Collective Behaviour in Ensembles of Ultracold Rubidium Atoms

ILIEVA, TEODORA,VELLCHEVA

Collective Behaviour in Ensembles of Ultracold Rubidium Atoms

Teodora Vellcheva Ilieva

A thesis submitted in partial fulfillment
of the requirements for the degree of
Doctor of Philosophy

Department of Physics
Durham University

2019

To Divna, Filip and Iliya

Abstract

High optical nonlinearities can be achieved at the single photon level by coupling the photon states to strongly interacting Rydberg excitations under the conditions of electromagnetically induced transparency. The nonlinear response in Rydberg quantum optics comes as a direct result of the long range dipole-dipole interactions via Rydberg blockade and interaction induced dephasing.

In this thesis, Rydberg quantum optics experiments are performed with two spatially separated mediums with a nonlinear response at the single photon level. Two ultracold rubidium atomic clouds are tightly confined by a pair of in-vacuo aspheric lenses such that only a few Rydberg excitations can exist in each one of the clouds simultaneously. The long range character of the dipole-dipole interactions leads to the generation of quantum states of light. The effective photon-photon interactions are directly observed as an anti-correlation in the simultaneous photon retrieval as a result of the non resonant van der Waals interactions. The collective Rydberg excitations, stored in the non-overlapping mediums, experience an additional spatial non-uniform phase.

In addition, we experimentally characterize the cooperative optical response of a cold atomic medium at a single photon level. This aims to exploit the enhancement of the spontaneous emissions decay rate (superradiance) as a dependence of the number of atoms involved in the ensemble.

The observed atomic response in two different regimes gives a further understanding of the system dynamics and unlocks a promising potential route towards the implementation in scalable, multichannel quantum optical devices.

Declaration

I confirm that the work in this thesis is based on research carried out at the Department of Physics, Durham University. Where material has been generated through joint work, the work of others has been indicated.

Teodora Ilieva
Durham, 27th August 2019

Acknowledgements

During the course of my PhD, I have had the privilege of working alongside many people, without whom this thesis would have never existed.

First, I must thank my supervisor Charles Adams for the given opportunity to work in the Rydberg Quantum Optics project. I am very grateful for his constant support, guidance and encouragement. I want to thank Hannes Busche, Simon Ball and Paul Huillery for showing me the ropes when I first stepped into the lab. I could not have achieved any of this without your guidance. Especially Paul who taught me how to develop both my theoretical and experimental skills and showed me what kind of scientist I want to be some day.

I also want to thank so many people in AtMol. Niamh Jackson for keeping me sane and never giving up on me when I was feeling down. Ryan Hanley for his endless optimism, support and patient explanation. Ifan Hughes, James Keaveney and Kate Whittaker, my thin cell team, for spending all this time giving me gaudiness in the hot vapour's field. The new Rydberg team, Yuechun Jiao, Chloe So and Charles Möhl for the warm welcoming back in the project. I want to thank Daniel Whiting, Paul, Niamh, Ryan and Kate for the friendship and constant laughs. The entire group of AtMol has been a lovely place to work. I also would like to thank Ryan, Niamh and Rob Bettles for reading this thesis.

Finally, I am incredibly lucky to have such an amazing family. My husband Iliya who has always supported me in the choices I have made, and have allowed me to pursue all my dreams. Thanks for always being there whenever I needed you. I must also thank my parents, who have always believed in me and love me unconditionally. My cousin, Cveta, whose frequent calls always cheer me up. Last, but definitely not least, I want to thank Filip who followed me to the northern part of England without a single doubt.

Contents

1. Introduction **19**

2. Atom-light interactions and Rydberg atoms **23**
2.1. Two-level system 24
2.2. Three-level system 28
2.3. Rydberg atoms 33

3. Experimental Setup **39**
3.1. Laser systems 41
3.2. Optical Setup 45

4. Superradiance and collective mode interference **49**
4.1. Driving field and atom behaviour 51
4.2. Experimental realization 54
4.3. Experimental results 56

5. Storage and retrieval of optical photons, Blockade vs. Dephasing model. **65**
5.1. Introduction 65
5.2. Storage and retrieval of optical photons 67
5.3. Experimental realization 70
5.4. Rydberg blockade simulation 75
5.5. Dephasing simulation 84
5.6. Summary 100

6. Towards single Rydberg excitation **101**
6.1. Introduction 101
6.2. Experimental improvements 104
6.3. Expected behaviour of the retrieved single photon pattern 111
6.4. Summary 115

7. Conclusion and Outlook **117**

Appendix **121**

A. Modelling the superradiance behavior **121**

B. Two-channel depahsing model with spin-wave operators **125**

C. Photon statistics **129**

Bibliography **133**

List of Figures

2.1. Two-level atom. 24
2.2. Optical susceptibility of a two-level medium. 27
2.3. Three-level atom. 28
2.4. Optical susceptibility of a three-level medium. 30
2.5. The dressed states of a three-level atom. 32
2.6. Dipole-dipole interactions. 34
2.7. An atomic to pair state basis. 35
2.8. Rydberg blockade. 36

3.1. Schematic of experiment setup. 40
3.2. Level scheme of the ^{87}Rb D2 line. 41
3.3. Sequence to prepare the atomic ensembles in the microscopic dipole traps. 43
3.4. Optical setup for two photonic channels. 45
3.5. Optical setup for the Rydberg coupling light. 46
3.6. Single photon Hanbury-Brown Twiss detection setup. . . . 47

4.1. The decay rates Γ and frequency shifts Δ of the individual symmetric eigenmodes. 52
4.2. A schematic of the experimental setup for ^{87}Rb D2 transition. 54
4.3. Experimental sub-microsecond sequence. 54
4.4. The optical driving pulse for different optical depths. . . . 56
4.5. Experimental lineshapes and corresponding Lorentzian fit. 56
4.6. Experimental and numerical decay rates as a function of steady state optical depth. 58
4.7. Experimental decay rates for four different detunings (0 MHz, +2 MHz, +3 MHz, +4 MHz). 59
4.8. Experimental decay rates for three different mean photon numbers 0.5, 1.5 and 4. 60
4.9. The second-order correlation function $g^2(0)$ as a function of time duration for the whole pulse. 60
4.10. The second-order correlation function $g^2(0)$ as a function of time duration for two different time slots within the pulse. 61
4.11. The initial transient peak of the optical driving pulse. . . . 62
4.12. Experimental decay rates of the initial transient peak on resonance. 62

5.1. A schematic of the spatially separated channels. 70

5.2. The micro-second storage sequence for the electromagnetically induced transparency signal and control fields and the optical trap. 71
5.3. Cross-talk between the two channels. 72
5.4. Autler-Townes splitting at $|30S_{1/2}\rangle$ as a function of the signal light detuning. 73
5.5. A histogram of detected photon events at Rydberg state $|80S_{1/2}\rangle$. 74
5.6. A schematic of the Rydberg partial blockade regime. . . . 75
5.7. A scheme of the Rydberg blockade model used to simulate the photon statistics gathered from the experiment. 76
5.8. Two clouds with Gaussian distributed atoms shifted from one another at a distance of 10 µm. 77
5.9. Two clouds with Gaussian distributed atoms shifted from one another at a distance of 10 µm with excited Rydberg atoms and a corresponding blockade radius of 6 µm. 78
5.10. Calculated cross-correlation and single-correlation function dependence on the clouds length for four different longitudinal cloud sizes. 79
5.11. Cross-correlation function $g^{(2)}_{AB}$ measured in the experiment for different clouds separation at level $|80S_{1/2}\rangle$ and the calculated cross-correlation function $g^{(2)}_{AB}$. 79
5.12. Single-correlation function $g^{(2)}_{A}$ measured in the experiment at level $|80S_{1/2}\rangle$ and the calculated single-correlation function $g^{(2)}_{A}$. 80
5.13. Calculated cross-correlation function $g^{(2)}_{AB}$ for different number of photons sent to the clouds at Rydberg state $|80S_{1/2}\rangle$. 81
5.14. Cross-correlation function $g^{(2)}_{AB}$ and single-correlation function $g^{(2)}_{A}$ measured at different Rydberg states for a fixed clouds separation of 10 µm. 81
5.15. Cross-correlation function $g^{(2)}_{AB}$ and each one of the clouds individually measured in the experiment at a fixed $|80S_{1/2}\rangle$ Rydberg state for different clouds separations. 82
5.16. Simulation results for single-correlation function $g^{(2)}_{A}$ at different storage times. 86
5.17. Simulation results for single-correlation function $g^{(2)}_{A}$ for different for different collective Rydberg states $|nS_{1/2}\rangle$. . . 87
5.18. A scheme of the dephasing model used to simulate the photon statistics gathered from the experiment. 89

5.19. Simulation results for cross-correlation function $g^{(2)}_{AB}$ at 10 µm clouds separation for different storage times. 90
5.20. Simulation results for cross-correlation function $g^{(2)}_{AB}$ at different clouds separation for different collective Rydberg states $|nS_{1/2}\rangle$. 91
5.21. Simulation results for cross-correlation function $g^{(2)}_{AB}$ for a cloud separation of 10 µm for different collective Rydberg states $|nS_{1/2}\rangle$. 92
5.22. The effect of the interaction strength over the retrieved photon statistics. 93
5.23. The effect of the clouds separation on retrieved photon statistics. 94
5.24. The effect of the interaction time on retrieved photon statistics. 95
5.25. The evolution of the imprinted spin-wave phase pattern during storage at $|80S_{1/2}\rangle$ and 10 µm away excitation. . . . 96
5.26. The emitted phase pattern of the stored photons at $|80S_{1/2}\rangle$ and separation of 10 µm. 97
5.27. A schematic of the Rydberg dephasing regime. 97
5.28. The evolution of the imprinted spin-wave phase pattern during storage at $|80S_{1/2}\rangle$ and 5 µm shift from the center excitation. 98

6.1. Different configurations for effective photon photon interactions. 101
6.2. A schematic of a fully blockaded regime. 102
6.3. Effective photon-photon interactions regime. 103
6.4. Optical setup for two photonic channels. 105
6.5. A schematic of the setup of the crossed dipole trap. 106
6.6. Fluorescence imaging system. 107
6.7. Fluorescence imaging of the optical traps after a 100 µs exposure time. 108
6.8. An absorption signal from the tweezer trap and overlapped with the crossed trap. 109
6.9. Optical depth versus power in the tweezers. The crossed trap power is fixed at 600 mW. 110
6.10. Evolution of the imprinted spin-wave phase pattern during storage. 111
6.11. Projections of the expected photon pattern in xy (radial) plane retrieved from an atomic cloud. 112
6.12. Dependence of the deflection angle on the interaction time. 113

7.1. A single-correlation function $g^{(2)}(t)$ within the retrieved photon pulse. 118
7.2. Modulation of optical photons. 120

C.1. Photon events possible configurations inside the Hanbury-Brown Twiss interferometer. 130

List of Tables

2.1. Scaling of Rydberg atom properties with principal quantum number n for constant Ω 34

C.1. Probability table that connects the possible physical events in the experiment (the number of photons arriving on the detection system) with the detected events (click on a detector). 131

1. Introduction

The great interest in single-photon sources over the past few decades has always been based on their application in the quantum-information science [1], involving encoding, communication, manipulation, and measurement of information. Photons allow information to be encoded in the quantum state as polarization or momentum and are ideal carriers of classical or quantum information due to their weak interaction with the environment over long distances [2]. This results in lower levels of noise and losses. However, the absence of interactions leads to the fact that photons are relatively difficult to control at the single quantum object level. Single-photon processes depend on probabilistic protocols, and consequently have a very small probability of success.

Ideally, a single photon source should be deterministic or on-demand with a 100% probability of emitting a single photon. Furthermore, the emitted photons should be indistinguishable, and have a relatively fast repetition rate. A wide variety of schemes have been explored to emit a single photon at any arbitrary time defined by the user, based on color centers [3–5], quantum dots [6–8], single atoms [9], single ions [10], single molecules [11] and atomic ensembles [12]. Plenty of sources where the creation of photon pairs is probabilistic, rather than deterministic have also been investigated. In those cases the photons are created in pairs by parametric downconversion in bulk crystals [13], waveguides [14] and four-wave mixing [14, 15].

There are variety of approaches that lead to single quanta, in most of which the system is driven to an excited state that will emit a single photon. Unfortunately, in the case of a single emitter, this process is not so controllable. When the photon is absorbed it will be scattered spontaneously in a random direction and the system's response will be different for a second photon. Optical cavities have been used to engineer the emission in a well-controlled environment, providing a response on a single photon level [8, 16–18].

Single photon sources that use collective excitations in ensembles of atoms have also been investigated [19–22], with the advantage of producing directional emission.

Although the weak free-space direct interactions make photons ideal carriers of information, they also make them difficult to implement in quantum processes and quantum optical devices. Interactions between photons can be mediated indirectly if the interaction is strong enough to produce a non-linear response [23]. Effective interactions at a single photon level can be achieved in high-Q cavities [24] or strongly interacting atoms [25].

A single collective Rydberg excitation could change the optical response of a whole ensemble of atoms [26]. This provides a large optical non-linearity at the single photon level and therefore the potential to realize fully deterministic protocols for manipulating photons.

In Rydberg nonlinear optics [27–29], an electromagnetically induced transparency process is used as a coherent method to mediate photon-photon interactions. As a result of the dipole blockade effect, the system can be put in a regime of a non-classical state of light even when the input pulse is a classical, coherent state [25, 30].

Most effective interaction schemes require photons that propagate in overlapping optical modes inside a medium. Rydberg atoms long range dipole–dipole interactions (over many micrometers) not only provide a deterministic single photon source, but at the same time provides an approach to engineer effective contactless photon-photon interactions, removing the requirement for the overlapping of optical modes [31].

This thesis aims to investigate a controllable response at the level of single optical photons, by presenting a cooperative behaviour in an ensemble of cold rubidium atoms. Initially it is demonstrated how an ensemble of atoms in dimensions larger than the optical wavelength (outside the Dicke limit) and driven by a classical external field, can collectively enhance the emission decay rate. Furthermore two different system models are presented and analysed in order to explain the observed, experimentally effective contactless photon-photon interactions. The photons are stored as strongly interacting collective Rydberg excitations in spatially separated cold atomic mediums [31]. The single quanta level and the high indistinguishability of the created photons (identical in spatial shape, wavelength, polarization etc.) are the main requirements for implementation in optical quantum technologies. The steps performed in taking the experiment to a single photon regime are also discussed, as well as the future avenues which this regime will unlock.

Thesis structure

This thesis is structured as follows:

- Chapter 2 reviews and summarises both atom-light interactions and the most important properties of Rydberg atoms.
- Chapter 3 introduces the experimental setup.
- Chapter 4 is focused on the collective enhancement of the directional emission of a cold atomic ensemble.
- Chapter 5 covers different theoretical approaches in understanding the contactless interactions between non-overlapping optical photons in spatially separated mediums.
- Chapter 6 introduces the new improved experimental setup and what to expect as a result of contactless interactions at a single-photon level.

Publications arising from this work

- H. Busche, P. Huillery, S. W. Ball, T. V. Ilieva, M. P. A. Jones and C. S. Adams, "Contactless non-linear optics mediated by long-range Rydberg interactions", *Nat. Phys.*, **13**, 655 (2017)
- R. J. Bettles, T. Ilieva, H. Busche, P. Huillery, S. W. Ball, N. L. R. Spong and C. S. Adams, Collective mode interferences in light–matter interactions, *arXiv:1808.08415*, (2019)

2. Atom-light interactions and Rydberg atoms

The optical nonlinearities and non-local interactions between photons are engineered using Rydberg electromagnetically induced transparency. The combination of a three-level atomic system with Rydberg interactions as well as collective emission effects create a rich platform for quantum optics. In this section the main physical concepts are summarized.

2.1. Two-level system

This section covers the interaction between a coherent light field and an ensemble of atoms. The atom-light interaction will be considered in a simple case of an oscillator with two levels, coupled by a resonant driving classical field, with a frequency ω_S, shown in figure 2.1. The expected atomic response will be linear.

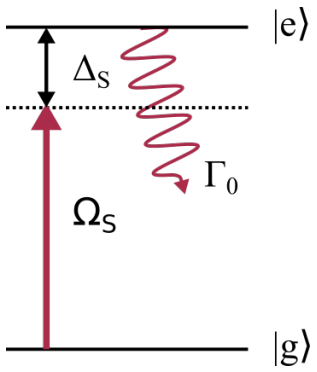

Figure 2.1.: Two-level atom. A signal laser field is used to excite from $|g\rangle$ to $|e\rangle$. The field is detuned from resonance by Δ_S and has a Rabi frequency of Ω_S. The decay rate is Γ_0.

The resonant transition between the ground state $|g\rangle$ and the excited state $|e\rangle$ is at a frequency ω_{ge}. The detuning of the resonant driving field from this resonance frequency is given by:

$$\Delta_S = \omega_S - \omega_{ge}. \tag{2.1}$$

The excited state $|e\rangle$ spontaneously decays with a decay rate of Γ_0. For rubidium, Γ_0 is $2\pi{\cdot}6.065\,\mathrm{MHz}$ [32]. In addition, there is another source of decoherence - the finite linewidth of the driving laser field γ_S. The coherence decay rate is given by [33]:

$$\gamma_{ge} = \frac{\Gamma_0}{2} + \gamma_S. \tag{2.2}$$

The time evolution of the atom-light system can be calculated using the time-dependent Schrödinger equation:

$$i\hbar\frac{\partial}{\partial t}|\psi\rangle = \hat{H}_{tot}|\psi\rangle \tag{2.3}$$

where the Hamiltonian of the combined atom-light system is given by the Hamiltonian for the atom and the Hamiltonian for the interaction with the light field:

$$\hat{H}_{\text{tot}} = \hat{H}_{\text{atom}} + \hat{H}_{\text{int}}. \tag{2.4}$$

Only the interaction between the applied light field and the electric dipole moment of the atom will be considered, higher order terms are neglected. This approximation is known as electric-dipole approximation, where the wavelength of the emitted light field is much larger than atomic dimensions, therefore $e^{i\vec{k}\cdot r} \approx 1$.

The unperturbed Hamiltonian of the atom can be written as:

$$H_{\text{atom}} = \frac{\hbar\omega_{\text{ge}}}{2}(|e\rangle\langle e| - |g\rangle\langle g|). \tag{2.5}$$

And the interaction Hamiltonian is given by:

$$\hat{H}_{\text{int}} = -\hat{d} \cdot \vec{E}, \tag{2.6}$$

where $\hat{d}$ is the electric dipole moment operator and in a two-level system can be expressed as:

$$d = d_{\text{eg}}(|g\rangle\langle e| + |g\rangle\langle e|), \tag{2.7}$$

E is the classical laser field

$$E = E_0 \cos(\omega_{\text{S}} t) = \frac{E_0}{2}(e^{i\omega_{\text{S}} t} + e^{-i\omega_{\text{S}} t}). \tag{2.8}$$

Combining equations (2.6) to (2.8) gives the interaction Hamiltonian:

$$H_{\text{int}} = d_{\text{eg}}\frac{E_0}{2}(|g\rangle\langle e| + |g\rangle\langle e|)(e^{i\omega_{\text{S}} t} + e^{-i\omega_{\text{S}} t}). \tag{2.9}$$

Using the rotating wave approximation the total Hamiltonian can be rewritten:

$$\hat{H} = \frac{\hbar}{2}\begin{pmatrix} 0 & \Omega_{\text{S}} e^{i\omega_{\text{S}} t} \\ \Omega_{\text{S}} e^{-i\omega_{\text{S}} t} & 2\omega_{ge} \end{pmatrix} \tag{2.10}$$

where $\Omega_{\text{S}} = d_{\text{ge}} E_0/\hbar$ is the angular Rabi frequency.

The time evolution of the system can then be calculated from the time dependent Schrödinger equation, which for the density matrix ρ is

equivalent to solving Liouville's equation:

$$\frac{d\rho}{dt} = \frac{i}{\hbar}[\rho, \hat{H}_{\text{tot}}]. \tag{2.11}$$

The density matrix formalism does not account for decay in the system or any decoherent processes, such as spontaneous emission. All of this is added by a decay matrix $\hat{\mathcal{L}}$. The resulting equation is called Lindblad master equation [34] and is given by:

$$\frac{d\rho}{dt} = \frac{i}{\hbar}[\rho, \hat{H}_{\text{tot}}] + \hat{\mathcal{L}}. \tag{2.12}$$

For the two-level system, this decay matrix is:

$$\hat{\mathcal{L}} = \frac{1}{2}\begin{pmatrix} 2\Gamma_0\rho_{\text{ee}} & -\Gamma_0\tilde{\rho}_{\text{ge}} \\ -\Gamma_0\tilde{\rho}_{\text{eg}} & -2\Gamma_0\rho_{\text{ee}} \end{pmatrix} \tag{2.13}$$

where $\tilde{\rho}_{\text{ge}} = \rho_{\text{ge}}e^{-i\omega_{\text{S}}t}$ and $\tilde{\rho}_{\text{eg}} = \rho_{\text{eg}}e^{i\omega_{\text{S}}t}$.

The time evolution of the density matrix can be derived as a series of coupled, first order equations, known as the optical Bloch equations for a two-level system including only a spontaneous decay:

$$\frac{d\rho_{gg}}{dt} = i\frac{\Omega_{\text{S}}}{2}(\tilde{\rho}_{ge} - \tilde{\rho}_{eg}) + \Gamma_0\rho_{ee}, \tag{2.14}$$

$$\frac{d\tilde{\rho}_{ge}}{dt} = i\frac{\Omega_{\text{S}}}{2}(\rho_{gg} - \rho_{ee}) + \tilde{\rho}_{ge}(-i\Delta - \Gamma_0/2), \tag{2.15}$$

$$\frac{d\rho_{ee}}{dt} = i\frac{\Omega_{\text{S}}}{2}(\tilde{\rho}_{eg} - \tilde{\rho}_{ge}) - \Gamma_0\rho_{ee}, \tag{2.16}$$

$$\frac{d\tilde{\rho}_{eg}}{dt} = i\frac{\Omega_{\text{S}}}{2}(\rho_{ee} - \rho_{gg}) + \tilde{\rho}_{eg}(i\Delta - \Gamma_0/2). \tag{2.17}$$

In the steady state $d\rho/dt = 0$ and to conserve the population $\rho_{gg}+\rho_{ee} = 1$. Therefore $\tilde{\rho}_{\text{eg}}$ can be expressed as:

$$\tilde{\rho}_{eg} = -\frac{i\Omega_{\text{S}}/2}{\Gamma_0/2 - i\Delta_{\text{S}}}(\rho_{gg} - \rho_{ee}). \tag{2.18}$$

The optical response of the atomic system to an applied light field is defined by the complex susceptibility χ and can be calculated from the off-diagonal coherence terms of the density matrix. The susceptibility of

the medium is given as:

$$\chi = \frac{-2Nd_{eg}^2}{E_0\hbar\Omega_S}\tilde{\rho}_{eg}. \tag{2.19}$$

where N is the number density.

In a weak probe limit ($\Omega_S \ll \Gamma_0$), the population remains mainly in the ground state ($\rho_{gg} - \rho_{ee} \approx 1$), the susceptibility can be expressed as a function of the laser detuning Δ_S:

$$\chi = \frac{iNd_{eg}^2}{E_0\hbar(\Gamma_0/2 - i\Delta_S)} = \mathrm{Re}(\chi) + \mathrm{Im}(\chi). \tag{2.20}$$

The $\mathrm{Re}(\chi)$ describes the dispersion and $\mathrm{Im}(\chi)$ describes the transmission and has a Lorentzian lineshape as shown in figure 2.2. The susceptibility is normalized to the susceptibility on resonance. The refractive index, $\tilde{n}$, of the medium is given by its susceptibility, where $\tilde{n} = \sqrt{1+\chi}$.

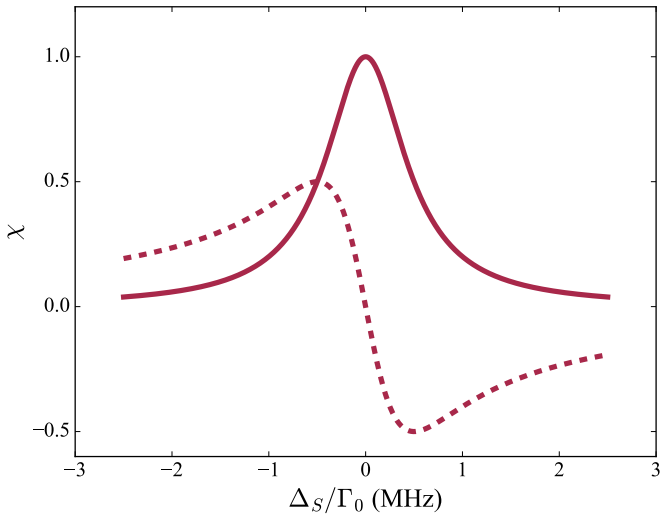

Figure 2.2.: The imaginary part which defines transmission (red solid line) and the real part which defines the dispersion (red dashed line) of the normalized optical susceptibility $\chi(\Delta_S)$ of a two-level system.

2.2. Three-level system

The three atomic states are arranged in a ladder configuration: a ground state $|g\rangle$, an intermediate excited state $|e\rangle$, and upper excited state $|r\rangle$, in our case a Rydberg state. A second laser field is added to the system to couple the intermediate $|e\rangle$ and the upper excited state $|r\rangle$. The coupling laser field Rabi frequency is Ω_C, detuned by $\Delta_C = \omega_C - \omega_{er}$, where ω_{er} is the resonant transition frequency and ω_C is the coupling driving field frequency. The excitation scheme is shown in figure 2.3.

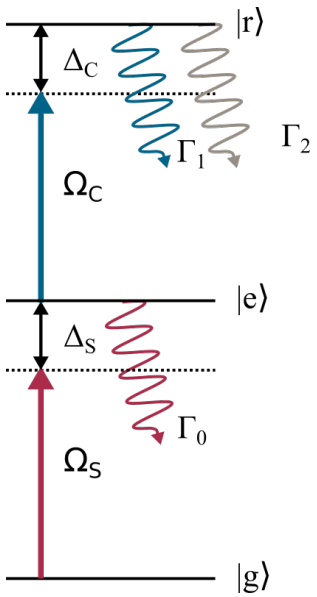

Figure 2.3.: Three-level atom. A signal laser field with Rabi frequency Ω_S and detuning Δ_S is used to excite from $|g\rangle$ to $|e\rangle$ and a second laser field with Rabi frequency Ω_C and detuning Δ_C is added to couple the lower excited state $|e\rangle$ to the upper excited state $|r\rangle$ in a ladder scheme.

The interaction Hamiltonian of the three-level system is [35]:

$$H_{\text{tot}} = H_{\text{atom}} + H_{\text{int}} = \frac{\hbar}{2}\begin{pmatrix} 0 & \Omega_{\text{ge}} & 0 \\ \Omega_S & -2\Delta_S & \Omega_C \\ 0 & \Omega_C & -2(\Delta_S + \Delta_C) \end{pmatrix}. \tag{2.21}$$

Again the time evolution of the system can then be calculated from the

Lindblad master equation (2.12) with decay Lindblad operator[34]:

$$\hat{\mathcal{L}} = \frac{1}{2}\begin{pmatrix} 2\Gamma_0\rho_{ee} & (\Gamma_0)\tilde{\rho}_{ge} & -\Gamma_1\tilde{\rho}_{gr} \\ -\Gamma_0\tilde{\rho}_{eg} & 2(\Gamma_1\rho_{rr} - \Gamma_0\rho_{ee}) & -(\Gamma_0+\Gamma_1)\tilde{\rho}_{er} \\ -\Gamma_1\tilde{\rho}_{rg} & -(\Gamma_0+\Gamma_1)\tilde{\rho}_{re} & -2\Gamma_1\rho_{rr} \end{pmatrix}. \tag{2.22}$$

In a weak probe limit ($\Omega_S \approx 0$ and $\rho_{ee} = \rho_{rr} \approx 0$), the coherence term $\tilde{\rho}_{eg}$ in the steady state is given by:

$$\tilde{\rho}_{eg} = -\frac{i\Omega_S/2}{\gamma_1 - i\Delta_S + \Omega_C^2/4(\gamma_2 - i(\Delta_S + \Delta_C))} \tag{2.23}$$

where the decay rates are:

$$\gamma_1 = \frac{\Gamma_2}{2} + \gamma_S \tag{2.24}$$

and

$$\gamma_2 = \frac{\Gamma_2}{2} + \gamma_S + \gamma_C. \tag{2.25}$$

where γ_S and γ_C are the corresponding finite laser linewidths.

The susceptibility is calculated the same way as in a two-level system by substituting the coherence term $\tilde{\rho}_{eg}$:

$$\chi = \frac{Nd_{eg}^2}{E_0\hbar}\frac{1}{\gamma_1 - i\Delta_S + \Omega_C^2/4(\gamma_2 - i(\Delta_S + \Delta_C))}. \tag{2.26}$$

Again the real and imaginary parts of the susceptibility $\chi(\Delta_S)$ give the optical response of the system as in the two-level case. In the presence of a coupling field, a narrow transparency window appears around resonance. In figure 2.4, the change in imaginary and real part of the optical susceptibility, for different Rabi frequency of the control field Ω_C, is shown. Δ_C is set to 0 so the two photon resonance appears at $\Delta_S = 0$. All the susceptibilities are normalized to the imaginary part of the corresponding susceptibility on resonance. For $\Omega_C = 0$, the system is the same as for the two-level case as there is no coupling light. For $\Omega_C = \Gamma_0/2$, a narrow transparency window appears in the transmission, with a steep gradient in the dispersion, when on resonance ($\Delta_S = 0$). If the control Rabi frequency Ω_C is increased beyond the linewidth of the signal transmission Γ_0, the absorption line splits into two lines, separated by the coupling Rabi frequency Ω_C [36].

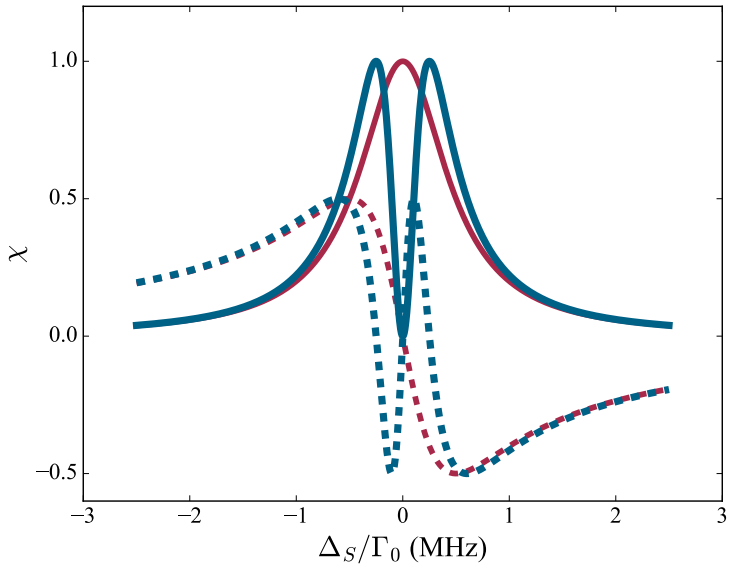

Figure 2.4.: The imaginary part which defines transmission (solid lines) and the real part which defines the dispersion (dashed lines) of the normalized optical susceptibility $\chi(\Delta_S)$ of a three-level ladder system. For $\Omega_C = 0$, there is no coupling field and the system is as in the two-level case. Increasing the coupling $\Omega_C = \Gamma_0/2$, a narrow transparency window appears at resonance $\Delta_S = 0$ in the transmission (blue solid line) and a steep gradient in the dispersion (blue dashed line).

Controlling the Rabi frequency of the control light Ω_C in three-level ladder system allows us to change the medium's susceptibility to the signal light. The transparency window at resonance frequency, in presence of the control field coupling to the upper excited state, can be understood by diagonalising the Hamiltonian H_{tot} (equation 2.21) to get the eigenstates on the two-photon resonance $\Delta_S + \Delta_C = 0$ [37].

$$\begin{aligned} |+\rangle &= \sin\theta \sin\phi |g\rangle + \cos\phi |e\rangle + \cos\theta \sin\phi |r\rangle, \\ |D\rangle &= \cos\theta |g\rangle \sin\theta |r\rangle, \\ |-\rangle &= \sin\theta \cos\phi |g\rangle - \sin\phi |e\rangle + \cos\theta \cos\phi |r\rangle, \end{aligned} \tag{2.27}$$

where θ and ϕ are the mixing angles defined as:

$$\begin{aligned} \tan\theta &= \frac{\Omega_{\mathrm{S}}}{\Omega_{\mathrm{C}}}, \\ \tan 2\phi &= \frac{\sqrt{\Omega_{\mathrm{S}}^2 + \Omega_{\mathrm{C}}^2}}{\Delta_{\mathrm{S}}} \end{aligned} \tag{2.28}$$

or can be written as:

$$\begin{aligned} \theta &= \arctan\Big(\frac{\Omega_{\mathrm{S}}}{\Omega_{\mathrm{C}}}\Big), \\ \phi &= \frac{1}{2}\arctan\Big(\frac{\sqrt{\Omega_{\mathrm{S}}^2 + \Omega_{\mathrm{C}}^2}}{\Delta_{\mathrm{S}}}\Big). \end{aligned} \tag{2.29}$$

The energy eigenvalues are:

$$\begin{aligned} E_{\pm} &= \frac{\hbar}{2}\Big(\Delta_{\mathrm{S}} \pm \sqrt{(\Delta_{\mathrm{S}}^2 + \Omega_{\mathrm{S}}^2 + \Omega_{\mathrm{C}}^2)}\Big), \\ E_D &= 0. \end{aligned} \tag{2.30}$$

In the weak probe limit and on resonance ($\Delta_{\mathrm{S}} = 0$ and $\Omega_{\mathrm{S}} \ll \Omega_{\mathrm{C}}$), the mixing angle $\theta \to 0$ and the eigenstates are:

$$\begin{aligned} |\pm\rangle &= (|r\rangle \pm |e\rangle)/\sqrt{2}, \\ |D\rangle &= |g\rangle. \end{aligned} \tag{2.31}$$

The signal laser field only couples to the $|e\rangle$ component of the states $|\pm\rangle$ as shown in figure 2.5. These two states have equal amplitude but with opposite signs and as a result they will interfere destructively - the signal laser field is suppressed or no longer absorbed, giving rise to the transparency seen in figure 2.4. The state $|D\rangle$ is known as a dark state or zero-energy eigenstate (zero-energy eigenvalue) and it is not coupled to the light field.

On resonance, the coupling laser field switches the imaginary susceptibility from a maximum to zero. These changes in the susceptibility lead to changes in the signal light group velocity:

$$v_g = \frac{d\omega_{\mathrm{S}}}{dk_{\mathrm{S}}} \approx \frac{c}{\tilde{n}(\omega_{\mathrm{S}}) + \omega_{\mathrm{S}}\frac{dn}{d\omega_{\mathrm{S}}}} \approx \frac{c}{\tilde{n}_g} \tag{2.32}$$

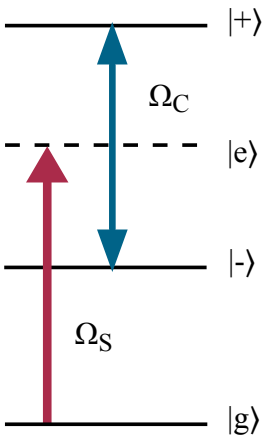

Figure 2.5.: The dressed states $|\pm\rangle$ are split by the Rabi frequency of the coupling laser field Ω_C. At the two-photon resonance, $\Delta_S + \Delta_C = 0$, the probability to populate $|+\rangle$ destructively interferes with the probability to populate $|-\rangle$. This results in a transparency.

As a result the group velocity is reduced on resonance and the light is slowed. The group index increases:

$$\tilde{n}_g = \frac{6\pi\rho c}{k_S^2} \frac{\gamma_1}{\Omega_C^2 + \gamma_2\gamma_1/4}. \tag{2.33}$$

The dependence of the group index $\tilde{n}_g$ on the Rabi frequency of the control field Ω_C allows to control the signal light group velocity v_g by changing the intensity of the control field. If Ω_C is reduced adiabatically to 0, the signal field photons can be stored as a spin-wave in a collective Rydberg atomic excitation [38–40].

2.3. Rydberg atoms

In order to observe effective photon-photon interactions, an introduction to Rydberg atom physics should also be discussed, along with the effect of the dipole-dipole interactions.

A Rydberg atom is an atom whose valence electron is excited in a state with high principal quantum number n. The binding energies E_n are well described by the Rydberg's formula:

$$E_n = -\frac{Ry}{n^2}, \tag{2.34}$$

which describes the convergence of spectral lines in hydrogen atom [41]. Ry is the Rydberg constant.

Many of the Rydberg properties can be concluded by the use of the classical Bohr model (a point-like electron orbits a point-like proton). The electron experiences a Coloumb potential dependent on the radius of its orbit. As the radius increases the electron experiences a weaker potential. The required ionisation energy becomes very small and the electron is extremely sensitive to external electric fields. For atoms with a similar electronic structure to hydrogen, like alkali metals, the difference from hydrogen model is given by the quantum defect δ_{nLJ}. It depends on the atomic species, the state's orbital and total angular momentum, and the principal quantum numbers n, L and J. The binding energy becomes:

$$E_n = -\frac{Ry}{(n-\delta_{\mathrm{nLJ}})^2}. \tag{2.35}$$

For rubidium, these quantum defects have been measured and are available in the literature [42–44].

The large electron radius gives rise to the dramatic scaling of various properties, with the principal quantum number n, summarized in table 2.1.

The weak electric binding forces of the outer electron to the nucleus makes Rydberg atoms sensitive to external electric fields. The polarisability of a Rydberg atom scales with the seventh power of the principal quantum number n, and the van der Waals interaction between atoms with the eleventh power. The long lifetimes and the strong dipole-dipole interactions makes Rydberg atoms very interesting for applications in quantum simulation, quantum optics and quantum information processing [45–47].

Table 2.1.: Scaling of Rydberg atom properties with principal quantum number n for constant Ω

Binding energy	n^{-2}
Orbital radius	n^2
Polarisability	n^7
Radiative lifetime	n^3
Dipole moment	n^2
Van der Waals interactions (C_6)	n^{11}
Van der Waals blockade radius $r_b^{(6)}$	$n^{11/6}$
Resonant dipole interactions (C_3)	n^4
Resonant dipole blockade radius $r_b^{(3)}$	$n^{4/3}$

Let us consider two atoms separated by distance r as shown in figure 2.6. The presence of the second atom results in a polarisation of the charge distribution of the first atom and vice versa. The dipole-dipole interaction energy between the two atoms is:

$$V(\vec{r}) = \frac{1}{4\pi\epsilon_0}\left(\frac{\vec{d_1}.\vec{d_2}}{|\vec{r}|^3} - \frac{3(\vec{d_1}.\vec{r})(\vec{d_2}.\vec{r})}{|\vec{r}|^5}\right), \tag{2.36}$$

where d_1 and d_2 are the induced dipole moments of these two atoms for the transitions from $|r\rangle$ to $|r'\rangle$ and from $|r\rangle$ to $|r''\rangle$ respectively.

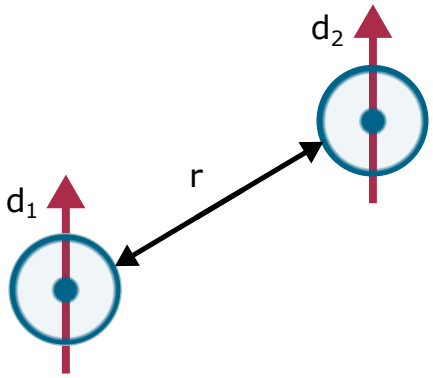

Figure 2.6.: Dipole-dipole interactions between two atoms separated by distance r with the induced dipole moments.

The energy shift as a result of the dipole-dipole interaction between these two Rydberg atoms, both in states $|r\rangle$ initially (figure 2.7), can be

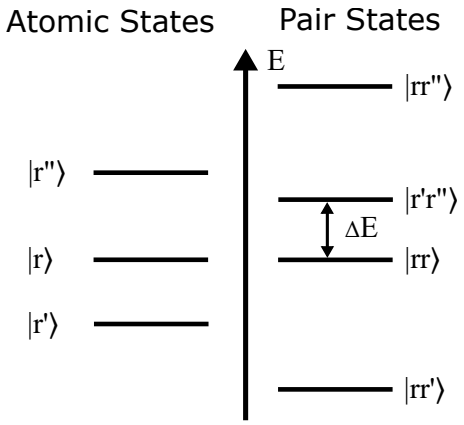

Figure 2.7.: An atomic to pair state basis. The near-resonant states coupled by the dipole-dipole interactions with an energy defect ΔE.

illustrated by considering the pair state basis $|rr\rangle$ and $|r'r''\rangle$ [48]. The energy separation between these levels is given by:

$$\Delta E = E_{r''} + E_{r'''} - 2E_r. \tag{2.37}$$

The dipole-dipole interaction depends on the separation between the atoms. Depending on the energy difference, ΔE, and the chosen Rydberg states there are two types of interactions:

Van der Waals interactions - when ΔE is large compared to the interaction potential $V(\vec{r})$.

As a result the atoms interact via the van der Waals potential:

$$V_{VdW} = -\frac{C_6}{|\vec{r}|^6}, \tag{2.38}$$

where the coefficient C_6 describes the interaction strength and scales with n^{11}. Usually van der Waals interactions appear when two atoms are in the same state, $|r\rangle$, or these two states are not directly dipole coupled.

The interaction strength for interactions between two rubidium atoms in $|rr\rangle = |60S_{1/2}, 60S_{1/2}\rangle$ is approximately $-140\,\mathrm{GHz\mu m}^{-6}$ [35]. In high $S_{1/2}$ states, the interactions are repulsive as the coefficient C_6 is negative.

Resonant dipole-dipole interactions - when the interaction potential $V(\vec{r})$ is stronger than the energy shift ΔE.

As a result, at short distances r, the atoms interact via the resonant

dipole-dipole potential [48]:

$$V_{dd}(\vec{r}) = \pm\frac{C_3}{|\vec{r}|^3}, \tag{2.39}$$

where the coefficient C_3 describes the interaction strength and scales with n^4.

Usually resonant dipole-dipole interactions appear when two atoms are in non-dipole coupled states or another dipole coupled pair state is nearby. Additional electric field can also be used to induce Stark shifts and put the system into resonance (Förster resonance [49, 50]). Two atoms can also be coupled to a nearby state of opposite parity using a microwave field. The resulting state $|r'r\rangle$ is resonant with the initial state $|rr'\rangle$. Excitation hopping processes appear over large distances [51] and are used to simulate energy transfer in biological systems (photosynthesis).

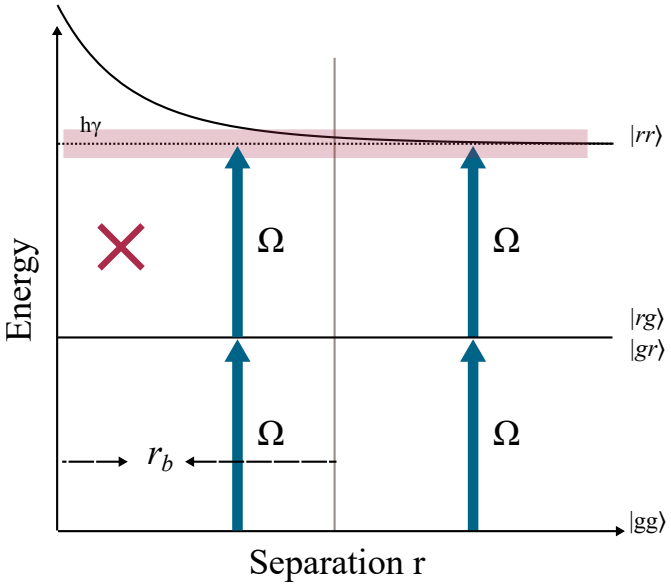

Figure 2.8.: The dipole-dipole interactions between Rydberg atoms lead to an energy shift beyond the linewidth $\hbar\gamma$ of the excitation laser field Ω. For distances beyond $r_b^{(k)}$, both of the atoms can be excited and for distances less than $r_b^{(k)}$ only single excitation $|gr\rangle$ or $|rg\rangle$ can exist.

The strong dipole-dipole interactions induce significant energy shifts in the μm range and, as a result, an excitation blockade. The excitation blockade allows a single photon to change the optical response of an atomic

medium over a range of many μm [26, 52, 53]. The concept of the dipole blockade was first proposed in [54, 55] as a way to create an universal quantum gate between atomic qubits.

The Rydberg blockade energy shift mechanism is shown in figure 2.8 as two atoms separated by a distance r. The interaction potential between the two atoms shifts the energy of the pair state $|rr\rangle$ by more than the linewidth $\hbar\gamma$ of the excitation laser field. This leads to a region where only a single Rydberg atom could exist within a volume defined by the blockade radius r_b:

$$r_b^{(k)} = \sqrt[k]{\frac{C_k}{\hbar\Omega}}, \tag{2.40}$$

where Ω is the Rabi frequency of the excitation laser field.

For van der Waals interactions, $k = 6$, and the blockade radius is $r_b^{(6)} \propto \sqrt[6]{C_6} \propto n^{11/6}$. For resonant dipole- dipole interactions, $k = 3$, and the blockade radius is $r_b^{(3)} \propto \sqrt[3]{C_3} \propto n^{4/3}$.

The dipole-dipole interactions play an important role in the system dynamics. The scaling with the principal quantum number n allows an easy control of the strength and the nature, attractive or repulsive, of the interactions. These interactions, and the cooperative effect as a result of them, will be explored in this thesis.

3. Experimental Setup

In order to exploit the strong nonlinearity between ultra-cold Rydberg atoms for quantum non-linear optics experiments, some requirements have to be fulfilled. Most of them are shared with most other ultracold atomic experiments, such as ultra-high vacuum conditions, various magnetic-fields, light for laser cooling and trapping, or imaging systems for diagnostics. However, there are some key requirements that had to be met in this particular setup: a detection system with high sensitivity to detect single photons; a control system to automate experiments; the capability to perform and repeat individual experimental shots sufficiently quickly in order to build up statistically meaningful data sets. Information on the design, implementation, and characterisation of the experimental setup is available in detail in several prior thesis from the Rydberg Quantum Optics project [56, 57]. In this chapter only parts of the existing setup, which are required for the work in this thesis, are documented.

Most single photon processes depend on probabilistic protocols and have a small probability of success. That leads to the requirement of a large number of measurements to gather enough photon statistics. A high atomic density is also required to ensure a large optical depth on the signal transition for experimental observation of cooperative optical effects.

The sequence used in each individual measurement is in order of μs while the cold atomic ensemble preparation takes $\approx 550\,\mathrm{ms}$. The main goal of the setup is to increase the number of times an ensemble can be recycled. This requires a speed up of the magneto-optical trap loading. For that purpose, a two-dimensional magneto-optical trap [58] is used to generate a slow atomic beam.

The main experimental apparatus has been designed and built by Hannes Busche, Simon Ball and Paul Huillery and is described in detail in [56, 57].

The high optical resolution, close to 1 µm for photon-photon interactions or close to the diffraction limit, required for the collective effects and Rydberg atoms interactions [54, 59], explored in the performed experiments, has been covered by a pair of high numeric aperture aspheric lenses. A schematic of the science chamber aspheric lenses is shown in figure 3.1. The lenses have an effective focal length $f_{\mathrm{eff}} = 10\,\mathrm{mm}$, a working distance

of $f_{\mathrm{wd}} = 7.0\,\mathrm{mm}$ and a numeric aperture of $NA = 0.5$. All laser light used for probing the cold atomic ensemble is along the axis defined by the pair of lenses.

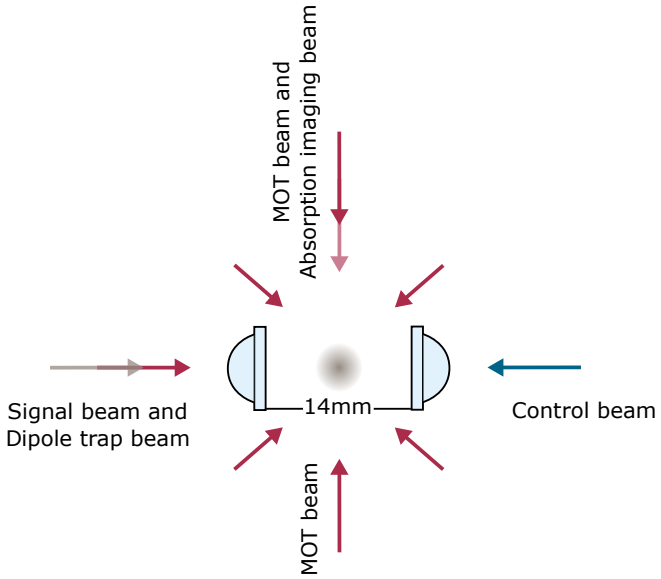

Figure 3.1.: Schematic of experiment setup. Three pairs of orthogonal beams (only axial are shown) overlap at the centre of a vacuum chamber to form a magneto-optical trap that slows and traps atoms. The signal light is overlapped with the dipole trap light and sent to the chamber. The counter propagating coupling laser, overlaps with signal beam. To avoid reflections on the aspheric lenses, the radial beam diameter is truncated to 4mm in the radial plane. The axial magneto-optical trap beam and an absorption imaging beam are overlapped due to limitation in the optical access in axial plane.

The lenses are separated by twice their working distance, allowing re-collimation of the signal and control laser beams, as well as the dipole trap laser beam, after focusing. Magnetic coils outside the science chamber provide a quantisation magnetic field along this axis. The sensitivity of Rydberg atoms to electric fields [48] requires both the compensation and minimization of any stray fields, which is achieved via a set of electrodes. A pair of magnetic coils provide an anti-Helmholtz field required for the magneto-optical trap [60].

3.1. Laser systems

780nm laser systems

The laser system [56, 57] provides coherent, narrow-linewidth light for cooling, trapping, and excitation of rubidium atoms.

A schematic of the transitions and hyperfine states of the ^{87}Rb D2-line is shown in figure 3.2.

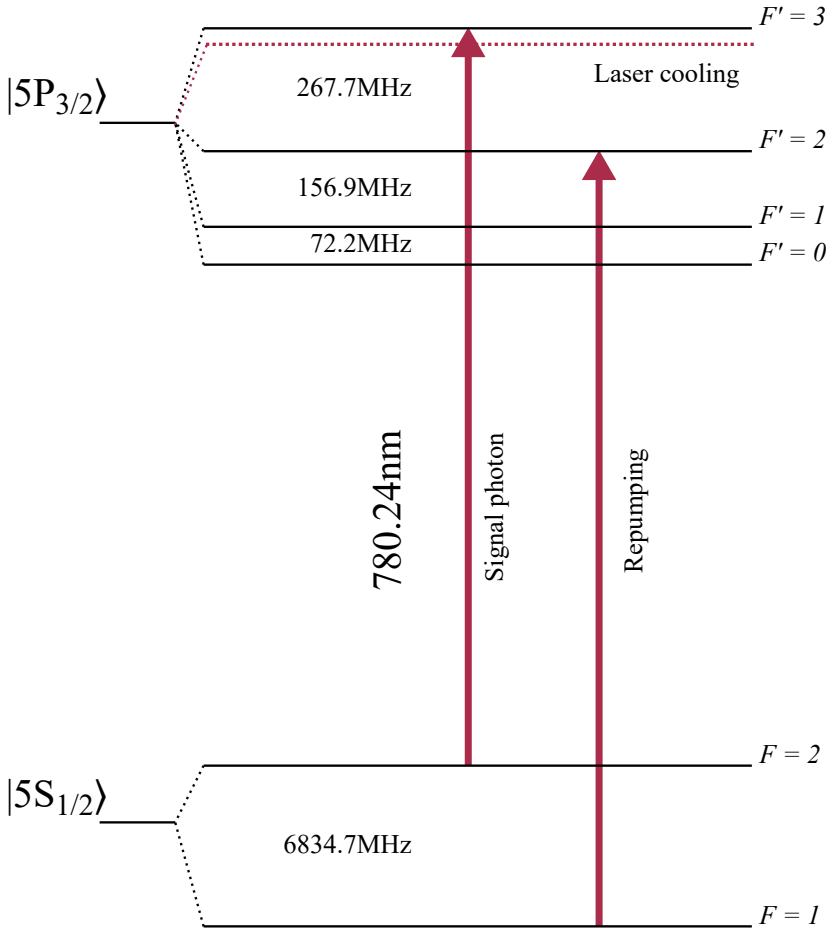

Figure 3.2.: Level scheme of the ^{87}Rb D2 line, D. Steck [32]. For laser cooling and repumping in the magneto-optical trap and the two-dimensional magneto-optical trap, the used transitions are $|5S_{1/2}, F = 2\rangle$ to $|5P_{3/2}, F' = 3\rangle$ and $|5S_{1/2}, F = 1\rangle$ to $|5P_{3/2}, F' = 2\rangle$. Signal light for Rydberg excitation uses $|5S_{1/2}, F = 2, m_F = 2\rangle$ to $|5P_{3/2}, F' = 3, m_{F'} = 3\rangle$ transition.

The cooling light and the excitation light are provided by a Toptica DL Pro diode laser. A Toptica BoosTA, seeded by the diode laser (around 40 mW), is used to provide high power (around 1.3 W) for the magneto-optical trap and the large interaction cooling volume of the two-dimensional magneto-optical trap. The diode laser is frequency stabilized to -140 MHz, red-detuned from the $|5S_{1/2}, F = 2\rangle$ to $|5P_{3/2}, F' = 3\rangle$ transition by modulation transfer spectroscopy [61, 62]. Small amount of the light provides the signal for the Rydberg electromagnetically induced transparency and red-detuned light (-140 MHz) for the $480nm$ laser system frequency stabilisation [63, 64].

The red-detuned cooling transition used is not perfectly closed and, due to the detuning, gives a non-zero probability to off-resonantly excited atoms to $|5P_{3/2}, F' = 2\rangle$, decaying to the lower $|5S_{1/2}, F = 1\rangle$ hyperfine ground state. These atoms need to be repumped [60]. The repumping light is provided by a diode Toptica DL100 laser which is frequency stabilized to the crossover resonance lines from $|5S_{1/2}, F = 1\rangle$ to $|5P_{3/2}, F' = 1 \times 2\rangle$ by frequency modulation spectroscopy [65, 66].

The light is delivered to the experiment using polarization maintaining optical fibers.

480nm laser system

The atoms are excited to a high Rydberg state by a two-photon transition. The first photon is at the same transition as the cooling transition from $|5S_{1/2}, F = 2, m_F = 2\rangle$ to $|5P_{3/2}, F' = 3, m_{F'} = 3\rangle$, while the second photon couples $|5P_{3/2}, F' = 3, m_{F'} = 3\rangle$ level with a Rydberg level $|nS_{1/2}\rangle$. A high power Toptica FALC 110 laser at 480 nm is used for that coupling. The Rydberg manifold allows the use of the same laser for a wide range of states. This laser is frequency stabilized by electromagnetically induced transparency spectroscopy [64] to the Rydberg state relative to the first photon excitation level.

The signal light detuning can be set independently, which allows compensation for the electric fields (Stark shifts) between the vacuum chamber and the Rubidium cell used for the locking.

The coupling light is switched by a polarisation switching electro-optic modulator. As a result the switching on and off times are approximately 100 ns. During this work, the electro-optic modulator has been substituted with a combination of acousto-optic modulators for faster switching times and better extinction of the zero power level. None of the presented results in this thesis has been taken using the acousto-optic modulators setup.

910nm laser system

The dipole trap laser is an in-house built ECDL and is amplified by an in-house built tapered amplifier [67]. The light is sent to the experiment by a single mode polarization maintaining fiber acting as a mode filter, providing a high purity TEM_{00} mode. The dipole trap is based on a red-detuned far off-resonant 910 nm laser light. Throughout this work, the dipole trap laser has been replaced with a 862 nm Toptica DL pro. The new laser performance will be discussed in Chapter 6.

Preparation of the microscopic dipole traps

To prepare the microscopic dipole traps the magneto-optical trap is loaded by the the two-dimensional magneto-optical trap, for typically 150 ms. The dipole trap is switched on at full power during the loading, because the AC Stark shift induced by the trap light shifts the repumping light off resonance at the trap position, creating an effective dark spot where atoms are no longer subject to light-induced collisions [68].

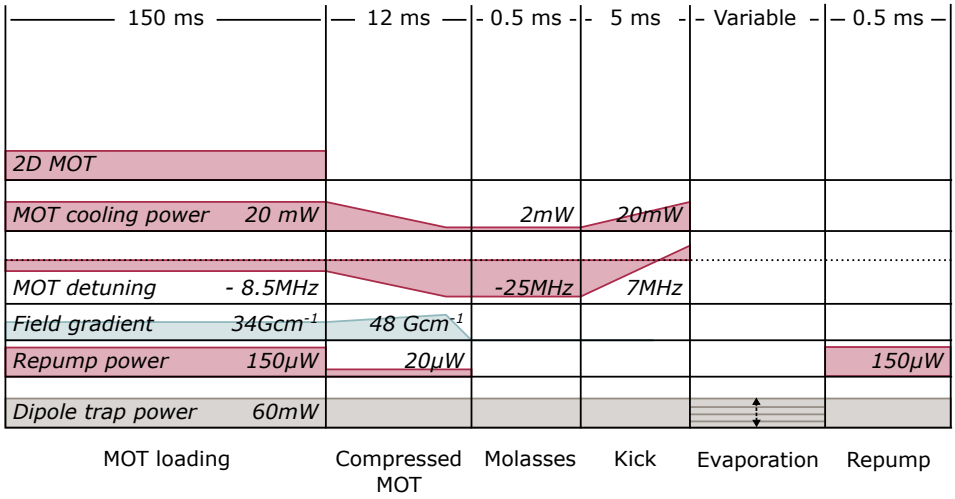

Figure 3.3.: Sequence to prepare the atomic ensembles in the microscopic dipole traps. The magneto-optical trap is loaded by the two-dimensional magneto-optical trap for approximately 150 ms and compressed to increase the atomic density. The dipole trap light is on throughout the whole sequence.

In the second step the magneto-optical trap is compressed for 12 ms by increasing the field gradient from 34 to 48 $\mathrm{Gcm^{-1}}$(axial) and ramping

down the repumping and cooling power to reduce light assisted collisions. At the end the magnetic field gradient is reduced to zero.

During the molasses stage, the repumping laser is switched off, resulting in the atoms being optically pumped into the lower ground state $|5S_{1/2}, F = 1\rangle$. The measured temperatures after the molasses stage are below 50 µK.

During the kick stage untrapped atoms, which can lead to unwanted absorption outside the dipole trap, are pushed out of the experimental volume by reactivating the magneto-optical trap cooling beams and ramping them to a blue detuning. The AC Stark shift of the atoms inside the dipole trap should remove the blue-detuned cooling light effect and as a result the atoms should stay unaffected.

The evaporation stage reduces the dimensions of the atomic cloud [69, 70]. Reducing the atoms temperature provides improvement of their confinement and reduces cross-talk between the two spatially separated channels. If no evaporation stage is applied, the untrapped atoms are pushed out of the trapped region. The repumping laser is switched on to pump atoms back into the upper ground state $|5S_{1/2}, F = 2\rangle$. All hyperfine Zeeman states are populated as no quantisation field is applied.

The entire preparation sequence is shown in figure 3.3.

3.2. Optical Setup

The optical setup for two photonic channels is shown in figure 3.4. The signal light is delivered to the experiment through polarization maintaining optical fibers. The signal and the trapping light are overlapped on a dichroic mirror and then split on a polarizing beam splitter (PBS). The beam paths are later recombined on a non-polarizing beam splitter (BS) which provides the same polarization for both signal beams so they can drive the same atomic transitions. At the end the beams are sent to the first in-vacuum lens which focuses them to $1/e^2$-waists of $1.0 \pm 0.1\,\mu m$ (signal light) and $4.5 \pm 0.3\,\mu m$ (dipole trap), respectively.

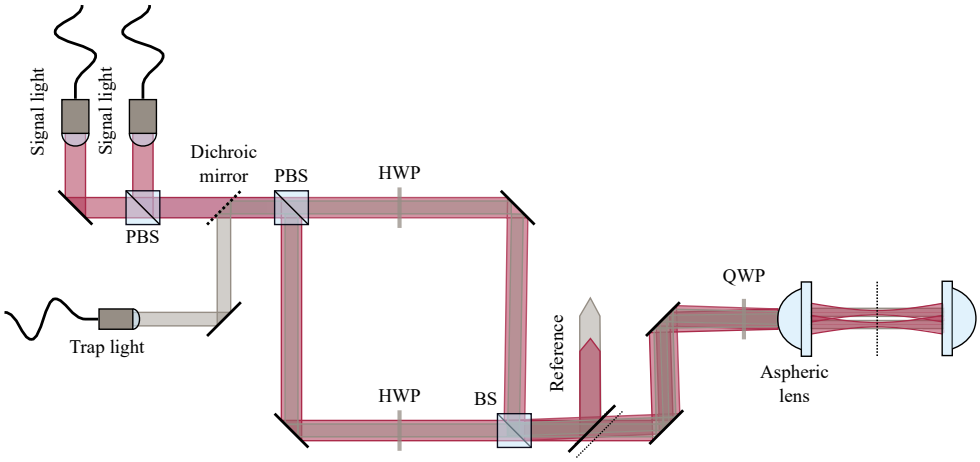

Figure 3.4.: Optical setup for two photonic channels. The signal beams are overlapped with the trap light on a dichroic mirror. Later, they are separated in a Mach-Zehnder interferometer and recombined on a non-polarising BS. The separation between the channels can be adjusted by changing the incident angle on the first in-vacuum lens. The lens focuses the signal and trap beams to $1/e^2$-waists of $1.0 \pm 0.1\,\mu m$ and $4.5 \pm 0.3\,\mu m$, respectively.

The red-detuned trapping light creates microscopic cigar-shaped ensemble of a few thousand cold rubidium atoms. The signal light is circularly polarized with detuning Δ from the $|5S_{1/2}, F = 2, m_F = 2\rangle$ to $|5P_{3/2}, F' = 3, m_{F'} = 3\rangle$ transition at $\lambda = 780.24nm$ (figure 3.2) with a natural linewidth of $\Gamma_0 = 2\pi \cdot 6.601\,\mathrm{MHz}$.

The separation between the two channels is adjusted by tilting and translating a mirror in one of the interferometer arms. As a result the

incident angle on the aspheric lens is changed.

The coupling laser light counter-propagates through the second in-vacuum lens of the vacuum chamber as shown in figure 3.5. After the coupling light fiber, there is an external lens used to focus in front of the second in-vacuum lens and not onto the atomic ensembles. The beam is approximately collimated among the overlapping volume with a waist of approximately 25 µm. This waist is sufficiently larger compared to the separation between the channels, that makes the applied Rabi frequency almost spatially independent. The coupling Rabi frequency for each channel is equalized by measuring the Autler Townes splitting of the absorption spectrum at low principle quantum number n and low photon number so there are no interaction effects.

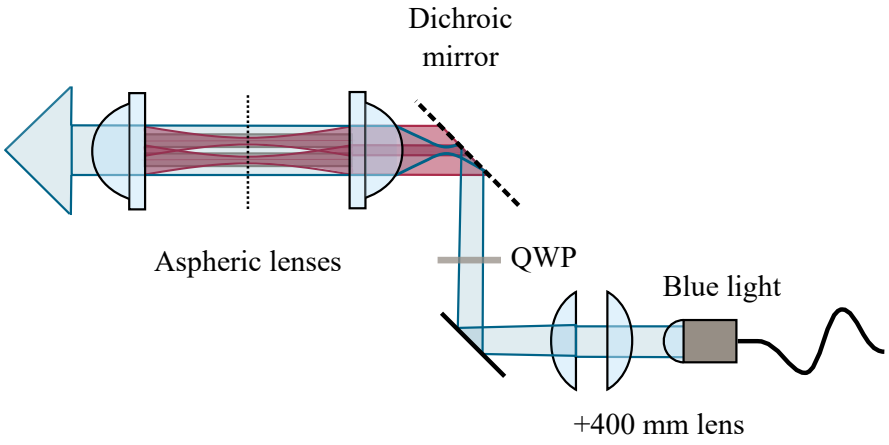

Figure 3.5.: The coupling light counter-propagates with respect to the signal light beam. A lens focuses the light in front of the in-vacuum lens, such that the beam is approximately collimated among the overlapping volume with a waist of $\approx 25\,\mu m$.

The detection experimental setup is built to be able to detect optical nonlinearities at the level of individual photon[27–29, 71], as well as measure the correlations between single photons. To detect extremely weak light fields, the used photodetectors should be extremely sensitive and with low noise levels.

The light emitted from the ensembles in the forward direction is collected by a second, identical lens and separated with an edge mirror at the focus of a 4:1 telescope. A schematic of the detection setup is shown in figure 3.6. The emitted photons are detected behind single-mode fibers. Each

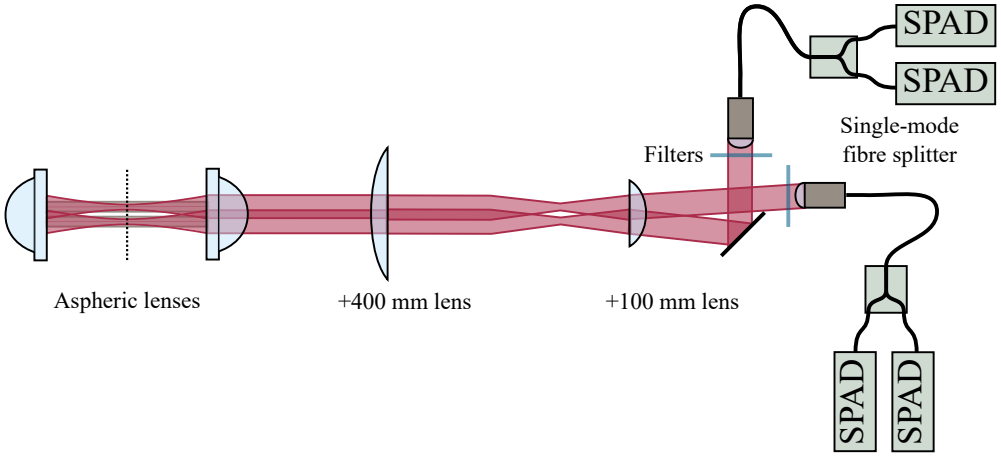

Figure 3.6.: Single photon Hanbury-Brown Twiss detection setup. The signal modes are separated with an edge mirror at the focus of a 4:1 telescope. Each signal mode is coupled into a single mode fiber splitter. A pair of filters is placed before each fiber to block the dipole trap at 910 nm, the coupling light at 480 nm and any additional background light.

fiber is aligned onto the original signal mode, acting as a mode filter which distinguishes target photons from those emitted elsewhere. A pair of filters, placed before each fiber, block the dipole trap at 910 nm, the coupling light at 480 nm and any additional background light.

A single detector setup is limited by its dead time and it can not count photons that are too close in time. To overcome this limitation, the detection setup for each optical channel consists of two single photon sensitive avalanche photo diodes (SPADs), arranged in Hanbury-Brown Twiss interferometer [72]. The typical overall detection efficiencies, including the quantum efficiencies of the detectors and transmission loss between the focal plane of in-vacuum lens pair to the detectors is approximately 20%. The SPADs' quantum efficiencies is approximately 60%. The detection efficiency is mostly limited by the in-vacuum lens pair coating, the filters and the fiber coupling.

Each individual detected event is recorded using the fast digital inputs of the FPGA based experimental control system DExTer [73] with a time resolution of 5 ns. The gathered photon statistics is analysed using a method described in Appendix C.

The experiments presented in Chapter 4 are carried out with signal photons using one of the channels. The contactless effective photon-photon interactions presented in Chapter 5 are carried out with signal photons

using a two-channel setup.

4. Superradiance and collective mode interference

The interaction of light with an atom can be dramatically modified if an atomic ensemble is used instead of a single atom. The atoms do not act independently and as a result the response of each atom will depend on the behavior of the rest of the ensemble. This phenomena is known as collective or cooperative behaviour, and usually leads to effects such as frequency shifts, modified decay rates, enhanced light–matter coupling and collective transparency in systems ranging from atoms [74–78] and ions [79] to quantum dots [80, 81]. The behaviour of these systems usually is described by collective eigenmodes. The collective response of the ensemble will depend on the orientation of the atoms as the dipole-dipole interaction is both long range and anisotropic.

In 1954, Dicke first considered the behaviour of an ensemble of atoms decaying in close proximity to each other [82]. In this case, the emission of a single atom is influenced by the presence of a second one. He calculated that a cloud of N two-level atoms, much smaller in size than a single wavelength, initially all prepared in their excited states, will spontaneously decay N times faster than just a single atom. All the atoms will be coupled to the same mode of the electromagnetic field and be prepared in a fully symmetric state. Over the past 60 years, enhanced superradiant decay has been observed in many different physical systems [74, 80, 83–85].

However, Dicke ignored the resonant dipole-dipole interaction between atoms separated by such small distances. As a result, the superradiant decay is due to the emitted radiation of the individual atoms. For the case where there are more atoms close enough to have an effect, then the light emitted from the first atom can excite more dipoles in the neighbouring atoms. This will lead to an ensemble of atoms, all scattering light back and forth between themselves. The behaviour of such ensemble can be very different compared to just a single atom.

Later, atomic samples with lower densities were investigated, where the dipole-dipole interactions are weaker [86–88]. Depending on the relative phases of the different atomic dipoles, the decay can still be superradiant,

although the decay rate is never as large as in the small sample limit. As a result of the phased preparation, the spontaneous decay preferentially occurs in the directions governed by the initial wavevector of the driving field and the geometry of the atomic ensemble [89]. Other collective interference effects also have been previously observed in many experiments such as quantum interference beats between different quantum states [90] or as a result of the relative motion of atoms [15].

In this chapter, we investigate a single-photon superradiant emission from a microscopic ensemble of ultra-cold rubidium atoms with dimension larger than the optical wavelength. The interference between simultaneously excited collective eigenmodes leads to faster than expected superradiant population dynamics and photon emission.

4.1. Driving field and atom behaviour

This section will discuss the scattering behaviour of a single atom and how this changes when there are two atoms. A simplified scenario of the model is described in Appendix A and [91].

For a single atom, the magnitude of the total field is a combination of the driving field E_{L} and the emission E_{SC} scattered from the dipole. The intensity of the total field is proportional to the field amplitude squared:

$$|E|^2 = |E_{\mathrm{L}} + E_{\mathrm{SC}}|^2 = |E_L + G(r)d_{\mathrm{ge}}\rho_{\mathrm{ge}}(t)|^2 \tag{4.1}$$

where $G(r)d_{\mathrm{ge}}$ is the scattered field at distance r from the dipole and d_{ge} is the dipole matrix element.

The behaviour of a single atom can be calculated using the optical Bloch equations:

$$\dot{\rho}_{ge}(t) = (i\Delta - \Gamma_0/2)\rho_{ge} + i\frac{|d_{ge}|}{\hbar}E_L, \tag{4.2}$$

where we assume that in the weak driving limit the excited state population can be ignored, $\rho_{ee} \approx 0$. This reveals both a transient and a steady state solution:

$$\rho_{ge}(t) = \underbrace{\rho_{ge}^{ss}(1}_{\text{Steady state}} \underbrace{- e^{i\Delta t}e^{-\Gamma_0 t/2}) + e^{i\Delta t}e^{-\Gamma_0 t/2}\rho_{ge}(0)}_{\text{Transient}}. \tag{4.3}$$

Substituting that in equation (4.1), and setting $\Delta = 0$ and $\rho_{ge}(0) = 0$, results in:

$$\begin{aligned} |E|^2 &= |E_L|^2\Big|1 + \frac{\alpha}{|d_{ge}|}G(r)d_{ge}(1 - e^{-\gamma_0 t})\Big|^2 \\ &= |E_L|^2\Big|\underbrace{(1 + \frac{\alpha}{|d_{ge}|}G(r)d_{ge})}_{\text{Steady state}} - \underbrace{\frac{\alpha}{|d_{ge}|}G(r)d_{ge}e^{-\gamma_0 t}}_{\text{Transient}}\Big|^2 \\ &\propto |A - e^{-\Gamma_0 t/2}|^2 = |A|^2 - e^{-\Gamma_0 t/2}(A + A^*) + e^{-\Gamma_0 t}. \end{aligned} \tag{4.4}$$

where α is the atomic polarisability. This results in a decay of the initial transient flash at a rate $\propto \Gamma_0/2$. The fast $e^{-\Gamma_0 t}$ term will not have any effect after a few $\tau_0 = 1/\Gamma_0$.

However, when the driving field is turned off, $E_L = 0$, the magnitude of the total field is defined only by the scattered field term:

$$|E|^2 = |\rho_{ge}^{ss}e^{-\Gamma_0 t/2}|^2 = e^{-\Gamma_0 t}|\rho_{ge}^{ss}|^2 \tag{4.5}$$

and is expected to decay twice as fast as compared to the initial transient flash.

If a second two-level atom is introduced to the system, the behaviour is described using collective eigenmodes, of which there will be two. One, symmetric where both dipoles oscillate in-phase ↑↑ with each other, and one anti-symmetric where they oscillate π out of phase with each other ↓↑. Each atom is a driven classical electric dipole with fixed polarization.

As the atoms are moved further apart, the shift and width of the symmetric (dark blue) and anti-symmetric (light blue) individual eigenmode changes as shown in figure 4.1. A uniform beam will excite only the symmetric in-phase mode and not the asymmetric one, due to the fact that the anti-symmetric mode is out of phase and does not overlap with the symmetric driving field mode vector. Each individual eigenmode is a mode of oscillation with distinct decay rate and resonance frequency. Still, some of the decays will be superradiant and some of them will be subradiant, but the overall system's decay will be faster than any individual eigenmode's decay.

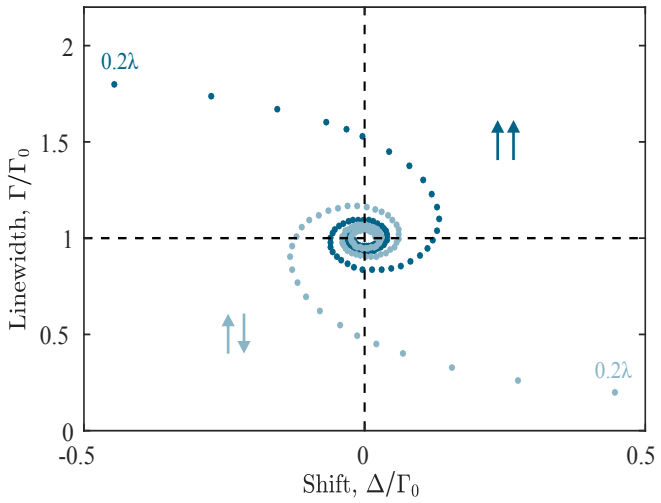

Figure 4.1.: The decay rates Γ and frequency shifts Δ of the individual symmetric (dark blue dots) and anti-symmetric (light blue dots) eigenmodes for two atoms with separation R varying in steps of $0.05\,\lambda$ [91].

The picture is significantly more complicated when there are more than two atoms in a random configuration and different coupling to the Gaussian driving field. That results in a time-dependent decay rate. As a result

of all different oscillation frequencies, the measured intensity of the total scattered electric field is a sum of the beating and interference between the different eigenmodes. However, this does not affect the natural linewidth. It stays independent from the whole beating process, which has been observed experimentally and is discussed later in this chapter.

4.2. Experimental realization

The ^{87}Rb D2 transition, $|5S_{1/2}, F = 2, m_F = 2\rangle$ to $|5P_{3/2}, F' = 3, m'_F = 3\rangle$, is used to measure linewidths and decay rates at different atomic densities and to observe the collective behavior in an ensemble of cold atoms (figure 4.2a). A tightly focused probe light (waist radius $w_0 \approx 1\,\mu m = 1.28\,\lambda_0$) propagates through a microscopic cloud of optically trapped rubiduim atoms, which acts as an optical medium (figure 4.2b). A weak coherent Gaussian pulse is sent to the atomic ensemble and the resulting transmission is detected using a Hanbury-Brown Twiss interferometer (setup described in Chapter 3).

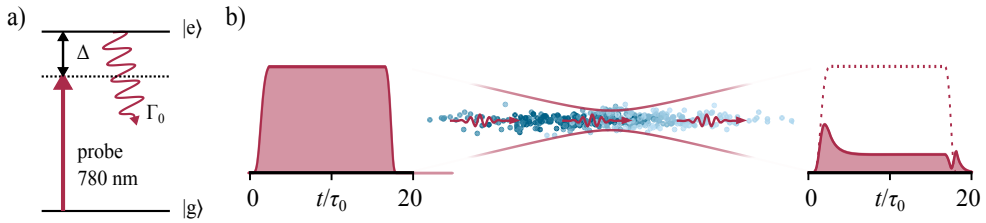

Figure 4.2.: a) A scheme of ^{87}Rb transition - $|5S_{1/2}, F = 2, m_F = 2\rangle$ to $|5P_{3/2}, F' = 3, m'_F = 3\rangle$. b) A probe beam is tightly focused to a $1/e^2$ waist radius $w_0 \approx 1\,\mu m = 1.28\,\lambda_0$ using high NA aspheric lenses into a microscopic atomic ensemble confined in optical tweezers. The first red pulse represents the signal sent to the microscopic atomic ensemble and the second one represents the experimental signal after the microscopic atomic ensemble.

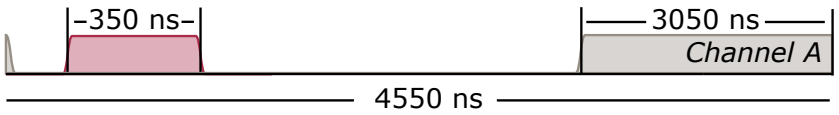

Figure 4.3.: Experimental sub-microsecond sequence to measure signal transmission through the microscopic atomic ensemble. The trapping light is switched off while probing the ensemble to avoid AC Stark shifts.

The sub-microsecond sequence used to control the experiment is shown in figure 4.3. Once the ensemble is prepared, the trap light is turned off for 1.5 µs, during 0.35 µs of which the probe pulse can be applied in

absence of any AC-Stark shifts caused by the trap light. This procedure is repeated between 4000 and 10000 times before reloading the atoms in the magneto-optical trap. The number of repetitions depends on the measured optical depth and atom loss inside the dipole trap.

Instead of applying a separate optical pumping pulse for state preparation, the atoms are optically pumped into the $|5S_{1/2}, F = 2, m_F = 2\rangle$ state by the probe light during the first 1000 to 1200 repetitions. This number again depends on the measured optical depth and atom loss inside the dipole trap. These initial repetitions are not taken into account in our data analysis due to the rapid change of the optical depth during the pumping process. In order to confine the atomic dynamics to just two internal energy levels, we apply an external magnetic field to Zeeman shift the states with different m_F, and then optically pump the atoms into the ground and excited maximal m_F states, which are coupled by probe light with circular polarization.

To measure linewidths and decay rates at different atomic densities, we used the $|5S_{1/2}, F = 1\rangle$ level of the ^{87}Rb ground state which is not addressed by the probe light. That allows us to control a fraction of the atoms in $|5S_{1/2}, F = 2, m_F = 2\rangle$ state by changing the duration of the repumping pulse (between 10 µs and 500 µs) that is applied on the $|5S_{1/2}, F = 1\rangle$ to $|5P_{3/2}, F' = 2\rangle$ transition after loading the dipole trap. As a result the atomic cloud dimensions stay the same and only the number of atoms included in the experiment is changed.

To guarantee that the resonant optical depth remains similar during each data set, it is split into subsets of 10 subsequent cycles which are compared to one another.

4.3. Experimental results

Figure 4.4a and b shows the experimental signal before and after the optical driving pulse for two different optical depths. The decay rates observed for each optical depth, $-\ln(T(\Delta))$, in the experiment are relatively constant until masked by the noise.

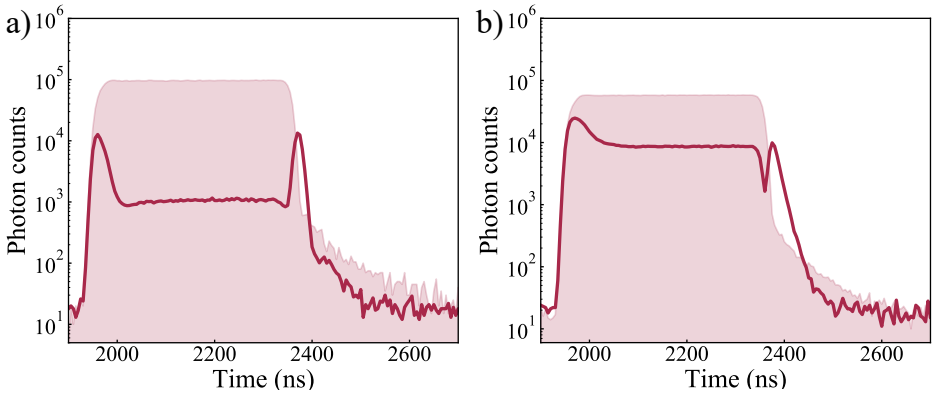

Figure 4.4.: The optical driving pulse for two different optical depths. a) OD = 4.54 and b) OD = 2.91. The shaded pulse is the initial pulse sent to the atoms.

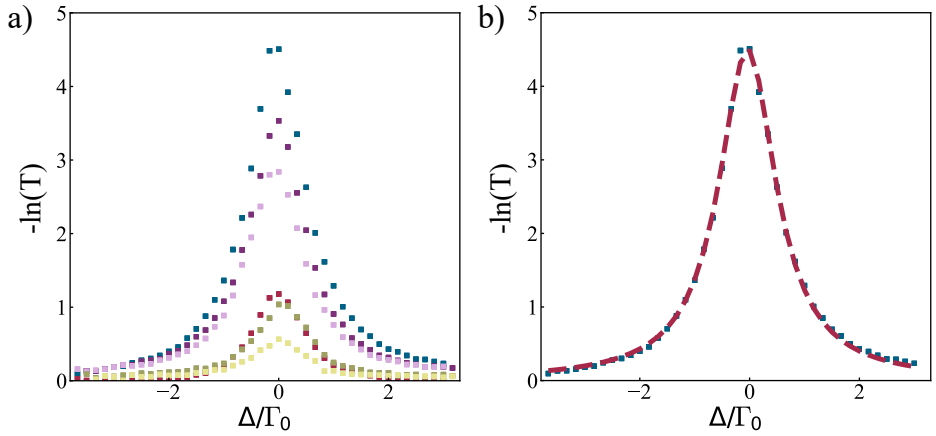

Figure 4.5.: a) Experimental lineshapes at different optical depths. b) Experimental lineshape at high optical depth OD = 4.54 (blue squares) and the coresponding Lorentzian fit (red dashed line).

The resonant optical depth within a measurement is determined by calculating the transmission $T(\Delta) = P_{\text{tot}}/P_0$ while the system is in the steady state (the period where the transmission of the probe pulse through the ensemble remains constant - figure 4.4). For a range of probe detunings Δ (figure 4.5a), a Lorentzian fit of the lineshape of the resulting spectrum $OD(\Delta) = -\ln(T(\Delta))$ has been performed (as shown in figure 4.5b). The resonant peak optical depth during steady state excitation is then given by the amplitude.

The corresponding decay rates have been compared in four different regimes.

- when the driving pulse is on resonance with the atoms (presented in figure 4.6a (blue));
- when the driving pulse is $-2\,\text{MHz}$ detuned from the resonant frequency (presented in figure 4.6a (gold));
- for four different detunings - $0\,\text{MHz}$, $+2\,\text{MHz}$, $+3\,\text{MHz}$, $+4\,\text{MHz}$ (presented in figure 4.6a (cyan));
- for different driving field strength when the driving pulse is on resonance with the atoms (presented in figure 4.6a (purple)).

Both experimentally and numerically, there is a clear positive correlation between the decay rate and the optical depth (figure 4.6a). The observed increase, as the cloud dimensions remain similar, is further evidence that superradiance is a collective effect and not just single atom behaviour [87].

All errorbars stated for each optical depth correspond to the uncertainty in the Lorentzian fits of the lineshapes (as shown in figure 4.6(c and d) calculated by splitting each measurement to 10 subsets.

Normally, a change in the decay rate should also result in a change of the linewidth, because the decay rate and the full width at half maximum (FWHM) linewidth for any given eigenmode are both Γ. In this case however, despite the significant increase in the initial decay rate, both experimentally and numerically, there is a relatively small increase in the linewidth - figure 4.6b. This seems counterintuitive, but it should be considered that the linewidth – decay rate correspondence does not account for the interferences between the different eigenmode frequencies. Furthermore, unlike the decay rate, its observation is not restricted only to the first one or two lifetimes Γ_0. The overall linewidth should contain all eigenmodes excited by the laser. The superradiant modes do not dominate

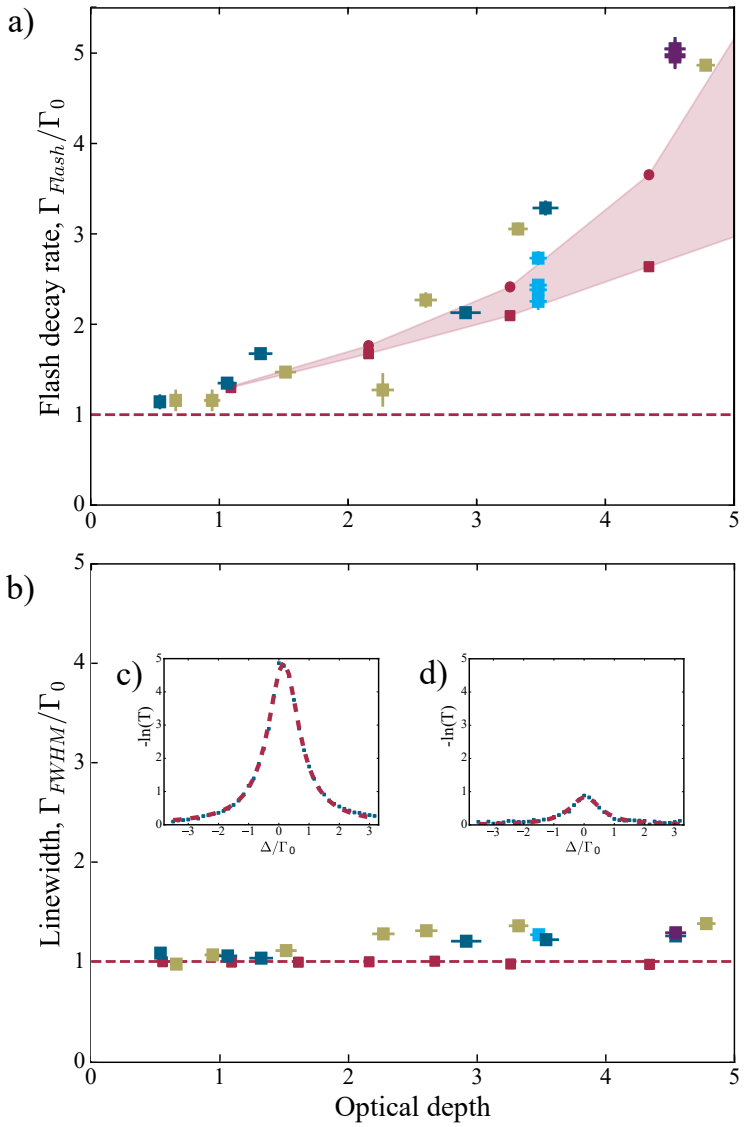

Figure 4.6.: a) Experimental and numerical decay rates on resonance (blue), -2 MHz detuned from resonance (gold), for four different detunings (cyan) and for three different mean photon numbers (purple) as a function of steady state optical depth. The numerics highlight the decay rate immediately after (squares) and τ_0 (circles) the pulse was turned off. b) Full width at half maximum on resonance (blue), -2 MHz detuned from resonance (gold), for four different detunings (cyan) and for three different mean photon numbers (purple) as a function of peak optical depth during steady state excitation for experiment and numerics (red squares). c) and d) Lineshapes at high (OD = 4.89) and low (OD = 0.84) optical depth for the experiment on resonance (blue doted lines) and the corresponding Lorentzian fit (red dashed lines).

these various components. They only contribute at the beginning of the decay process. Experimentally, it is possible to observe decay rates over a much longer time [77, 92]. In that case the linewidth should start increasing as well.

Varying the detuning (between 0 MHz and 4 MHz) for the same optical depth (OD = 3.69) is shown in figure 4.6 (in cyan) as well as in figure 4.7. It is easy to see that a detuning change in such a small range does have a small impact on the decay rate of the coherent flash.

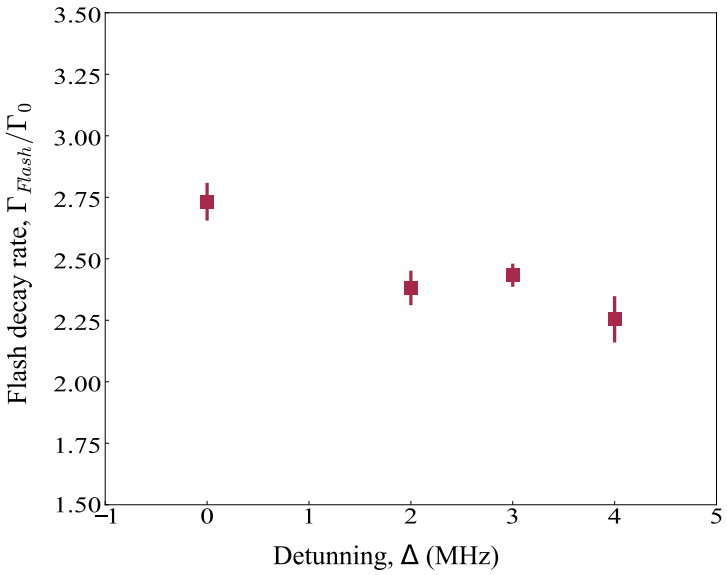

Figure 4.7.: Experimental decay rates for four different detunings (0 MHz, +2 MHz, +3 MHz, +4 MHz).

The experimental results outlined above, were all performed in a weak driving regime, as the mean number of photons per pulse is approximately 1.5. As shown in figure 4.6 (in purple) as well as in figure 4.8, the experiment was also repeated for different driving fields. Results are shown for different photon mean numbers of 0.5, 1.5 and 4. The figure clearly shows that there is no change in the decay rate as a function of the driving field, where the optical response remains in the linear regime. The steady state optical depth is OD = 4.54.

The second-order correlation function $g^2(0)$ has also been analyzed for different durations within the flash pulse, as shown in figure 4.9 for the whole pulse, and figure 4.10 for two different time slots within the pulse.

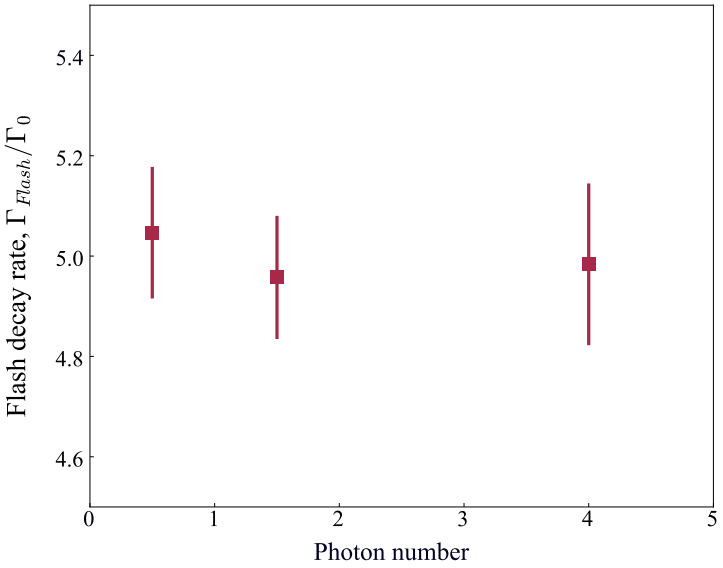

Figure 4.8.: Experimental and numerical decay rates for three different mean photon numbers 0.5, 1.5 and 4.

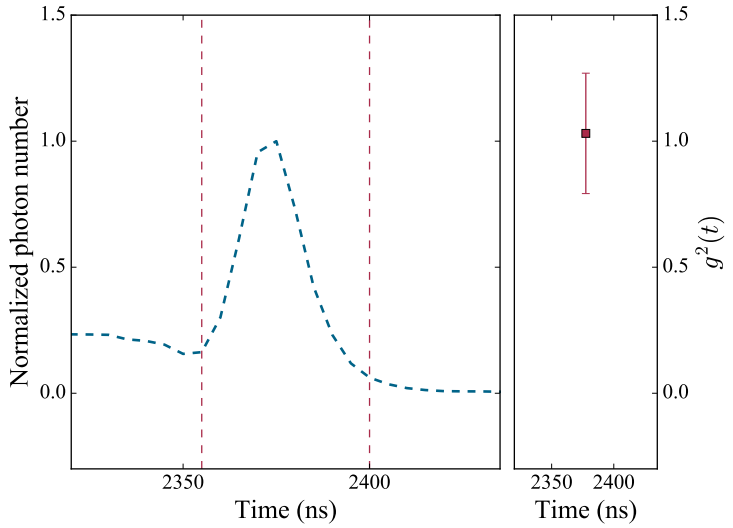

Figure 4.9.: The single correlation function $g^2(0)$ as a function of time duration for the whole pulse. a) The blue line represents the flash pulse while the red vertical lines represent the region within which $g^2(0)$ has been calculated. b) The calculated value of $g^2(0)$ within that region and the corresponding error.

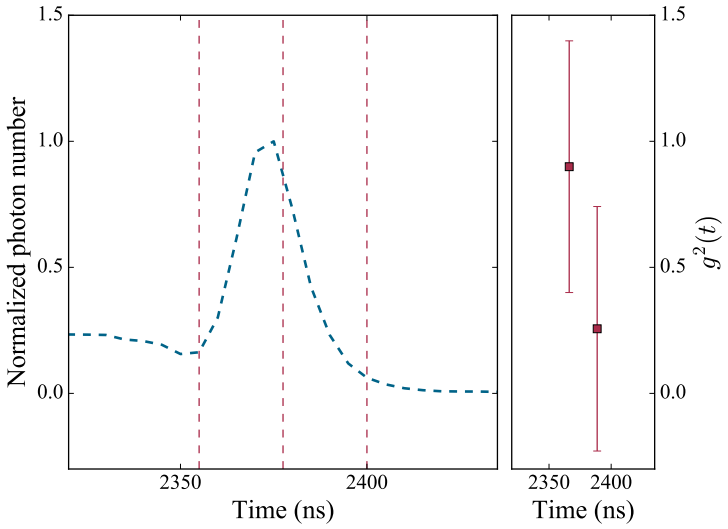

Figure 4.10.: The single correlation function $g^2(0)$ as a function of time duration for two different time slots within the pulse. a) The blue line represents the flash pulse while the red vertical lines represent the region within which $g^2(0)$ has been calculated. b) The calculated value of $g^2(0)$ within these regions and the corresponding errors.

Splitting to more then one time slot needs a sufficient amount of data and a good signal-to-noise ratio. This is the reason why the second region in figure 4.10b gives a $g^2(0)$ less than one, and also the much larger errorbars. The approximate value of the single correlation function $g^2(0)$ remains 1 and as expected the flash emission is classical state of light. The method used to analyze the photon measurements and calculate the single correlation function $g^2(0)$ is described in Appendix C.

It is also interesting to have a look at the initial transient peak which appears before the system is settled down into a steady state (figure 4.11). The region of interest is marked with the two blue dashed lines. This flash should be a result of interference between the driving field E_L and the scattered dipoles emission E_{SC}.

As expected the overall behaviour of the ensemble can be very different from the behaviour of a single atom, and its expected decay rate proportional to $\Gamma_0/2$. Again the overall decay is a combination of all individual dipoles decays, which are shifted off-resonance with respect to each other. Figure 4.12 shows the calculated decay rates of the initial peak on resonance as a function of steady state optical depth. The decay rate is calculated

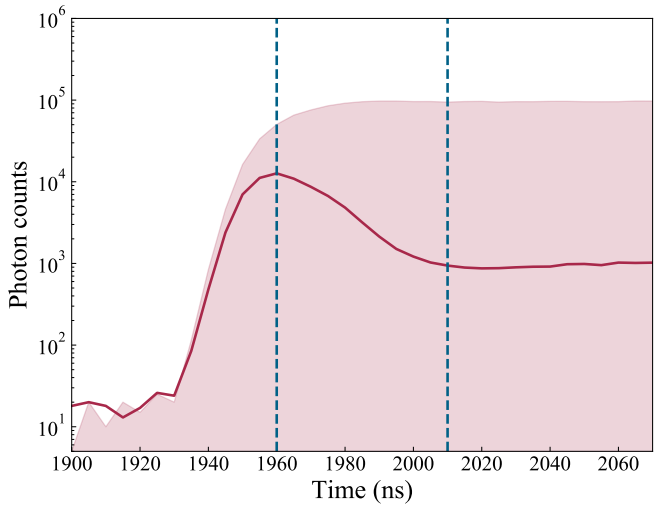

Figure 4.11.: A slice of the optical driving pulse for optical depths OD = 4.54. The shaded pulse is the initial pulse sent to the atoms. The blue dotted lines correspond to the region within which the decay rates have been calculated.

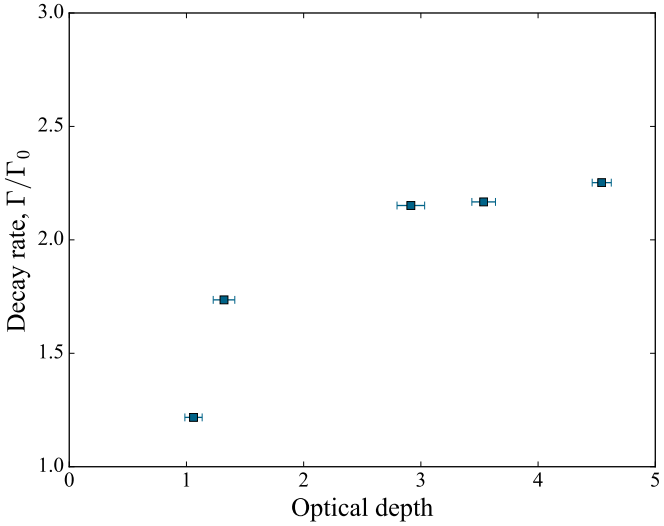

Figure 4.12.: Experimental decay rates of the initial transient peak on resonance, immediately after the driving field is turned on and before the system is settled down into a steady state, as a function of steady state optical depth.

immediately after the pulse was turned on and before the system is settled down into a steady state. The increase of the decay rate when increasing the optical depth is further proof that this is a collective effect and not a single atom response.

Although there is good agreement in the obtained decay rates of the coherent superradiant flash between experiment and numerical simulations, there are still factors which can contribute and affect the measured optical depth such as the exact number and positions of the atoms in the cloud, and Gaussian beam misalignment. Atomic dephasing also may reduce the experimental optical depth, whilst not affecting the decay rate.

Summary

The interference between eigenmodes of collectively excited ensembles of optical dipoles can lead to a decay faster than any individual, superradiant eigenmode. The decay is not only due to the decay of the individual eigenmodes but also depends on their frequency shifts. In the future, a Rydberg character could be introduced to the flash which should result in decay rates proportional to the Rabi frequency of the dressing field and proportional to the lifetime of the used Rydberg state. The Rydberg character should also suppress the $g^2(0)$ within the dressed flash. Numerical simulations and experimental data of a Rydberg dressed flash could provide a different approach in which to exploit collective mode engineering in quantum technology applications.

5. Storage and retrieval of optical photons, Blockade vs. Dephasing model.

5.1. Introduction

Photons have been deemed ideal carriers of quantum information due to their weak free-space interactions [93]. Consequently, photons very rear interact with each other in vacuum. A solution to make individual photons interact is to convert one photon into an atomic excitation. Rydberg atoms, due to their strong interactions, can be used to achieve strong photon-photon interactions by mapping the photon states onto Rydberg excitations [27, 37]. The dipole-dipole interactions give rise to the Rydberg blockade suppression effect and limit additional excitations. Additionally, the relatively long lifetime of Rydberg atoms allow the observation of these photon-photon interactions. The ability to vary the interaction strength between Rydberg atoms unlocks the potential to develop scalable quantum information networks.

This chapter is based on experiments with two spatially separated atomic clouds (figure 5.1), performed in collaboration with Hannes Busche, Simon Ball and Paul Huillery. In Sections 5.4 and 5.5, different models are introduced to simulate and explain the experimentally gathered photon statistics.

Contactless photon-photon interactions depend on the amount of Rydberg excitation, within a single medium, and on the distance between the spatially separated mediums containing these excitations. The first condition is related either to the Rydberg blockade radius, which can be controlled by; either changing the linewidth of the control laser, changing the effective size of each cloud, controlled by the focus of the signal light, or by only exciting some of the atoms to the intermediate $|5P_{3/2}\rangle$ state. In the desired regime only a single Rydberg excitation would be possible in each of the clouds. The interaction effect can then be read out by measuring

the sub-Poissonian statistics of the retrieved photons. This is defined by the simplified second order spatial correlation function $g^{(2)}(t)$, expressed by the number of detected retrieved photons [94].

5.2. Storage and retrieval of optical photons

The single Rydberg excitation state is a superposition of quantum states characterized by a single atom being excited into a Rydberg state. For example a collective superposition state with a single atomic excitation is:

$$|R\rangle = \frac{1}{\sqrt{N}} \sum_j \Big(|r_j\rangle \otimes_{k\neq j} |g_k\rangle \Big) \tag{5.1}$$

where $|r_j\rangle$ and $|g_k\rangle$ correspond to a state in which a single atom j is excited to the Rydberg state and all other atoms are left in the ground state. N is the number of entangled atoms sharing the Rydberg excitation.

The excitation of a doubly-excited state is excluded as a result of the blockade mechanism. The many-body character of the excitation can be treated by introducing an entangled collective state. The collectiveness of this excited state leads to a collective enhancement of the oscillation between ground and excited state - the Rabi frequency - $\sqrt{N}\Omega$ [95, 96].

This collective state $|R\rangle$ should also include the specific phase of the photons $\phi(\vec{r}_j)$, which originates from the phase of the excitation lasers at the position of each atom j excited to the Rydberg state, and the excitation probabilities $\epsilon(\vec{r}_j)$ at position $\vec{r}_j$. This ensures that the retrieved photon will be in its originally imprinted spatial mode. The collective spin-wave state is defined as:

$$|R\rangle = \frac{1}{\sqrt{\sum_j \epsilon(\vec{r}_j)^2}} \sum_j \epsilon(\vec{r}_j) e^{i\phi(\vec{r}_j)} \Big(|r_j\rangle \otimes_{k\neq j} |g_k\rangle \Big). \tag{5.2}$$

To understand better the storage process in the experiment using electromagnetically induced transparency, we should discuss the propagation of the signal photon through this atomic medium. This can be described in terms of quasi-particles, known as polaritons [38], and corresponds to superpositions of atomic coherence and electromagnetic excitations. Using electromagnetically induced transparency scheme for storing signal photons, restricts the population in the intermediate level $|e\rangle$. The dark-state polariton field is:

$$\psi(z,t) = \underbrace{\cos\theta \varepsilon_S(z,t)}_{\text{Electromagnetic part}} - \underbrace{\sin\theta \sqrt{N} \rho_{gr}(z,t) e^{i(k_S+k_C)z}}_{\text{Atomic part}} \tag{5.3}$$

where the signal field is $\varepsilon_S(z,t)$, the wave vector of the spin-wave is given by $(k_S + k_C)$, the mixing angle θ comes from the group index as $\tan\theta^2 = n_g r$,

and $\rho_{gr}(z,t)$ is the coherence between the states $|g\rangle$ and $|r\rangle$. The coherence term also represents the direct coupling between these two states.

The group velocity is given by $v_g = c\cos\theta^2$ and for $\theta \to 0$ the character of the dark state polariton is dominated by the photonic component and $v_g \to c$. If $\theta \to \pi/2$, the group velocity $v_g \to 0$ and the electromagnetic field is completely transferred to the atomic coherence.

Controlling the group velocity v_g in the range between 0 and c, by controlling the Rabi frequency of the coupling beam Ω_C (equation (2.28)), allows the storage of photons as stationary collective Rydberg excitations. The shape and the coherence of the photon are imprinted in the phase and amplitude of this spin-wave.

The stored photons can be later retrieved from the atomic medium by increasing Ω_C. The group velocity v_g will increase and transfer back the atomic coherence into an electromagnetic excitation. The phase of the signal photons, previously imprinted and conserved in the spin-wave, should lead to a retrieved electromagnetic field emission with the same spatial mode as the original signal field.

To understand this directionality in the retrieval process, we now look at an example of a spin-wave with a single atomic excitation:

$$|\psi\rangle = \frac{1}{\sqrt{N}} \sum_{j=1}^{N} e^{i\phi_j} |r_j\rangle, \tag{5.4}$$

where $|r_j\rangle = |g_1 g_2 \ldots r_j \ldots g_N\rangle$ correspond to a state in which a single atom j is excited to a Rydberg state and all other atoms are left in the ground state $|g\rangle$. The phase factors are given by $\phi_j = (\vec{k}_S + \vec{k}_C) \cdot \vec{r}_j$, where $\vec{r}_j$ is the position of atom j.

Since the directionality of the retrieval relies on constructive interference between each term, it should increase with the number of atoms used to imprint the photon or the optical depth of the medium. The retrieval efficiency is mainly reduced by motional dephasing of the atoms during the storage time. Such motion disturbs the phase pattern imprinted into the medium. As long as the phase factors ϕ_j remain in relative phase, the photon will be collectively emitted back into its original signal spatial mode. The retrieval efficiency κ_{ret} decays exponentially with time [97]:

$$\kappa_{ret} = e^{-(t^2/\tau^2)}, \tag{5.5}$$

where τ is the $1/e$ lifetime of the spin-wave, given by:

$$\tau = \frac{1}{(\vec{k_S} + \vec{k_C}) \cdot \vec{v}} \tag{5.6}$$

with v as the velocity of the atoms.

The electromagnetically induced transparency storage scheme gives an additional requirement related to the finite width of the transparency window, $\gamma_S < \Delta_{EIT}$, where γ_S is the linewidth of the signal photons. Frequency components outside this window are scattered by the medium. Reducing Ω_C leads to a reduction in the bandwidth of the signal pulse that is transmitted.

On the other hand, the initial storage of the signal light pulse requires spatial compression, such that it spatially fits inside the medium. That gives a requirement of either a minimal length $l > v_g t_S$, a very short pulse time t_S, or a low value of Ω_C.

As a result, to have enough atoms to store the signal light pulse and get better retrieval efficiency, the optical depth (OD) of the medium should be $OD \gg 1$ and the control light should be switched off adiabatically.

5.3. Experimental realization

The level digram required for the experiments outlined in this chapter is highlighted in figure 5.1a. A weak Gaussian coherent pulse at 780 nm drives the transition $|g\rangle = |5S_{1/2}, F = 2, m_F = 2\rangle$ to $|e\rangle = |5P_{3/2}, F' = 3, m'_F = 3\rangle$ while a strong coupling beam at 480 nm drives $|5P_{3/2}, F' = 3, m'_F = 3\rangle$ to $|nS_{1/2}\rangle$ transitions. The beams are counter-propagating with opposite circular polarisation. Part of the signal photons are stored as polaritons in the Rydberg state.

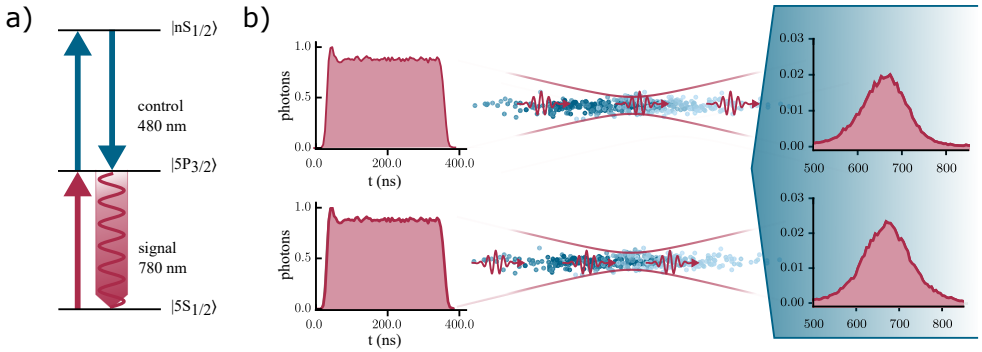

Figure 5.1.: A schematic of the spatially separated channels. a) The Rydberg electromagnetically induced transparency ladder scheme in ^{87}Rb. b) A schematic of two spatially separated channels. The sent and retrieved signal light detected in the experiment is represented by the pulses before and after the atomic clouds. A signal light beam is tightly focused into a cigar-shaped cloud of cold ^{87}Rb atoms which are trapped with a far red-detuned 910nm optical tweezers. The distance between the channels is adjustable.

The signal light is tightly focused (waist $1/e^2$ radius $w_0 \approx 1\,\mu\text{m} = 1.28\,\lambda_0$) and propagates independently through two microscopic clouds of optically trapped ^{87}Rb atoms, acting as two spatially separated optical media. A schematic of the two mediums is shown in figure 5.1b. The corresponding optical setup for this experiment is described in Chapter 3. The estimated dimensions of each cigar-shaped atomic ensemble is 1.5 µm in radial size and 20 µm in axial size. The dimensions of the atomic ensembles are difficult to measure in the current experimental setup, but the atoms should occupy a fraction of the volume defined by the size of the dipole trapping beam. For these experiments, the trapping beam has a waist $1/e^2$

radius of 4.5 µm and Rayleigh range of 70 µm.

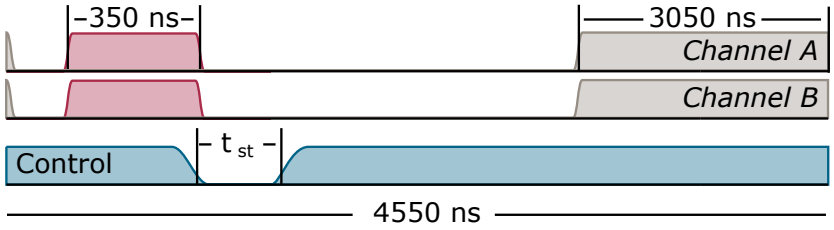

Figure 5.2.: The micro-second storage sequence for the electromagnetically induced transparency signal and control fields and the optical trap.

The storage protocol is shown in figure 5.2. Once the ensembles are prepared, the trap light is switched off for 1.5 µs. During that time the atoms are probed with a 350 ns square pulse of signal light. As a result the signal pulse is applied in the absence of any AC-Stark shifts due to the trap light. The control light power is reduced to zero, converting the signal photons into collective Rydberg excitations. The incoming signal pulses contain a mean of 2.2 ± 0.2 photons. After the storage time t_{st}, the photons are retrieved by restoring back the control field. The switching of the control field is controlled by a polarization switching electro-optic modulator, with response time of approximately 100 ns. The measured control light Rabi frequency is $\Omega_C/2\pi = 9 \pm 1$ MHz. The resulting transmission is detected using the Hanbury-Brown Twiss interferometer setup, described in Chapter 3. Each one of the data points is obtained over 25 million storage and retrieval cycles with 25,000 repetitions within a single magneto-optical trap loading.

The minimum separation between the two atomic ensembles is 10 µm. Any separation smaller than that results in cross-talk between the channels. The absorption cross-talk is measured by observing the effect on the transmission of the signal light on the neighbouring channel while there are no atoms in that particular one. The trap light was filtered and only the signal light was transmitted for this specific channel. The cross-talk data for the minimum allowed separation is shown on figure 5.3. Increasing the separation reduces the cross-talk. The two channels are spatially independent after 10 µm. Any separation less than that value leads to a cross-talk greater than 5%.

To maintain a relatively constant coupling Rabi frequency Ω_C, throughout each different measurement, an Autler-Townes splitting of the absorption line is made at $|nS_{1/2}\rangle = |30S_{1/2}\rangle$ because of the high power required

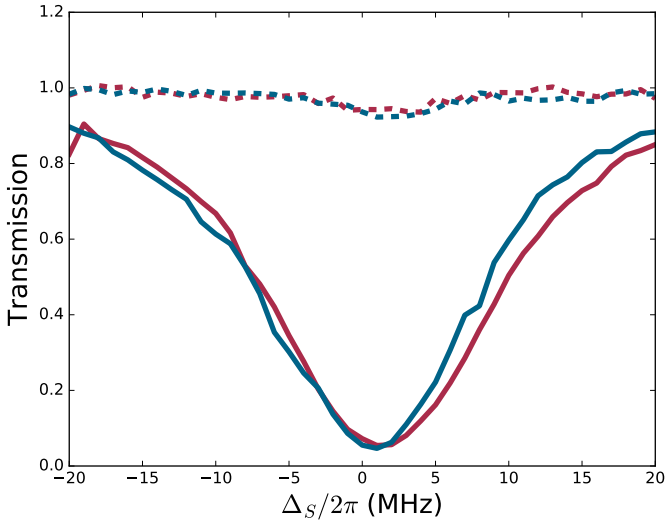

Figure 5.3.: Cross-talk between the two channels. The signal light transmission in channel A (red) and channel B (blue) for 10 µm separations. For the spectra shown as solid lines both atomic media are present. The corresponding colored dashed lines represents a case where the dipole trap in this channel is blocked and the signal detected comes from the nearby channel's atomic cloud.

for such measurements at higher Rydberg levels, such as $|80S_{1/2}\rangle$. Figure 5.4 shows Autler-Townes splitting for various laser powers. The obtained Rabi frequencies, $\Omega_C/2\pi = 0\,\text{MHz}$ (red), $\Omega_C/2\pi = 7.92 \pm 0.98\,\text{MHz}$ (blue) and $\Omega_C/2\pi = 14.59 \pm 0.11\,\text{MHz}$ (black), are calculated using the Beer-Lambert law and the three-level susceptibility from equation (2.26). The overlapping of the coupling light and the channels is also checked before each measurement to ensure that the control light intensity is equal for both channels.

The control light is switched on and off before and after the signal light pulse to ensure that its Rabi frequency Ω_C stays relatively constant throughout the entire duration of the signal pulse.

Figure 5.5 shows a storage-retrieval histogram of photon events for Rydberg state $|80S_{1/2}\rangle$. The grey trace shows the signal laser pulse in the absence of atoms, the red trace shows the signal laser light in the presence of atoms and the detected retrieved photons and the blue one shows the coupling intensity recorded on a photodiode. The discussed collective flash emission in Chapter 4 is also visible, and appears just after the signal light

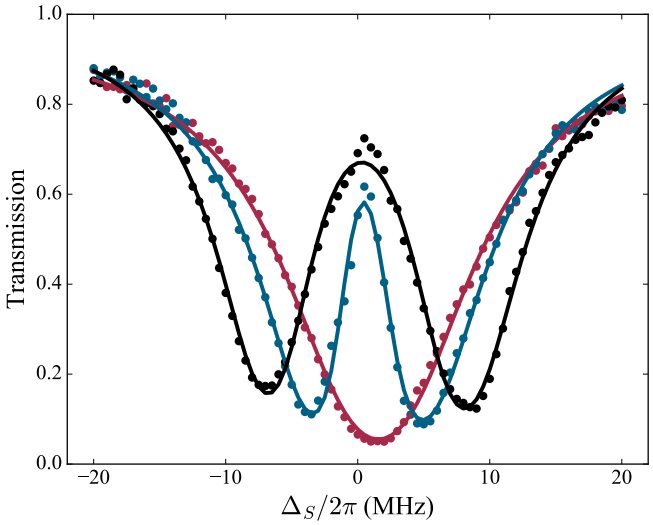

Figure 5.4.: Autler-Townes splitting at $|30S_{1/2}\rangle$ as a function of the signal light detuning for three different coupling powers. The calculated values are $\Omega_C/2\pi = 0\,\text{MHz}$ (red), $\Omega_C/2\pi = 7.92 \pm 0.98\,\text{MHz}$ (blue) and $\Omega_C/2\pi = 14.59 \pm 0.11\,\text{MHz}$ (black).

is switched off.

Two influences on the photon-photon interactions were explored initially:

- the separation between the clouds,
- the interaction strength at a fixed distance between the clouds.

After the results were gathered it was only natural to look for a theoretical model, that could describe the system. The first step was to create a model based on the Rydberg blockade effect described in Section 5.4. Due to the experimentally observed suppression even beyond the blockade radius, a research was made in a different direction to explain this particular observed behaviour - Section 5.5. To additionally provide proof of the chosen method, the storage time dependence of the retrieved photons was taken into consideration. The data gathered from the experiment was processed using the method described in Appendix C. The second order correlation function of the retrieved photons was used as an estimation criteria for a single channel and for both channels:

$$g^{(2)}_{A/B} = \frac{\langle N_{A/B}(N_{A/B}-1)\rangle}{\langle N_{A/B}\rangle^2}, \tag{5.7}$$

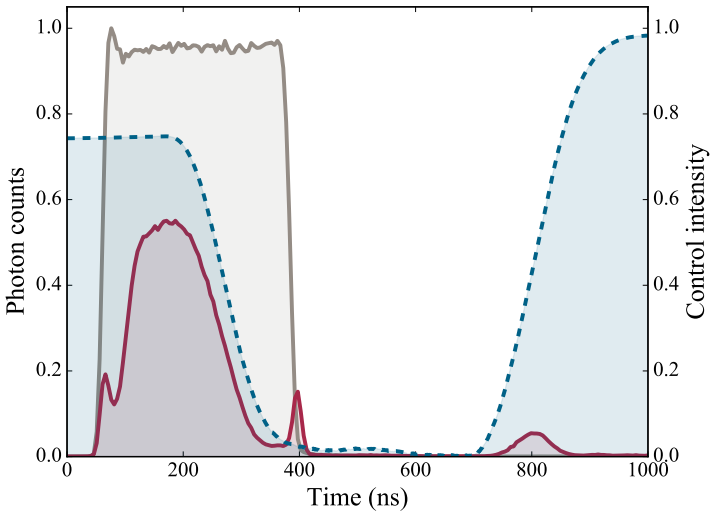

Figure 5.5.: A histogram of detected photon events at Rydberg state $|80S_{1/2}\rangle$. The grey trace shows the signal laser pulse in the absence of atoms, the red trace shows the signal laser light in the presence of atoms and the detected retrieved photons and the blue one shows the coupling intensity recorded on a photodiode.

$$g^{(2)}_{AB} = \frac{\langle N_A N_B \rangle}{\langle N_A \rangle \langle N_B \rangle} \tag{5.8}$$

where N is the number of detected retrieved photons, the indices A/B and AB indicates measurements from two different channels, either A or B, or AB simultaneously.

In the absence of interactions, $g^{(2)} = 1$. If the interaction strength is strong enough to influence a nearby stored photon, the second order correlation function $g^{(2)} < 1$ which indicates the retrieval of non-classical light with sub-Poissonian photon counting statistics. A $g^{(2)} = 0$ means a retrieval of no more than a single photon. The timing resolution is the width of the retrieval window. Errors in the second order correlation functions $g^{(2)}$ are calculated by splitting each dataset into multiple subsets, calculating $g^{(2)}$ for each subset and calculating the standard error over all subsets. In case of simultaneous retrieval, the presence of a photon stored in the first cloud should effect the storage in the second one.

5.4. Rydberg blockade simulation

The effect of the Rydberg blockade can be easily explained as a spatial extension of a restricted medium, in which a single excitation in the medium entirely prevents other excitations. For cases where the clouds are in scale with the blockade radius r_b (the blockade radius is big enough) only one photon can be stored in either of the two photonic channels. On the other hand, if the length of the atomic cloud exceeds the blockade radius r_b, the number of photons stored in each channel is only partially reduced by the blockade, although the channel separation is less than the blockade radius.

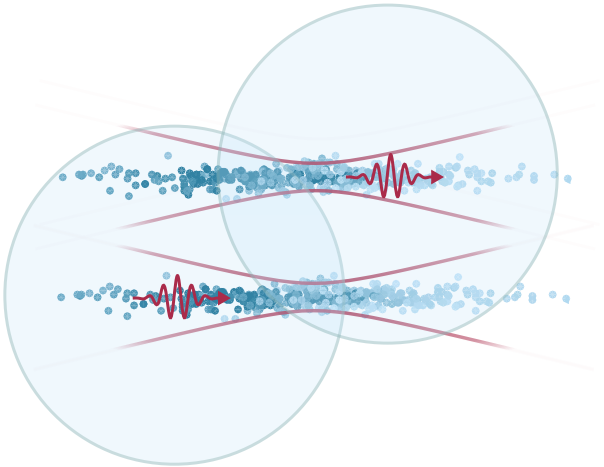

Figure 5.6.: A schematic of the Rydberg partial blockade regime. The experimental cigar-shaped cloud dimensions allow more than a single excitation in each cloud to exist.

A fully blockade regime between the two spatially separated mediums could not be achieved, due to the cross-talk which appears in separations less than 10 µm, and at the same time the tuning range of the coupling laser which limits the high Rydberg states that can be reached. Still, the partial blockade regime as shown in figure 5.6 is of interest for us as the experimental cigar-shaped cloud dimensions allow more than a single excitation in each cloud to exist.

The numerical simulation used to explain the experimental results is relatively simple compared to the complex theory which describes the experiment. The steps of the simulation are presented in figure 5.7.

Initially two clouds with Gaussian distributed atoms are created. The number of atoms in each cloud is limited to 1000. The clouds are shifted

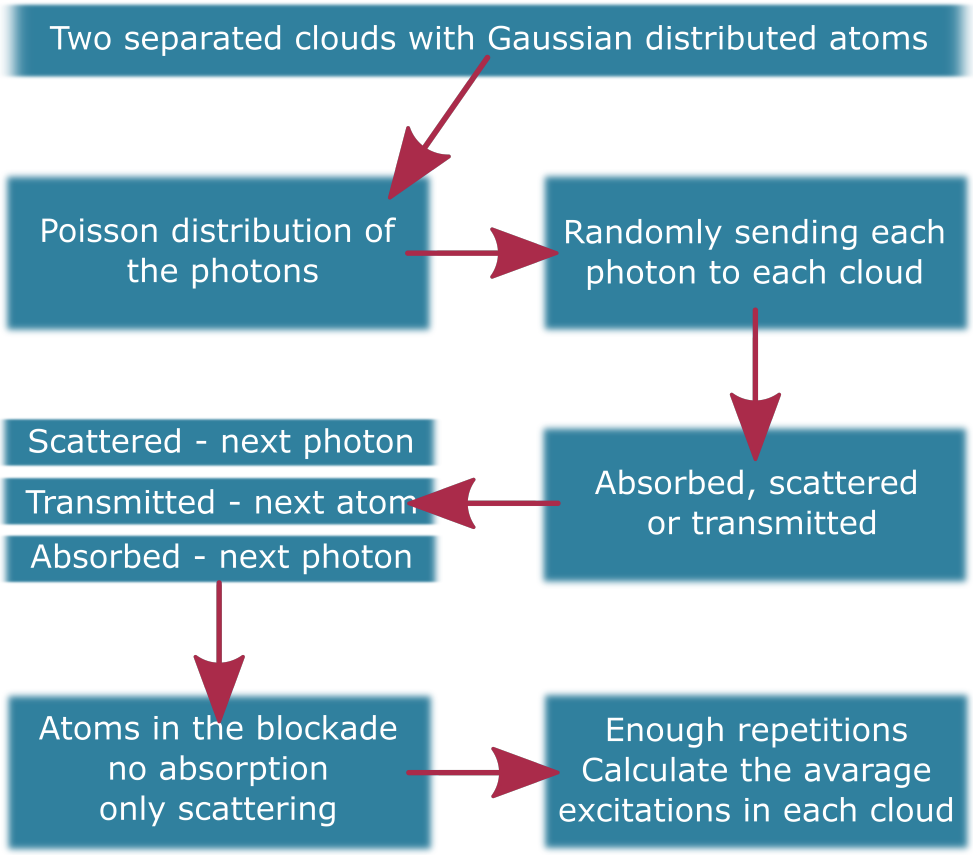

Figure 5.7.: A scheme of the Rydberg blockade model used to simulate the photon statistics gathered from the experiment.

at the required distance given by the different separations used in the performed measurements - figure 5.8.

Photons with a Poisson distribution are sent to both clouds. In order to replicate the experiment, the photons are randomly split and sent to either one of the clouds, to simulate a beam splitter behaviour.

Each one of the atoms inside the clouds can absorb, scatter or transmit a photon with a given rate (for the results presented later in this section the absorption and scattering probability rates are fixed at 0.001). Each absorbed photon results in a blockade as shown in figure 5.9 and within its radius the atoms cannot absorb anymore, although can still scatter future photons. If the sent photon is not absorbed or scattered by any of the atoms, it is simply transmitted by the cloud.

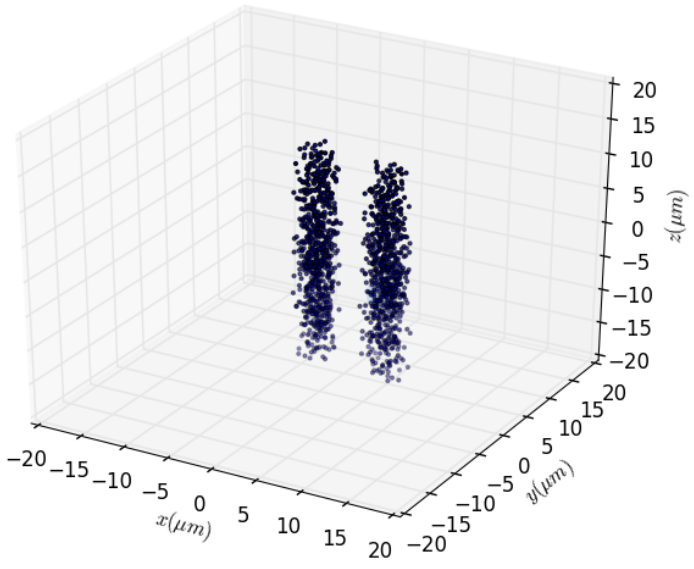

Figure 5.8.: Two clouds with Gaussian distributed atoms shifted from one another at a distance of 10 µm.

The calculation of the second order correlation function $g^{(2)}$ requires a large number of coincidences so that the described sequence should be repeated hundreds of thousands of times per each experimental data point, before the target precision is reached.

The model contains many free parameters which require some initial estimation. Since the basic calculation requires hours, a fitting process of these parameters is not feasible. One of the unknown parameters currently in the experiment is the cloud size which varies between each $g^{(2)}$ measurement. A simple solution to that was to examine the calculated second order correlation function $g^{(2)}$ for different longitudinal sizes between 30 µm and 60 µm (figure 5.10) of the clouds. Based on the experimental results, for single channel and for both channels simultaneously, we were able to approximate the effective cloud size. The channels' separation distance is set at 10 µm, and $r_b = 10$ µm is used for the Rydberg blockade radius, as this is the approximate blockade radius at Rydberg state $|80S_{1/2}\rangle$. From figure 5.10, it is clear that the cloud size has a major impact on both

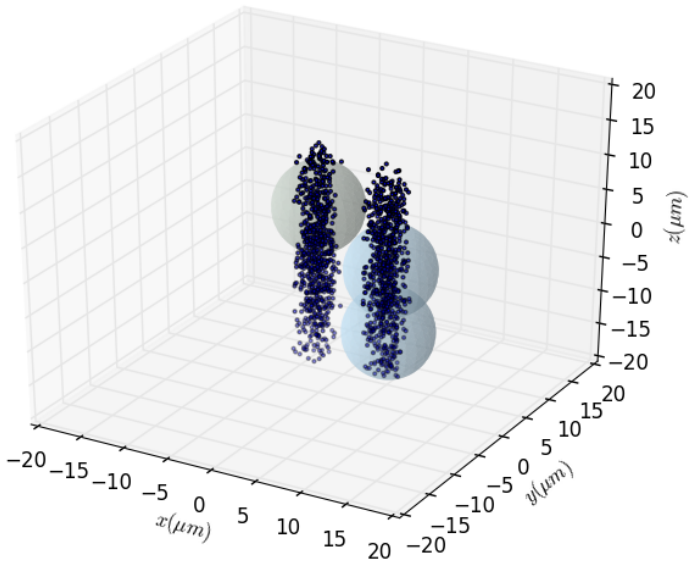

Figure 5.9.: Two clouds with Gaussian distributed atoms shifted from one another at a distance of 10 µm with excited Rydberg atoms and a corresponding blockade radius of 6 µm.

single-correlation and cross-correlation functions as it defines how many photons can be stored simultaneously. The effective longitudinal cloud size was estimated to be in a range between 25 µm and 30 µm.

Next we investigated the influence of the Rydberg blockade radius at two different cloud sizes - figure 5.11. The obtained results for the cross-correlation function $g_{AB}^{(2)}$ show that better agreement occurs between experiment and theory for a theoretical blockade radius of 14.6 µm (compared to the experimental value of approximately 10 µm). It is also clear that a small change in the cloud size does not affect the reproducing of the data when varying the separation between the two channels.

Similar behaviour can be observed in the calculated dependence between the single-correlation function $g_{A}^{(2)}$ and the Rydberg blockade radius (figure 5.12). Again better agreement occurs between experiment and theory for

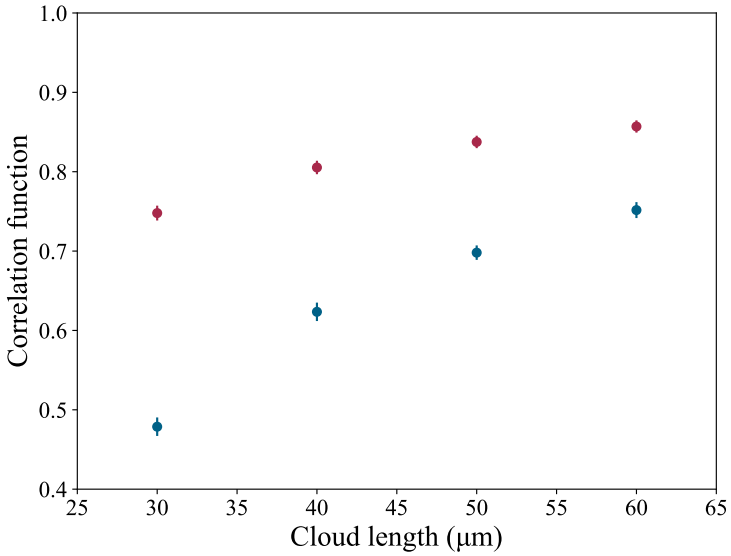

Figure 5.10.: Calculated cross-correlation function $g^{(2)}_{AB}$ (red circles) and single-correlation function $g^{(2)}_{A}$ (blue circles) dependence on the clouds length for four different longitudinal cloud sizes between 30 µm and 60 µm. The Rydberg blockade radius is fixed at 10 µm and the distance between the clouds is 10 µm.

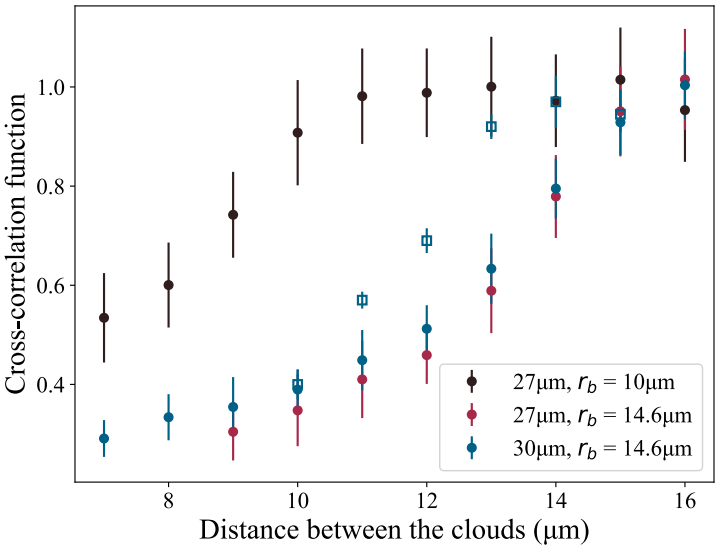

Figure 5.11.: Cross-correlation function $g^{(2)}_{AB}$ measured in the experiment (blue squares) for different clouds separation at level $|80S_{1/2}\rangle$ and the calculated cross-correlation function $g^{(2)}_{AB}$ (blue, red and black circles) for two different longitudinal cloud sizes and two different Rydberg blockade radii.

a theoretical blockade radius of 14.6 µm. The consistently constant values for different runs of the simulation gives a validation of that the model is stable.

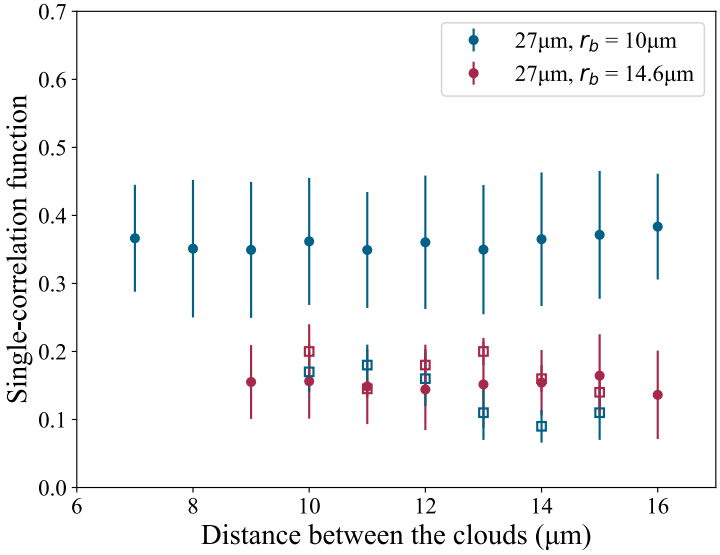

Figure 5.12.: Single-correlation function $g_A^{(2)}$ measured in the experiment (blue and red squares) at level $|80S_{1/2}\rangle$ and the calculated single-correlation function $g_A^{(2)}$ (blue and red circles) for two different Rydberg blockade radii.

The numerical model allows us to investigate different influences over the cross $g_{AB}^{(2)}$ and single-correlation function $g_{A/B}^{(2)}$. In figure 5.13, the g^2 function is calculated as a function of the number of photons initially sent to the atomic cloud. The results are shown for the Rydberg state $|80S_{1/2}\rangle$, where the cloud size is fixed at 27 µm(3 µm) in the longitudinal (radial) direction. The numerical results for the cross-correlation function $g^{(2)}$ are in a good agreement with the mean number of photons used in the experiment which is 2.2 ± 0.2.

The effect of the interaction strength for a single channel and two channels (figure 5.14) has also been investigated. The calculated results from the simulation for different Rydberg states (between $|50S_{1/2}\rangle$ and $|95S_{1/2}\rangle$ show very good agreement with the obtained experimental data points. A small change in the cloud size should not affect the reproduction of the experimental data.

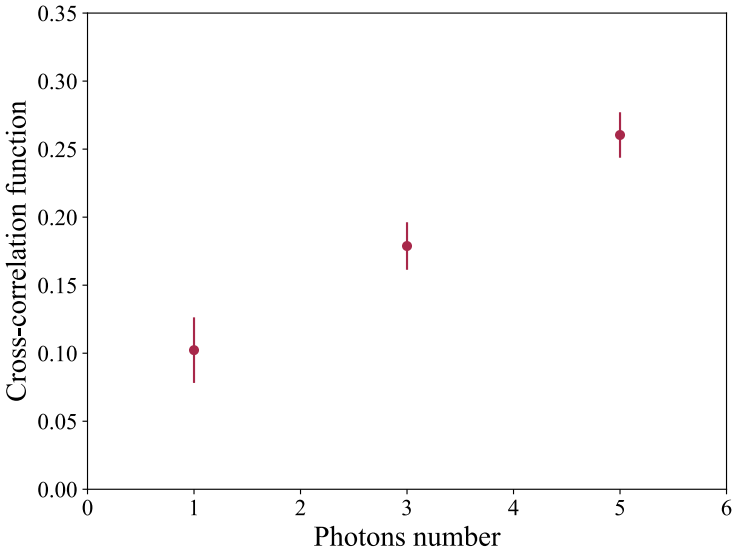

Figure 5.13.: Calculated cross-correlation function $g^{(2)}_{AB}$ for different number of photons sent to the clouds at Rydberg state $|80S_{1/2}\rangle$. The clouds have a longitudinal size of 27 µm and a radial size of 3 µm.

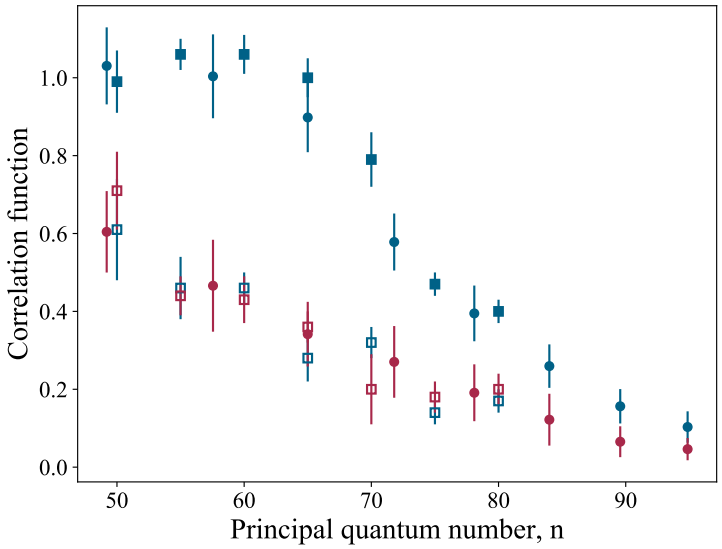

Figure 5.14.: Cross-correlation function $g^{(2)}_{AB}$ (blue squares) and single-correlation function $g^{(2)}_{A}$ individually (blue and red squares(channel A and channel B respectively)) measured at different Rydberg states for a fixed clouds separation of 10 µm. The result from the theoretical model for the cross (blue circles) and single (red circles) correlation function corresponds to a cloud longitudinal size of 27 µm and a radial size of 3 µm.

In both cases, for the single and cross-correlation function $g^{(2)}$, the theory does not vary significantly with the cloud size between 25 µm and 27 µm. As a result the effective longitudinal cloud size has been set to 27 µm because both experimental single and cross-correlation functions show best agreement with theoretical fit, as shown in figure 5.14 with red and blue circles respectively.

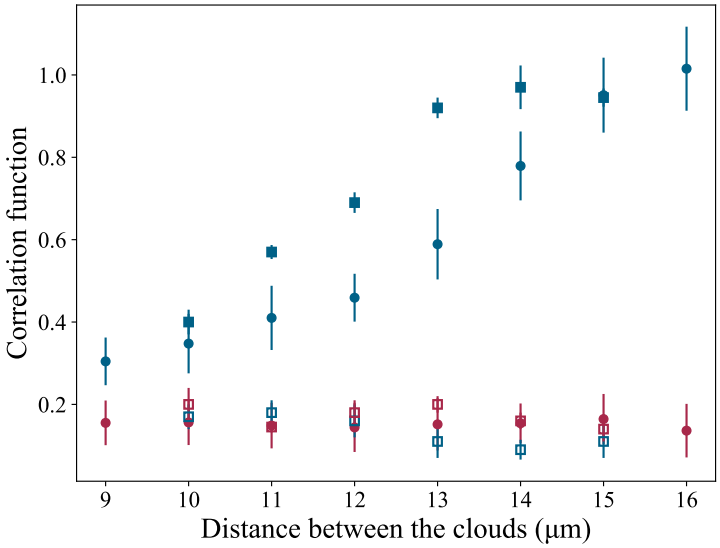

Figure 5.15.: Cross-correlation function $g^{(2)}_{AB}$ (blue squares) and each one of the clouds individually (blue and red squares) measured in the experiment at a fixed $|80S_{1/2}\rangle$ Rydberg state for different clouds separations. The result from the model for the cross (blue circles) and single (red circles) correlation function corresponds to Rydberg blockade radius of 14.63 µm for level $|80S_{1/2}\rangle$, a cloud longitudinal size of 27 µm and a radial size of 3 µm.

In figure 5.15 the combined calculated results for a fixed interaction strength and different clouds separation are shown. As previously observed in figures 5.11 and 5.12, a bigger blockade radius of 14.6 µm is required in the theoretical model compared to the experimental value of approximately 10 µm. Despite the good reproduction of the experimental data points within a single cloud, there is a significant deviation form the experimental data in the two clouds case.

In conclusion, the idea of a hard sphere that represents a Rydberg

blockade was sufficient in reproducing the cross correlation function $g_{AB}^{(2)}$ measured in the experiment for different Rydberg states at fixed distance of 10 µm between the atomic clouds. However, it is apparent from the results shown in this section, that a hard sphere model is not a good solution when the Rydberg state is fixed and the separation is varied (figure 5.15). The experimentally obtained data can not be entirely covered by a hard sphere model. The interaction induced phase shifts caused by the van der Waals interactions can not be simply neglected and should be included in the theoretical explanation.

5.5. Dephasing simulation

The model referred to in this section was developed in collaboration with Paul Huillery based on the work published in [98], where a theory for interaction induced dephasing within one atomic ensemble has been explored. As mentioned previously, photons stored as collective excitations are sensitive to interaction induced phase shifts. Based only on the additional phase shift of the imprinted spin-wave pattern, due to the van der Waals interactions, it allows the successful reproduction of the obtained experimental data.

Single channel

Let us consider an atomic ensemble within a single channel. The number of photons that can be detected simultaneously in a Hanbury-Brown Twiss interferometer is limited to two in each cloud, which limits the number of excitations used to the same number. The superposition of these collective states with different numbers of stored photons (between 0 and 2) is then:

$$|\psi\rangle = c_0|\psi_0\rangle + c_1|\psi_1\rangle + c_2|\psi_2\rangle \tag{5.9}$$

where the coefficients c_n describe the distribution of the signal photons. The collective ground state is $|\psi_0\rangle$.

The state containing one collective Rydberg excitation is defined as:

$$|\psi_1\rangle = \frac{1}{\sqrt{\sum_j E(\vec{r}_j)^2}} \sum_j E(\vec{r}_j) e^{i\phi(\vec{r}_j)} |r_j\rangle \tag{5.10}$$

where E is the electric field amplitude of the signal mode and ϕ is the imprinted signal and control field phase. $\vec{r_j}$ is the position of atom j, and $|r_j\rangle$ is the state where atom j is in the Rydberg state while the other atoms are in the ground state.

The state containing two collective Rydberg excitations is given by:

$$|\Psi_2\rangle = \frac{1}{\sqrt{\sum_{j,k>j} (E(\vec{r}_j)E(\vec{r}_k))^2}} \sum_{j,k>j} E(\vec{r}_j) e^{i\phi(\vec{r}_j)} E(\vec{r}_k) e^{i\phi(\vec{r}_k)} |r_j, r_k\rangle \tag{5.11}$$

where $\vec{r_j}$ and $\vec{r_k}$ are the position of atom j and k and $|r_j, r_k\rangle$ is the state where atoms j and k are in the Rydberg state while the other atoms are in the ground state.

During the storage time t_{st}, the components of $|\psi_2\rangle$ experience an additional induced phase factor due to interactions between the two Rydberg excitations. This evolution can be expressed through the operator $\hat{U}(t_{st})$:

$$\hat{U}(t_{st}) = \sum_{j,k>j} e^{-iV_{jk}t_{st}/\hbar} |r_j, r_k\rangle\langle r_j, r_k| \tag{5.12}$$

where $V_{jk} = V_{VdW}(\vec{r}_j, \vec{r}_k) = C_6/|\vec{r}_j - \vec{r}_k|^6$ is the van der Waals potential.

The interaction-induced dephasing reduces the probability with which two photons are retrieved from the state $\hat{U}(t_{st})|\psi_2\rangle$, in the same spatial mode as the initial signal photons. The overlap $D^{(2)}$ between the initial collective ground state $|\psi_2\rangle$ and the collective ground state after a photon storage and retrieval cycle $\hat{U}(t_{st})|\psi_2\rangle$, which determines the probability to retrieve signal photons in the original spatial mode, should be calculated for two pairs of control and signal photons.

$$D^{(2)} = \langle\psi_2|\hat{U}(t_{st})|\psi_2\rangle = \frac{1}{\sum\limits_{j,k>j}(E_(\vec{r}_j)E(\vec{r}_k))^2} \sum_{j,k>j} (E(\vec{r}_j)E(\vec{r}_k))^2 e^{-iV_{jk}t_{st}/\hbar} \tag{5.13}$$

Overlap $D^{(2)} = 1$ means that there is no interaction induced dephasing. This overlap $D^{(2)}$ can be relayed to the second order single-correlation function in the experiment as:

$$g^{(2)} = \frac{2|D^{(2)}|^2|c_2|^2}{(|c_1|^2 + 2|D^{(2)}|^2|c_2|^2)^2} \tag{5.14}$$

where $|c_1|^2$ and $|c_2|^2$ are the probabilities to store one or two photons. A single stored photon is not affected by the interaction-induced dephasing and as a result the probability to retrieve two stored photons in the original signal mode is given by $|D^{(2)}|^2$.

The incoming signal pulse is a classical light and the number of incoming photons should follow a Poisson distribution. The decay of the Rydberg excitations is neglected as their lifetime is long compared to the storage times t_{st} used in the experiment.

To simulate the data for a single cloud we create a cigar-shaped ensemble of $N = 1000$ randomly positioned rubidium atoms with Gaussian distributions. The value of the axial width, previously concluded from the blockade model, has been changed to 22 µm, as this value seems to be in a better agreement using this theoretical model. In the next step $D^{(2)}$ is calculated for the given atomic positions and the interaction potential V_{jk}.

The obtained result and the coefficients c_n (for a specific initial photon number distribution) are used to calculate the single-correlation function $g^{(2)}$. This procedure is repeated for multiple randomly generated ensembles and the results are averaged to obtain the final $g^{(2)}$. A schematic of the model for two channels case is shown in figure 5.18.

This model does not include any free parameters, but some experimental parameters, such as the number of atoms and longitudinal size of the atomic cloud, are known only as a rough approximation. The number of excitations stored in each channel follows Poissonian statistics with a mean $\overline{n} = 0.01$. The low value of $\overline{n}$ ensures that the truncation to two excitations has negligible effects on the calculated quantities.

$$|c_n|^2 = \frac{1}{n!} e^{-\overline{n}} \overline{n}^n \tag{5.15}$$

The number of photons and the number of atoms can be varied to verify that they do not affect the results. $g^{(2)}$ shows no impact as long as the mean number of photons $\overline{n} \ll 1 \ll N$.

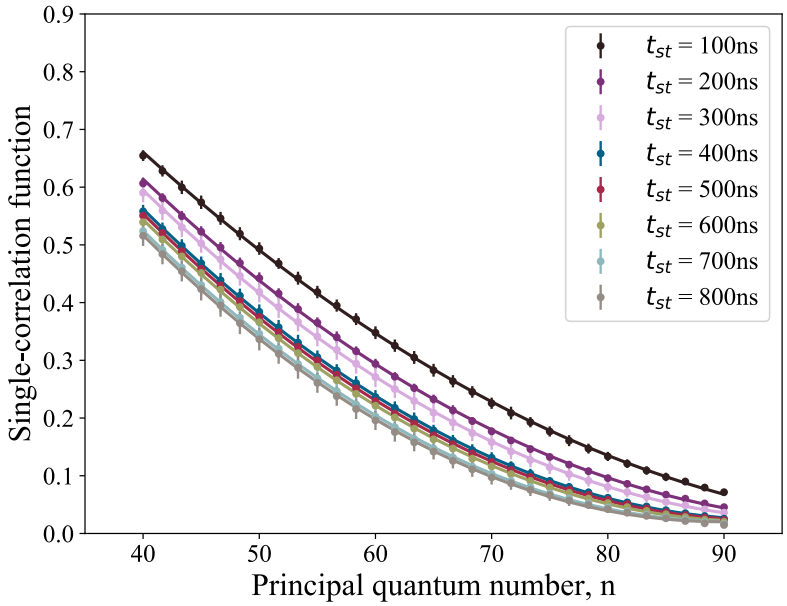

Figure 5.16.: Simulation results for single-correlation function $g_A^{(2)}$ at different storage times for different principal quantum numbers. The cloud has an axial size of 22 µm and a radial size of 3 µm. The lines are only drawn as a guidance.

The signal light mode is Gaussian with a waist of 1 µm, focused in the center of the channel.

As the interaction induced dephasing is storage time dependent, the influence on the photon retrieval while the storage time has been varied (between 100 ns and 800 ns) for different collective Rydberg states $|nS_{1/2}\rangle$ (between $n = 40$ and $n = 90$) has been investigated. It is clear in figure 5.16, that increasing either the principle quantum number n or the interaction time t_{st}, leads to an increase of the anti-correlation in the expected photon retrieval. The van der Waals potential scales with $V_{VdW} \propto n^{11}$ and also the interaction time dependence leads to a stronger suppression.

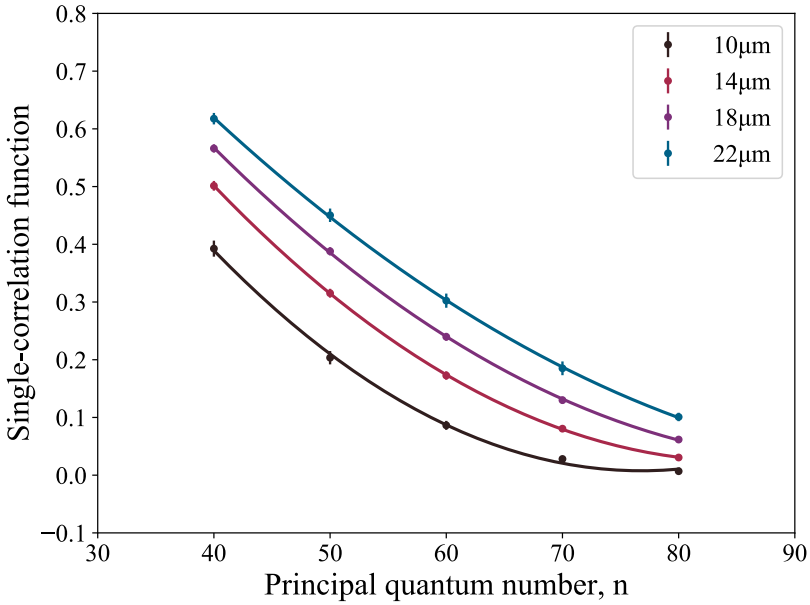

Figure 5.17.: Simulation results for single-correlation function $g_A^{(2)}$ for different for different collective Rydberg states $|nS_{1/2}\rangle$ with n from 40 to 80 and different axial cloud widths from 14 µm to 22 µm. The storage time used to gain this results is 170 ns, which is approximately the storage time used in the experiment. The cloud is with a constant radial size of 3 µm. The lines are only drawn as a guidance.

As in the blockade model, the dependence of anti-correlations in the photon retrieval on the axial length of the cloud has also been studied, as shown in figure figure 5.17. The axial length of the cloud has been varied (between 14 µm and 22 µm) for different collective Rydberg states $|nS_{1/2}\rangle$

(between $n = 40$ and $n = 80$). The theoretical anti-correlations in the photon retrieval become stronger as the medium becomes denser. This increase in the interaction-induced dephasing is due to the fact that the van der Waals interactions depend on the distance between the Rydberg excitations. As the length of the cloud is one of the unknown parameters, this result again can give us a clue to the approximate dimensions of the cloud in our experiment. The storage time used to obtain these results is equal to the storage time in the experiment $t_{st} = 170\,\text{ns}$.

Two channels

In the case of two channels, after between 0 and 2 photons are stored, the system will be in a state defined as:

$$|\psi^{(AB)}\rangle = c_{00}|\psi_{00}^{(AB)}\rangle + c_{10}|\psi_{10}^{(AB)}\rangle + c_{01}|\psi_{01}^{(AB)}\rangle + c_{11}|\psi_{11}^{(AB)}\rangle \tag{5.16}$$

with

$$|\psi_{nm}^{(AB)}\rangle = |\psi_{n}^{(A)}\rangle \otimes |\psi_{m}^{(B)}\rangle \tag{5.17}$$

where A and B refer to the two spatially separated channels. Similar to the single channel case, the coefficients c_{nm} describe the distribution of the signal photons. A schematic of the model is shown in figure 5.18.

During the storage time t_{st}, the components of $|\psi_{11}^{(AB)}\rangle$ experience an additional phase factor due to interactions between the two Rydberg excitations. This evolution can be expressed through the operator $\hat{U}^{(AB)}(t_{st})$:

$$\hat{U}^{(AB)}(t_{st}) = \sum_{j_A, j_B} e^{-iV_{j_A j_B} t_{st}/\hbar} |r_{j_A}\rangle\langle r_{j_A}| \otimes |r_{j_B}\rangle\langle r_{j_B}| \tag{5.18}$$

where $V_{j_A j_B} = V_{VdW}(\vec{r}_{j_A}, \vec{r}_{j_B}) = C_6/|\vec{r}_{j_A} - \vec{r}_{j_B}|^6$ is the van der Waals potential.

The interaction-induced dephasing reduces the probability to retrieve a photon from the state $\hat{U}^{(AB)}(t_{st})|\psi_{11}\rangle$ simultaneously in the signal photon mode from each channel.

To get to the second order cross-correlation function $g_{AB}^{(2)}$, the overlap between the ground state $|\psi_{11}^{(AB)}\rangle$ and the state resulting from the emission from $\hat{U}^{(AB)}(t_{st})|\psi_{11}^{(AB)}\rangle$ should be calculated for a pair of control and signal

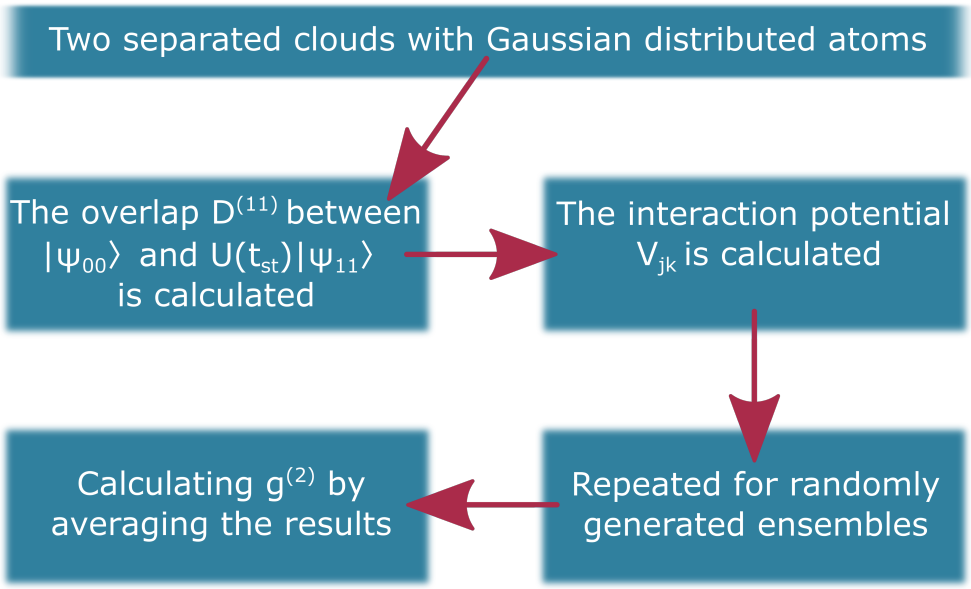

Figure 5.18.: A scheme of the dephasing model used to simulate the photon statistics gathered from the experiment.

photons.

$$D_{AB}^{(11)} = \langle \psi_{11}^{(AB)} | \hat{U}^{(AB)}(t_{st}) | \psi_{11}^{(AB)} \rangle = \\ = \frac{1}{\sum\limits_{j_A, j_B} (E_A(\vec{r}_{j_A}) E_B(\vec{r}_{j_B}))^2} \sum_{j_A, j_B} (E_A(\vec{r}_{j_A}) E_B(\vec{r}_{j_B}))^2 e^{-iV_{j_A j_B} t_{st}/\hbar} \tag{5.19}$$

This leads to $g_{AB}^{(2)}$ defined as:

$$g_{AB}^{(2)} = \frac{|D_{AB}^{(11)}|^2 |c_{11}|^2}{(|c_{10}|^2 + |D_{AB}^{(11)}|^2 |c_{11}|^2)(|c_{01}|^2 + |D_{AB}^{(11)}|^2 |c_{11}|^2)} \tag{5.20}$$

where $|c_{01}|^2$, $|c_{10}|^2$ and $|c_{11}|^2$ are the probabilities to store one photon in A, one photon in B or one photon in each simultaneously. A single stored photon is not affected by the interaction-induced dephasing and as a result the probability to retrieve two stored photons in the original signal mode is again given only by $|D_{AB}^{(11)}|^2$.

To simulate two clouds, two cigar-shaped ensembles of $N = 1000$ randomly positioned rubidium atoms with a Gaussian distribution based on experimentally determined cloud parameters have been created. Their centers are separated by a distance d_{AB}. The signal photon modes of both

channels are Gaussian with a waist of 1 µm, parallel to each other and focused in the centers of the clouds. The number of excitations stored in each channel follow a Poissonian statistics with a mean $\overline{n}, \overline{m} = 0.01$. Again this value has no effect on the results as long as $\overline{n}, \overline{m} \ll 1 \ll N_A, N_B$.

In the next step $D_{AB}^{(11)}$ is calculated for the given atoms positions and the interaction potential $V_{j_A j_B}$. The obtained result and the coefficients c_{mn}, given by:

$$|c_{nm}|^2 = |c_n|^2 |c_m|^2 \tag{5.21}$$

for a specific initial photon number distribution, are used to calculate the cross-correlation function $g^{(2)}$. This procedure is repeated for multiple random generated ensembles and at the end the results are averaged to obtain the final $g^{(2)}$.

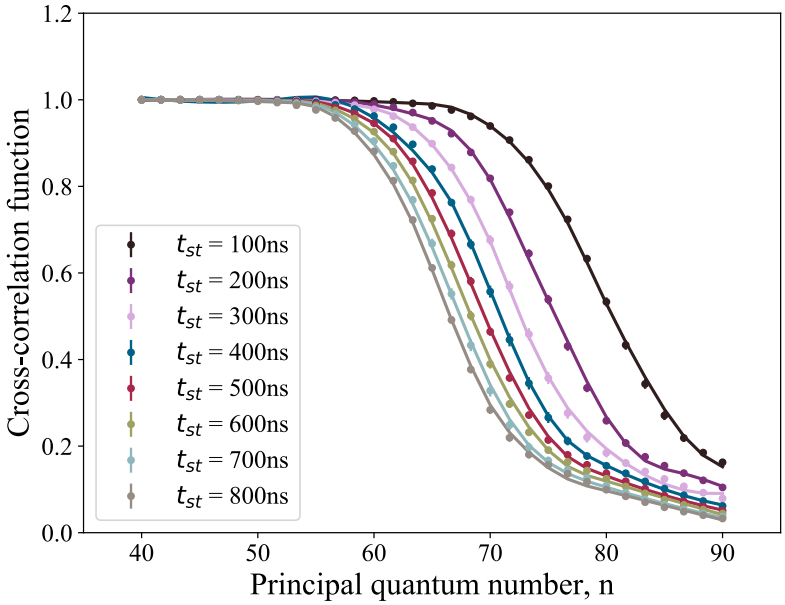

Figure 5.19.: Simulation results for cross-correlation function $g_{AB}^{(2)}$ at 10 µm clouds separation for different storage times and different principal quantum numbers. The cloud is with axial size of 22 µm and a radial size of 3 µm. The lines are only drawn as a guidance.

Figure 5.19 shows simulation results for $g_{AB}^{(2)}$ for different storage times (between 100 ns and 800 ns) as the principal quantum number n is varied (between 40 and 90). As expected the anti-correlation in the photon

retrieval increases with n as the van der Waals potential in principal scales with $V_{VdW} \propto n^{11}$. Additional phase shifts depend also on the storage time, and as a result, increasing the interaction times will lead to a stronger suppression of photons retrieved from both channels simultaneously.

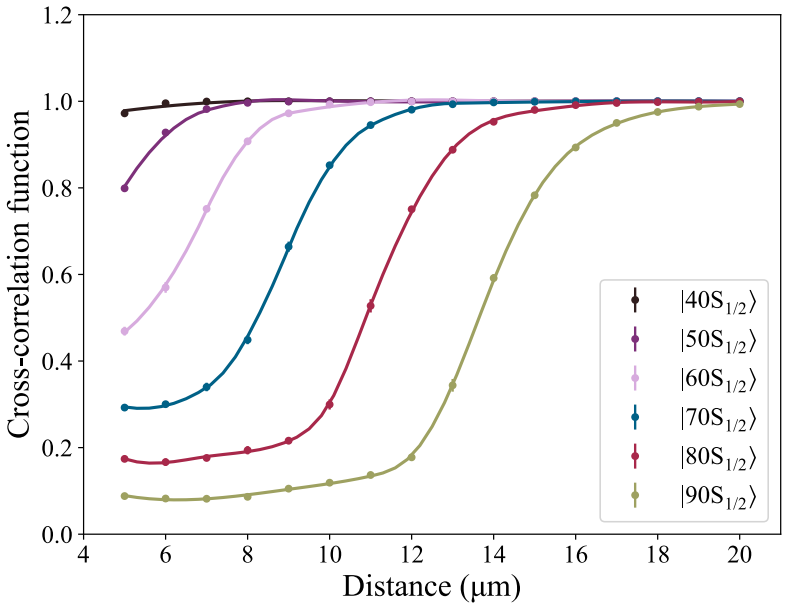

Figure 5.20.: Simulation results for cross-correlation function $g^{(2)}_{AB}$ at different clouds separation for different collective Rydberg states $|nS_{1/2}\rangle$ with n from 40 to 90. The storage time used to gain this results is 170 ns which is approximately the storage time used in the experiment. The cloud is with axial size of 22 µm and a radial size of 3 µm. The lines are only drawn as a guidance.

The van der Waals potential is distance dependent and in case of two channels the cloud separation defines the distance between the Rydberg excitations. Figure 5.20 shows simulation results for $g^{(2)}_{AB}$ for different clouds separations (between 5 µm and 20 µm) as the Rydberg state $|nS1/2\rangle$ is varied (between $|40S_{1/2}\rangle$ and $|90S_{1/2}\rangle$). The interaction time is $t_{st} = 170$ ns. The anti-correlation in the photon retrieval increases with n due to the van der Waals potential scales with $V_{VdW} \propto n^{11}$. Because it is also distance dependent, that leads to a suppression of photons retrieval from both channels simultaneously as the distance descends.

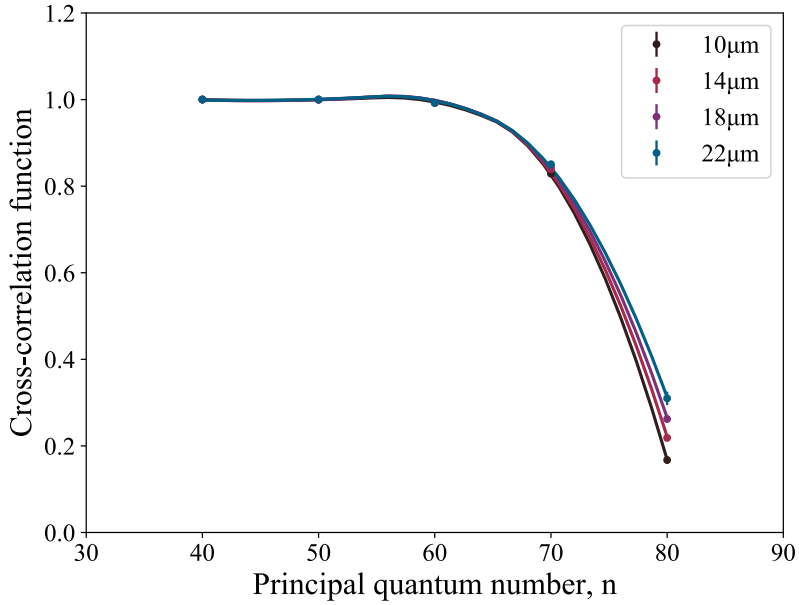

Figure 5.21.: Simulation results for cross-correlation function $g^{(2)}_{AB}$ at clouds separation of 10 µm for different collective Rydberg states $|nS_{1/2}\rangle$, with n from 40 to 80, and different axial cloud lengths, from 14 µm to 22 µm. The storage time used to gain this results is 170 ns, which is approximately the storage time used in the experiment. The cloud is with a constant radial size of 3 µm. The lines are only drawn as a guidance.

As mentioned previously one of the uncertain parameters in the dephasing model is the cloud longitudinal size. Unlike the single channel case, where both excitations are within a single cloud and the separation between them depends on the cloud size, for the two channels case (shown in figure 5.21) both excitations are expected to be symmetrically centered in each of the clouds. For a fixed cloud separation the cloud size should not have a significant effect. As expected, there is no obvious suppression in the photon retrieval from both channels simultaneously. The two channels case can not be used as an estimation of the effective cloud size in the experiment.

Comparing the experimental single and cross-correlation functions $g^{(2)}$ with the simulation results in figure 5.22, we find that they are in good agreement. The additional dephasing effect appears earlier in the case of

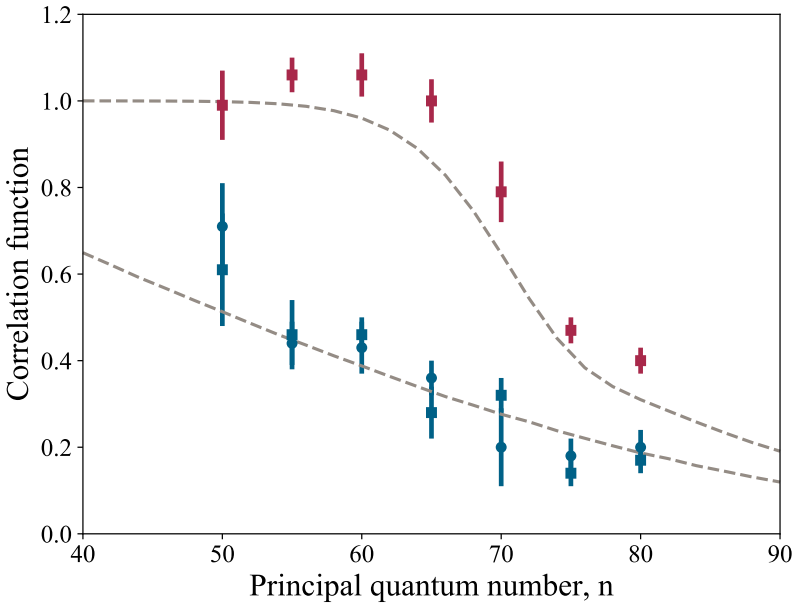

Figure 5.22.: The effect of the interaction strength over the retrieved photon statistics. The cross-correlation function $g^{(2)}_{AB}$ measured for photons retrieved from storage in Rydberg state $|nS_{1/2}\rangle$ (red squares). The channel separation is 10 µm. The measured single-correlation functions $g^{(2)}_{A/B}$ is represented by the blue squares and circles (for each one of the two channels) and shows signs of earlier suppression. The dashed grey lines represent results of the dephasing model.

a single channel, as the distance between the excitation within the cloud is not restricted. For the two channels case it is fixed at 10 µm and the interaction potential will start suppressing the simultaneous retrieval after gaining some particular strength. The interactions lead to a suppression of $g^{(2)}_{AB}$ after $n = 60$.

Figure 5.23 shows experimental and numerical results for the single and cross-correlation function $g^{(2)}$ at different separations with collective Rydberg state $|nS_{1/2}\rangle = |80S_{1/2}\rangle$. As expected, the measured and numerically calculated single-correlation functions $g^{(2)}_{A/B}$ in absence of the second channel remain approximately constant. For the two channel case the suppression stays even beyond the range of the excitation blockade, $r_b \approx 10$ µm for $|80S_{1/2}\rangle$. With the descending of the separation distance the

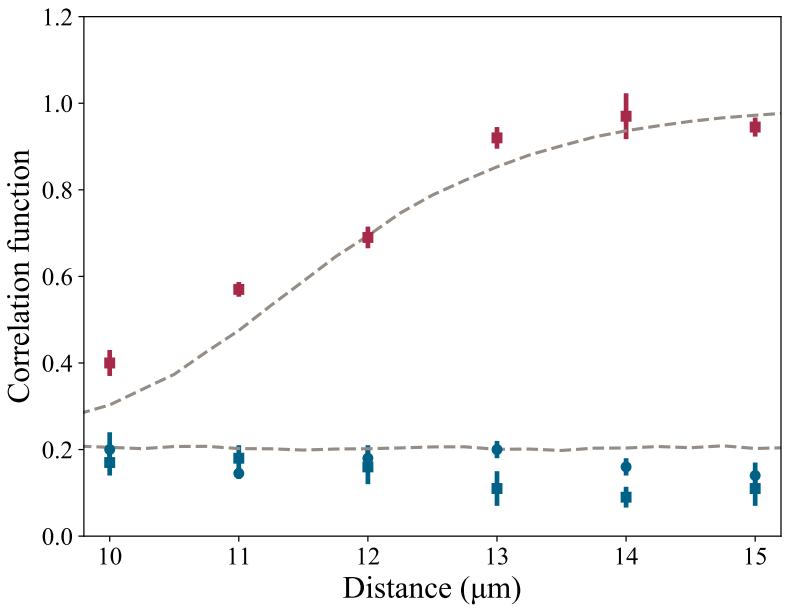

Figure 5.23.: The effect of the clouds separation on retrieved photon statistics. The single $g^{(2)}_{A/B}$ (blue circles and squares) and cross-correlation function $g^{(2)}_{AB}$ (red squares) at different separations with collective Rydberg state $|nS_{1/2}\rangle = |80S_{1/2}\rangle$. The dashed grey lines represent results of the dephasing model.

cross-correlation function $g^{(2)}_{AB}$ starts to approach the results of the single correlation function $g^{(2)}_{A/B}$. This result is also expected, as the $g^{(2)}$ functions of both cases should become equal at distances similar to the corresponding blockade radius. The simulation results are in good agreement with the experimentally gathered data.

The advantage of using the imprinted phase model before the dipole blockade mechanism model to interpret the experimental photon statistics is mostly visible when varying the storage time. In the case of a dipole blockade, there should be no time dependence (the time dependence is not included in the blockade model). The experimental results for two different Rydberg states, while the separation distance is constant, show clear dependence on the storage time. These results are shown in figure 5.24 for Rydberg state $|70S_{1/2}\rangle$ and separation distance, $d = 11.5\,\mu\text{m}$ (blue circles), and for Rydberg state $|80S_{1/2}\rangle$ and separation distance, $d = 11\,\mu\text{m}$ (red circles). The lower Rydberg state shows a weaker time dependence in

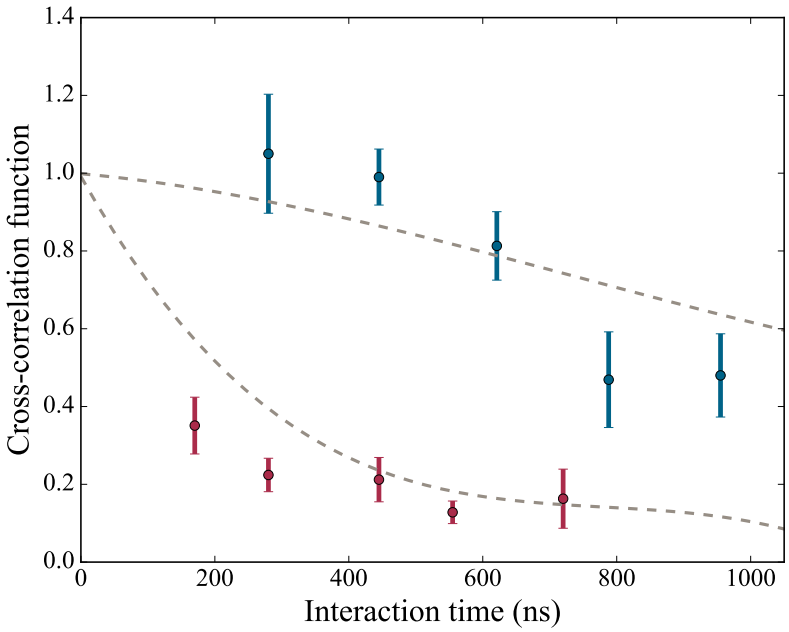

Figure 5.24.: The effect of the interaction time on retrieved photon statistics. The cross correlation function $g^{(2)}_{AB}$ at different storage times t_{st} with collective Rydberg state $|nS_{1/2}\rangle = |70S_{1/2}\rangle$ (blue circles) and separation of $d = 11.5\,\mu\text{m}$, and collective Rydberg state $|nS_{1/2}\rangle = |80S_{1/2}\rangle$ (red circles) and separation of $d = 11\,\mu\text{m}$. The dashed grey lines represent results of the dephasing model.

agreement with the model. The uncertainties in the experimental data are due to the strong dependence between the photon storage and retrieval efficiency and the storage time.

This result shows again that the interaction-induced phase shifts are the main contribution to the behaviour observed in the experiment and cannot be neglected and substituted by a hard blockade sphere model.

For better understanding of the dephasing mechanism, the phase pattern as a result of interaction phase shifts, and the perturbations in the original signal modes, have also been calculated for different scenarios. The amplitude and direction of the emitted light by the first cloud in presence of a stored excitation in the second one is defined by the laser phase and Rabi frequency at each atom's position and the accumulated interaction phase for some defined storage time.

The evolution of the imprinted spin-wave phase in the presence of a

second cloud, represented as a single Rydberg $|80S_{1/2}\rangle$ excitation (10 µm away) is shown in figure 5.25. The different interaction times show how the additional phase modifies the original mode pattern over time. Due to the van der Waals interaction and its time dependence, the results show bending of the original stored pattern. This should lead to an emission spatially different from the original signal photon mode.

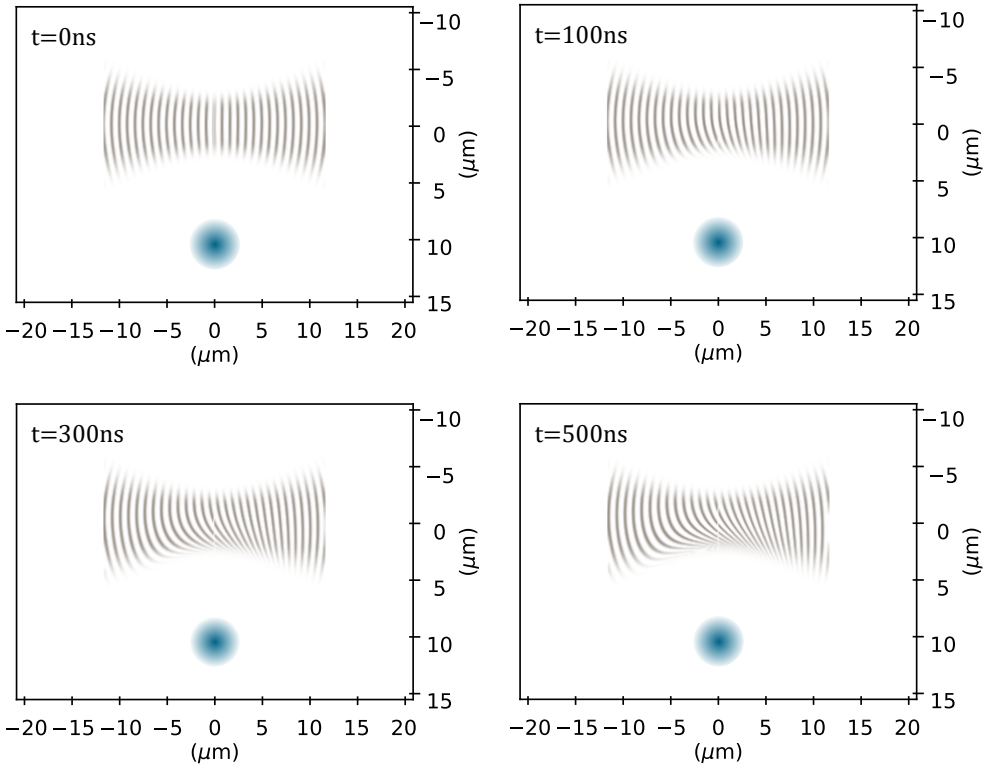

Figure 5.25.: The evolution of the imprinted spin-wave phase pattern during storage. The second cloud is represented as a Rydberg excitation at $|80S_{1/2}\rangle$ and it is 10 µm away. The different interaction times show the additional phase perturbation due to the van der Waals interaction. The cloud's radial size is 3 µm and 22 µm longitudinal size.

The emitted photon modes, as a result from the modified spin-wave pattern, are shown in figure 5.26. The additional angle and the fact that the cloud is longitudinally bigger than a blockade radius should result in a suppression of the simultaneously detected retrieved photons in the original signal mode from both channels. The phase pattern becomes increasingly distorted with longer storage times due to the additional van der Waals

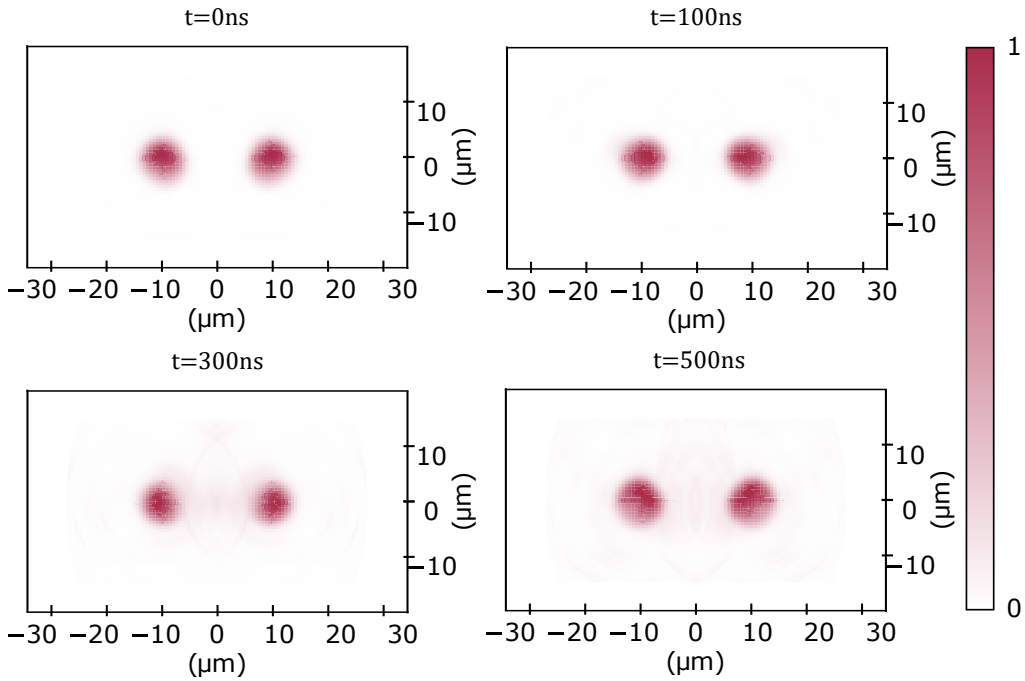

Figure 5.26.: The emitted phase pattern of the stored photons at $|80S_{1/2}\rangle$ and separation of 10 µm. The cloud's radial width is 3 µm and the axial is 22 µm.

dephasing and gets more difficult for detection with a single mode fiber. The colorbar represents normalised peak intensity.

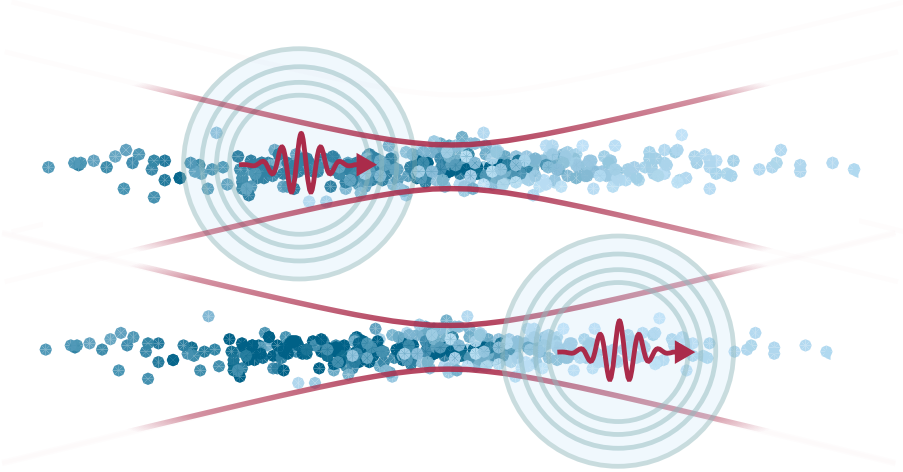

Figure 5.27.: A schematic of the Rydberg dephasing regime. The experimental cigar-shaped clouds dimensions allow the single excitation position to not be localized in the cloud.

As discussed previously, the van der Waals interaction is also distance dependent and as a result the position of the nearby Rydberg excitation is important. The experimental cigar-shaped clouds' dimensions allow the single excitation position not to be localized in each cloud's center, as shown schematically in figure 5.27.

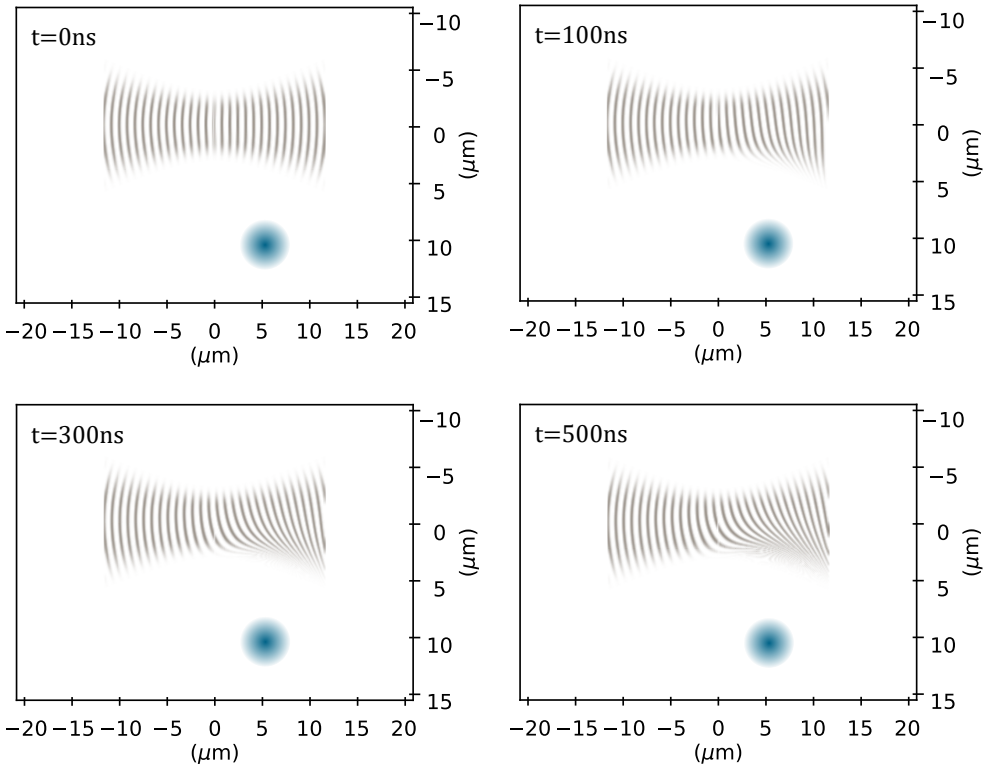

Figure 5.28.: The evolution of the imprinted spin-wave phase pattern during storage. The second cloud is represented as a Rydberg excitation at $|80S_{1/2}\rangle$ and it is 10 µm away and shifted in axial direction with 5 µm from the center. The different interaction times show the additional phase perturbation due to the van der Waals interaction and how this axial shift affect just partially the spin-wave stored pattern. The cloud's radial size is 3 µm and 22 µm longitudinal size.

The evolution of the imprinted spin-wave phase in the presence of a second cloud, represented as a single Rydberg $|80S_{1/2}\rangle$ excitation (10 µm away), shifted from the center of the cloud, is shown in figure 5.28. The different interaction times show how the additional phase modifies the original mode pattern over time. Due to the van der Waals interaction, and its

time and distance dependence, the results show only partial bending of the original stored pattern. This should lead to an emission not only spatially different from the original signal mode, but with a blurred Gaussian profile due to the fact that only some of the atoms' phase will be modified.

The evolution of the imprinted spin-wave phase pattern, when the Rydberg excitations are not localised in the center of each cloud, starts showing significant perturbations at storage times longer than the experimentally used one of 170 ns. This leads to the conclusion that the experimentally observed suppression in the simultaneous photon retrieval should not be affected by the Rydberg excitation position within the cloud.

The dephasing model seems to be a more accurate and flexible solution to interpret the experimental results. The theoretical model for two channels shows less sensitivity to the only unknown parameter - the longitudinal cloud size. Additionally, it allows only the effective size of the cloud to be used in the radial direction as this represents the experimental conditions more accurately.

5.6. Summary

This chapter has introduced two different models to interpret experimental results gathered from two spatially separated atomic mediums. It has shown that the idea of a hard sphere model is not a sufficiently accurate solution and the additional van der Waals interactions dephasing can not be simply neglected when explaining contactless interactions between photons stored as collective Rydberg excitations in spatially separate mediums. The dephasing model seems a better more flexible solution and is in a better agreement with the Rydberg excitation interactions. Additionally, it allows only the effective size of the cloud, instead of all atoms in the dipole trap, to be used.

The demonstration of contactless effective photon interactions unlocks the potential for future improvements of the experimental setup which will allow the experiment to reach a single excitation regime. The van der Waals interactions between the collective excitations lead to spatial phase shifts which will be interesting to investigate both theoretically and experimentally. The first step to achieve that is to improve the longitudinal confinement of the microscopic atomic clouds. This whole topic will be discussed in the Chapter 6.

6. Towards single Rydberg excitation

6.1. Introduction

Optical nonlinearities allow for the realisation of strong effective photon photon interactions. The best way to make individual photons interact is to convert one photon into an atomic excitation. Unfortunately, this process is not so easy to control. When a photon is absorbed it will be scattered spontaneously in a random direction and the response of the medium to a second photon will be different (as shown in figure 6.1a). At the same time, a single atom does not strongly influence the propagation of a second photon. It is also hard to get good coupling between the photon and the emitter. A single atom could be strongly coupled to a single photon in a well-controlled environment using a cavity (figure 6.1b), providing a response on the single photon level [16–18]. The probability to absorb a photon can be improved by using an atomic ensemble instead of

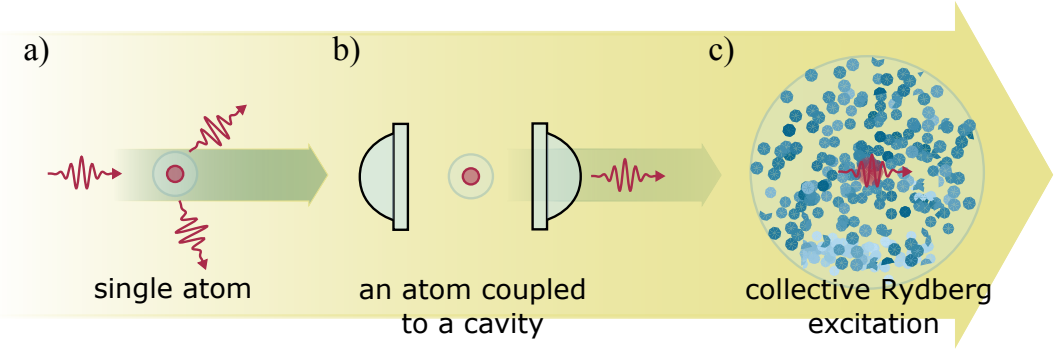

Figure 6.1.: Different configurations for effective photon photon interactions. a) A single atom as an emitter, b) a single atom strongly coupled to a single photon in a well-controlled environment using a cavity and c) a single collective Rydberg excitation.

a single atom. On the other hand, a single collective Rydberg excitation could change the optical response of a whole ensemble of atoms (figure 6.1c). This provides a large optical nonlinearity at the single photon level and therefore a potential to realize fully deterministic protocols for manipulating photons.

This chapter covers the steps that have been performed to improve the longitudinal confinement of the microscopic atomic clouds in the experiment. A stronger confinement should allow for the exploration of a regime in which both microscopic atomic clouds can be fully blockaded by a single stored photon (figure 6.2). The presence of one photon in either of the mediums restricts the storage of a second photon. This regime has a direct technical applications in quantum optical devices such as switches [99], transistors [52, 53], or phase shifters [100]. The optical response of the blockaded volume is discrete in the presence or absence of a single stored photon.

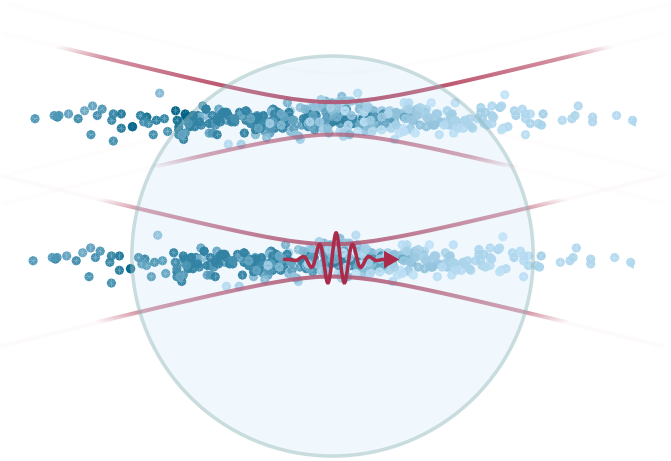

Figure 6.2.: Fully blockaded regime. For a channel separations $r < r_b$, simultaneous storage of photons as collective Rydberg excitations in both channels is forbidden.

On the other hand, it allows for the investigation of effective photon-photon interactions in spatially separated mediums, in a regime where each microscopic atomic cloud can contain a single photon at the same time - figure 6.3. The atoms in the collective Rydberg excitation experience additional interaction-induced dephasing which disturb the spatial mode of the emitted photons.

A solution to achieve the longitudinal confinement of the microscopic

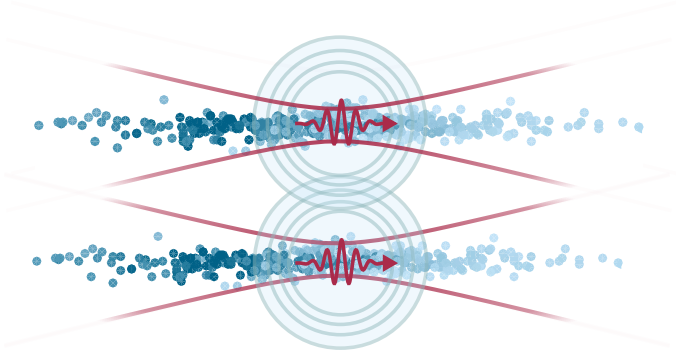

Figure 6.3.: Effective photon-photon interactions regime. For a channel separations $r > r_b$.

atomic clouds was the implementation of a crossed optical dipole trap [101]. As a result the optical depth of the microscopic atomic clouds should also improve.

The investigated suppression in the detection of simultaneously retrieved photons, from both channels, covers only the overlap between the retrieved and the original signal mode. It will be interesting in the future to also map out the emission pattern after the van der Waals dephasing.

6.2. Experimental improvements

Two-channel setup

In this work, the whole two-channel setup before the chamber has been rebuilt to allow independent control of the trapping beams. The in-house 910 nm laser has been switched with a 862 nm Toptica TA-PRO laser with 3.5 W output power. This allows for enough power to split between the tweezers and the new additional crossed trap.

The new pre-chamber setup is shown in figure 6.4. An additional pre-chamber waist measuring system (shown as Reference in 6.4) allows to conduct signal light and trapping light waist measurements, providing information for the waist sizes inside the science chamber. The signal beams are overlapped with the trap light on dichroic mirrors. Later, they are combined on a non-polarising BS. The separation between the channels can be adjusted by changing the incident angle on the first in-vacuum lens by rotating the non-polarising beam splitter (BS). The trap light waist radius and position are controlled using an adjustable telescope right after the trapping light fiber. The lens focuses the signal and trap beams to $1/e^2$-waists of $1.4 \pm 0.1\,\mu m$ and $4.6 \pm 0.4\,\mu m$ respectively.

As mentioned previously the limitations on the quality of the emitted mode is set by the geometry of the atomic cloud which depends entirely on the trapping geometry [101] that confine the atoms. The potential of the dipole force is given by:

$$U_{\text{trap}} = -\frac{1}{2}\langle \text{Re}(d).E \rangle \tag{6.1}$$

where d is the transition dipole moment and E is the electric field amplitude.

For a focused Gaussian laser beam, the potential is described by:

$$U(r,z) = U_0 \frac{\omega_0^2}{\omega^2(z)} e^{-(2r^2/\omega^2(z))}, \tag{6.2}$$

where ω_0 is the $1/e^2$ waist radius, r and z are the radial and axial coordinates and $\omega(z)$ is the $1/e^2$ radius of the beam at a distance z:

$$\omega(z) = \omega_0 \sqrt{1 + \left(\frac{z}{z_R}\right)^2} \tag{6.3}$$

with $z_R = \pi\omega_0^2/\lambda$ the Rayleigh range.

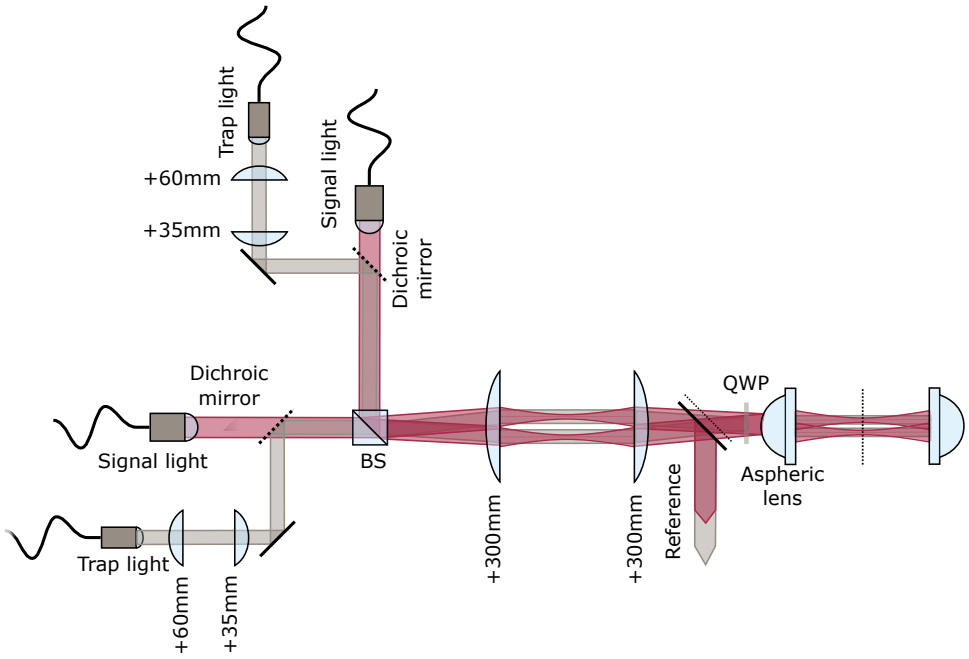

Figure 6.4.: Optical setup for two photonic channels. The signal beams are overlapped with the trap light on dichroic mirrors. Later, they are combined on a non-polarising BS. The separation between the channels can be adjusted by changing the incident angle on the first in-vacuum lens. The lens focuses the signal and trap beams to $1/e^2$-waists of $1.4 \pm 0.1\,\mu\text{m}$ and $4.6 \pm 0.4\,\mu\text{m}$ respectively.

The radial and axial size of a thermal cloud at temperature T in a harmonic potential is given by [101]:

$$\sigma_{\text{radial}} = \sqrt{\frac{k_B T \omega_0^2}{4U_0}} \tag{6.4}$$

and

$$\sigma_{\text{axial}} = \sqrt{\frac{k_B T z_R^2}{2U_0}}. \tag{6.5}$$

The previous experimental setup was based on two 910 nm optical tweezers focused to a waist of $4.5\,\mu\text{m} \pm 0.3\,\mu\text{m}$. This results in a high trapping frequency in the radial direction but poor confinement in the axial direction. The tightly focused traps result in cigar-shaped clouds with a large aspect ratio. The length can be compressed by narrowing the waist, but a reduction in the waist will result in small radial size of the atomic ensemble since both directions are dependent on the waist w_0.

The tight confinement in the propagation direction makes overlapping of the signal light and the tweezers extremely difficult. Wider traps would make this alignment less sensitive. The first implementation of a crossed dipole trap was at 1064 nm. This trap requires power ≈ 10 W due to the lower polarisability of rubidium atoms at this specific wavelength. The specific acousto-optic modulator's requirements, of fast switching (in the order of hundreds of nanoseconds) and at the same time maintaining such high power, led to the need for substituting the laser with a 862 nm laser. An 862 nm dipole trap has the advantage of a higher polarizabilty of the rubidium atoms at this wavelength.

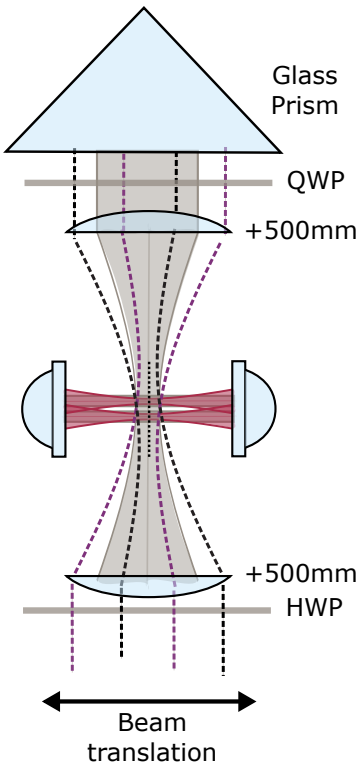

Figure 6.5.: A schematic of the setup of the crossed dipole trap. The two inch 500 mm lenses focus the crossed trap beams in the centre of the chamber to a waist of $27\,\mu\text{m} \pm 1\,\mu\text{m}$. The crossed trap beams are overlapped with the two-channel tweezers. Translation of the incoming beam can be used to change the crossing angle of the incoming and retro reflected trap beams in order to improve the confinement of the atoms in the axial direction.

The crossed trap setup geometry is shown in figure 6.5. Two 500 mm achromatic two-inch lenses were chosen to focus the crossed trap beam in the centre of the chamber to a waist of 27 µm ± 1 µm. The beam waist was measured in free space before setting the alignment into the science chamber. A further reduction of the trapping volume can be achieved by using the retro reflected dipole trap beam. The incoming and counter propagating trapping beams cross inside the chamber. This gives relatively low trapping frequencies in the propagation direction. As a result, the atoms should be more tightly confined in the crossing region.

The crossed trap is aligned to overlap with the tightly focused tweezers and should result in a higher density of atoms in these regions (as shown in figure 6.8). The new geometry allows for more efficient loading of the optical tweezers as well as providing the desired confinement, estimated by using the single-correlation function within a photonic channel.

To be able to implement the crossed trap, a fluorescence imaging setup has been used. The ratio of the trapping beam powers and the alignment were optimised by detecting the absorption signal using the single-photon counters.

The imaging of microscopic ensembles requires a high optical resolution which makes the process very difficult to accomplish. The chamber setup allows optical access to the dipole traps only along the radial axis through the in-vacuum lenses. The schematic of the fluorescence imaging setup is shown in figure 6.6.

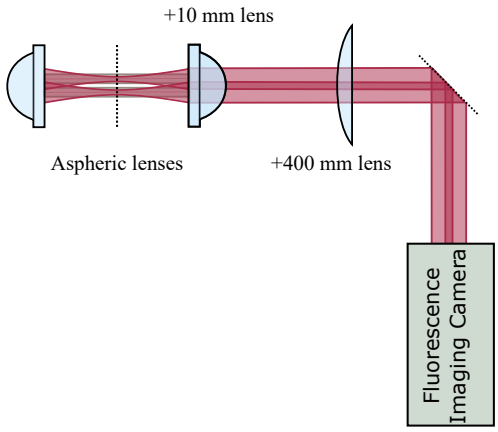

Figure 6.6.: Fluorescence imaging system. Fluorescence from the ensemble is imaged using x39 magnification telescope onto an electron-multiplied CCD Andor Ixon camera.

The small cloud sizes require μs exposure times to let the atoms expand before imaging. The fluorescence images taken are not focused and can not be an estimation for the size of the atomic ensembles or the temperature. To accurately calculate the number of atoms additional measurement and calibration should be performed in the future. Despite its disadvantages, the fluorescence imaging provides not real-time visualization of the dipole traps and can be used for alignment and initial overlapping of the tweezers and the crossed trap. The fluorescence images in figure 6.7, show the optical traps after a 100 µs exposure time.

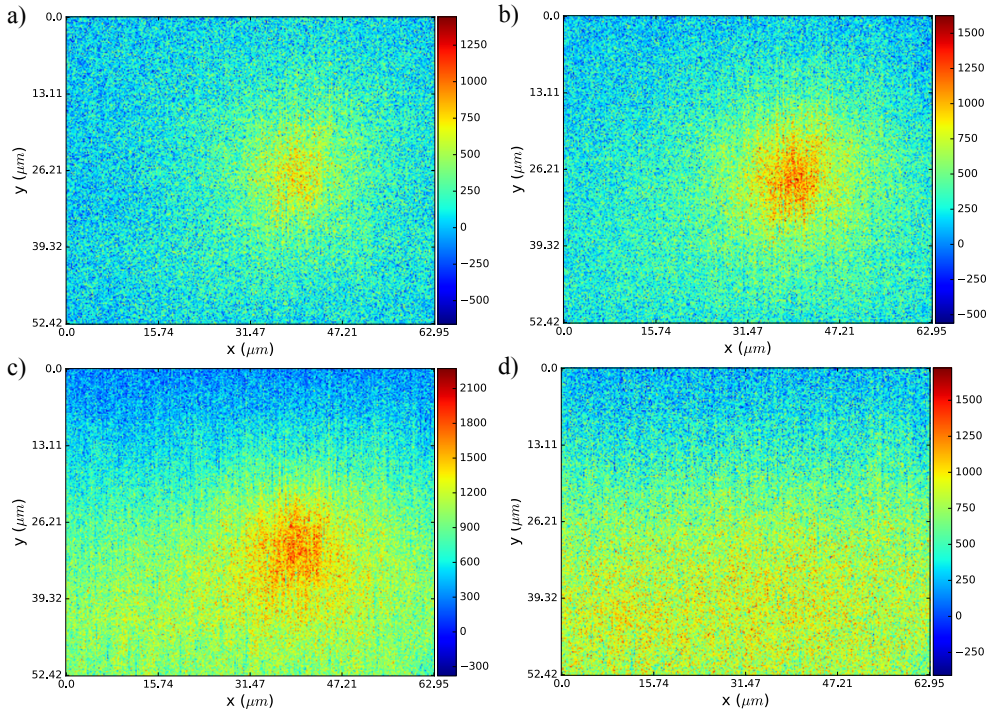

Figure 6.7.: Fluorescence imaging of the optical traps after a 100 µs exposure time. a) the ensemble created by the tweezer trap, b) the ensemble created by the tweezer trap and the crossed dipole trap, c) the ensemble created by the tweezer, the crossed dipole trap and its retro reflected beam, d) the ensemble created by the crossed dipole trap and its retro reflected beam.

From figures 6.7a and 6.7b, it is easy to see the improvement in the density of the microscopic ensemble created by the tweezer trap and the ensemble created by the tweezer and the crossed dipole trap. Adding the retro

reflected beam shows no significant improvement in the radial axis but also shows how the atoms spread among the crossed-retro reflected trap plane (figure 6.7c), probably due to bad alignment of the retro reflection. Figure 6.7d shows the ensemble created by the crossed dipole trap and its retro reflected beam. Each image is a combination of 400 individual images which makes it extremely time consuming and impossible to use for real-time alignment. However, the optimal method for real-time improvement of the overlap between the tweezers and the crossed trap, is the detected absorption signal on the single-photon counters. An absorption signal from the tweezer and the crossed trap after 25,000 repetitions is shown in figure 6.8. The calculated optical depth (OD) of the atomic medium confined by the tweezer trap is 5.15 ± 0.1 and 5.48 ± 0.1 for the atomic medium confined by the tweezer and crossed trap. For this measurement the crossed trap power is fixed at 734 mW.

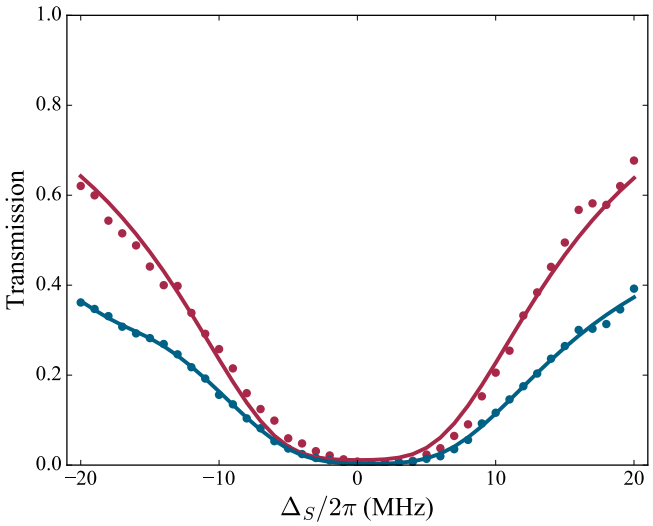

Figure 6.8.: An absorption signal from the tweezer trap (red) and overlapped with the crossed trap (blue). The calculated opticlal depth (OD) is 5.15 ± 0.1 and 5.48 ± 0.1 respectively. The crossed trap power is fixed at 734 mW.

Additionally, some steps have been taken towards balancing the power ratio between the crossed trap and the tweezers. Figure 6.9 gives some initial information about the ratio of the power needed in both traps. The crossed trap power is fixed at 600 mW.

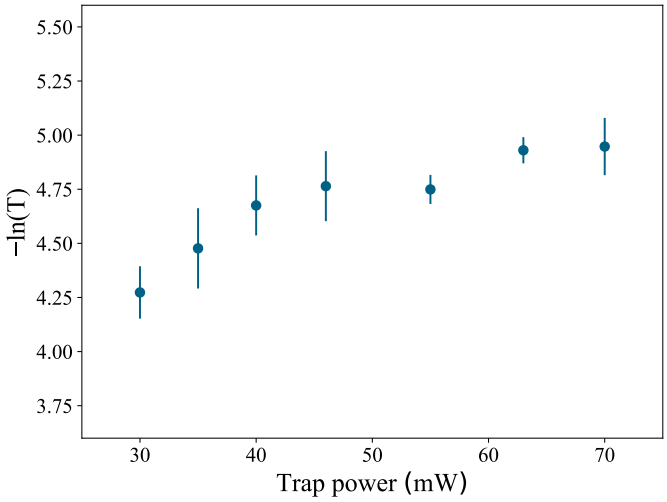

Figure 6.9.: Optical depth versus power in the tweezers. The crossed trap power is fixed at 600 mW.

6.3. Expected behaviour of the retrieved single photon pattern

The dephasing model discussed in chapter 5 can be used to predict a spin-wave stored pattern when the excitations are centered in the clouds and each cloud holds just a single Rydberg excitation.

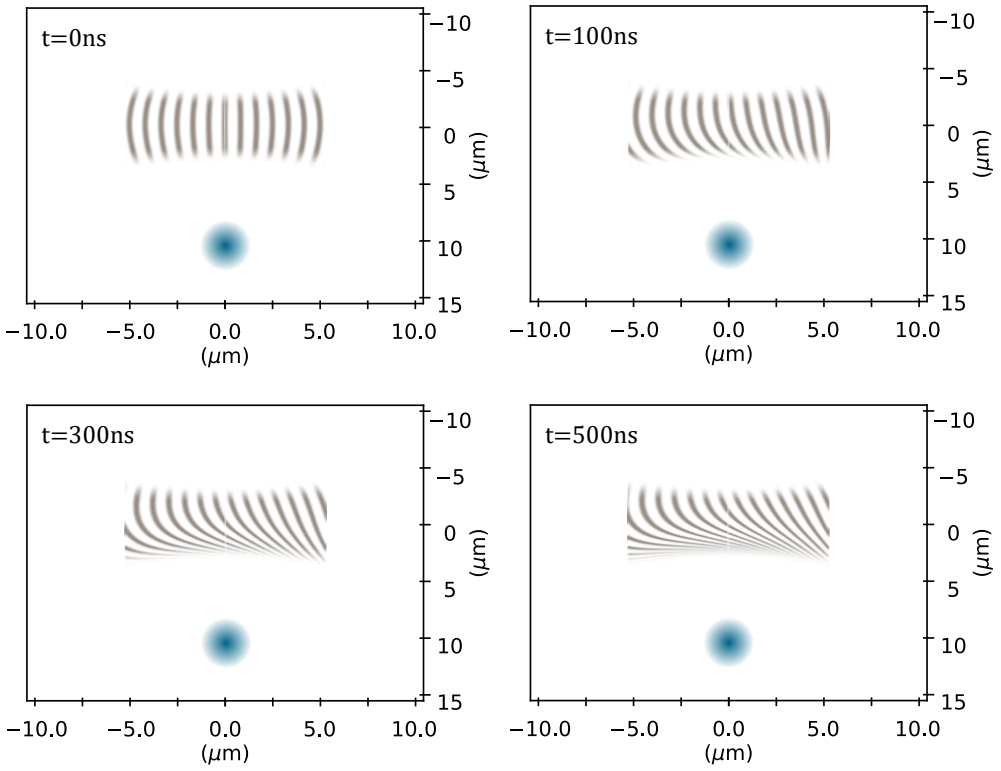

Figure 6.10.: Evolution of the imprinted spin-wave phase pattern during storage. The second cloud is represented as a Rydberg excitation (10 µm away from the center) at state $|80S_{1/2}\rangle$. The different interaction times show the additional phase perturbation due to the van der Waals interaction and how this axial shift just partially affects the spin-wave stored pattern. The cloud's radial size is 4 µm and the longitudinal size is 10 µm.

The evolution of the imprinted spin-wave phase pattern during storage is shown in figure 6.10. The second cloud is represented as a Rydberg excitation (10 µm away from the center) at state $|80S_{1/2}\rangle$. The different interaction times show the additional phase perturbation due to the van

der Waals interaction and how this axial shift just partially affects the spin-wave stored pattern. The cloud's radial size is 4 µm and the longitudinal size is 10 µm.

A projection of the expected photon pattern in xy (radial) plane for two different storage times (180 ns and 280 ns) is shown in figure 6.11. Atoms experience bigger dephasing with the increasing of the storage time and at the same time the Gaussian profile is spatially smeared. An additional peak looks to appear, probably due to the distance dependence of the van der Waals interactions. The colorbar represents the normalised peak intensity.

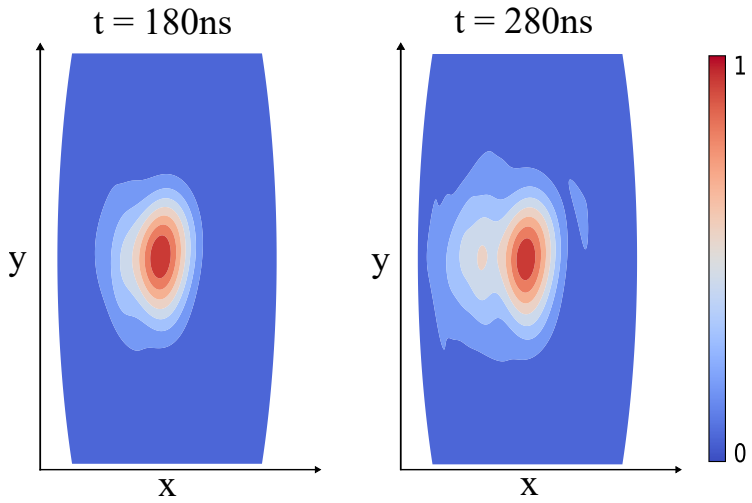

Figure 6.11.: Projections of the expected photon pattern in xy (radial) plane retrieved from an atomic cloud, spatially separated by 10 µm from a Rydberg excitation at state $|80S_{1/2}\rangle$, for two different storage times (180 ns and 280 ns). Atoms experience bigger dephasing with the increasing of the storage time and at the same time the Gaussian profile is spatially smeared.

A more in-depth investigation of the photon pattern could be made in the future. A prediction of the deflection angle of the mode distribution of emitted photons can also be made by fitting a Gaussian profile and calculating the separation between the two fits. This will provide some information where to look for the perturbed retrieved photons in the spatial domain. Figure 6.12 shows the deflection angle dependence of the interaction time.

In the future, it is intended to implement piezo-actuators to translate

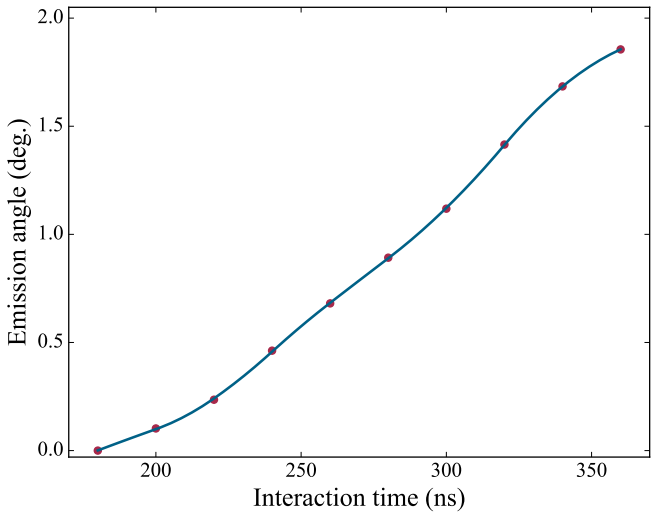

Figure 6.12.: Dependence of the deflection angle on the interaction time.

the single-mode fibre tip in the detection system. This will allow for the creation of a multi-pixel imaging array. Alternatively, an electron-multiplied CCD camera with very low read noise for direct spatial imaging can be used.

The model predicts that the collective mode remains relatively directional for small storage times but the Gaussian profile starts blurring significantly after $\approx 350\,\text{ns}$. The storage efficiency will also play a huge role in future experiments. The current storage efficiency is approximately 5%. The predicted displacement at 350 ns is approximately 0.6 µm, which makes it almost impossible to distinguish between the initial signal light profile and the retrieved collective mode pattern. A single correlation $g^2(0)$ has been taken at Rydberg state $|60S_{1/2}\rangle$ for two different dipole trap configurations. The calculated result for the second order correlation function in the presence of the cross trap is $g^2(0) = 0.35 \pm 0.09$. That shows a significant improvement compared to the previously obtained one of $g^2(0) = 0.43 \pm 0.07$.

In an absence of the cross trap, the correlation function $g^2(0) = 0.52 \pm 0.08$. This result is expected considering that the effective cloud size, defined by the probe waist radius and the Rayleigh range of the tweezer, is bigger in radial direction compared to the previously used setup.

These results show promise in reaching a regime of single photon excita-

tion at a Rydberg state of $|80S_{1/2}\rangle$ or higher.

6.4. Summary

Although a lot of experimental improvements have been implemented in order to enter the single photon regime, some unpredicted failures of the laser systems limited the progress in that direction. However, a single correlation $g^2(0)$ measurement has been taken at Rydberg state $|60S_{1/2}\rangle$. The obtained result of $g^2(0)$ shows significant improvement in comparison to those previously obtained. The single photon excitation regime can be probably reached at Rydberg state $|80S_{1/2}\rangle$ or higher. Unfortunately no measurements have been performed at that level in the new setup configuration, thus comparison with the previously obtained result of $g^2(0) = 0.17 \pm 0.03$ is impossible [31].

7. Conclusion and Outlook

This thesis includes an experimental and theoretical investigation of collective behavior in an ensemble of cold atoms. It presents system models to cover the effective long-range interactions between photons stored as collective excitations in separate and non-overlapping spatial modes. This work also reports on the initial implementation of an experimental setup dedicated to move quantum non-linear optics with cold Rydberg atoms towards a single photon regime.

In chapter 4, both the experimental and theoretical work regarding the collective behaviour of an ensemble of cold atoms is discussed. The provided investigation shows clear dependence between the optical depth and the decay rate of the directional emission, by varying different experimental parameters. It also shows that the superradiant emission is not intensity dependent and the system response on the single photon level is linear.

Theoretical models, describing the experimentally observed [56, 57] effective long-range interactions between photons stored as collective excitations in separate and non-overlapping spatial modes, have been introduced and discussed in chapter 5.

The experimental setup used for contactless effective photon interactions has been improved to open up opportunities for studying photon interactions on a single photon level. A longitudinal confinement of the microscopic atomic clouds [70, 101] has been demonstrated in chapter 6. The atom number in the clouds has also been increased. The confinement should unlock regimes where each of the ensembles can be fully blockaded by a single stored photon [26].

Although the results from the performed experiments are not explicitly conclusive, the improvement in the single correlation $g^2(0)$ function, measured at Rydberg state $|60S_{1/2}\rangle$, shows that there is a good possibility the desired regime can be achieved.

Outlook

In the future, Rydberg character could be introduced to the collective flash, discussed in chapter 4, which should result in decay rates proportional to the Rabi frequency of the dressing field and proportional to the lifetime of the used Rydberg state. The Rydberg character should also limit the possible simultaneous photon events inside the atomic medium and as a result a suppression in the single-correlation function $g^2(0)$ within the dressed flash should be observed. Numerical simulations and experimental data of a Rydberg dressed flash could provide a different approach in which to exploit collective mode engineering in quantum technology applications.

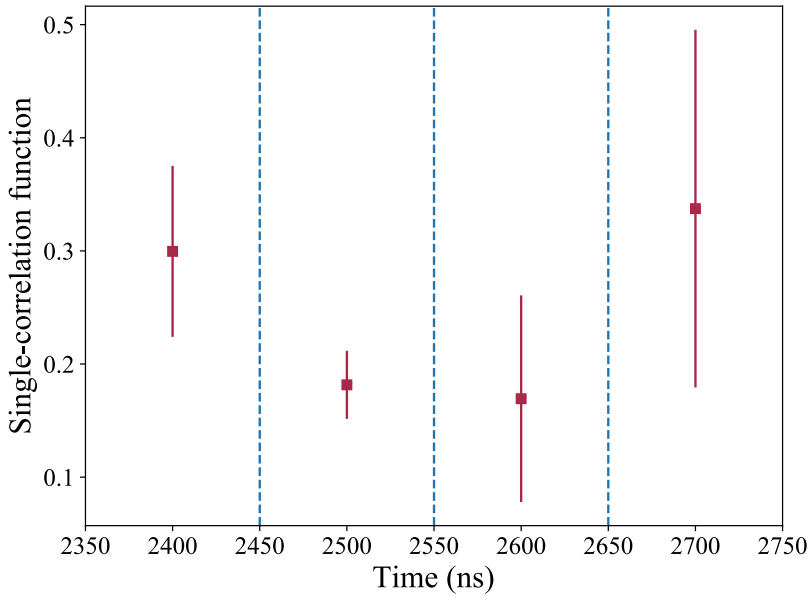

Figure 7.1.: A single-correlation function $g^{(2)}(t)$ within the retrieved photon pulse. Each one of the time bins is 100 ns long. The calculation is based on 350 million runs.

The photons distribution within the retrieved pulse has also been a subject of interest [67]. The great amount of data required for such investigation has always been a limitation. In figure 7.1 the calculated experimental single-correlation function $g^{(2)}(t)$ within the retrieved photon pulse is shown. The whole pulse is separated in four, 100 ns long bins.

The calculation is based on 350 million runs. It is clear by the size of the errorbar that the amount of data is insufficient.

Further investigation, for more accurate processing of the gathered photon statistics has been planned for the future. This will include the dead time of the single photon detectors.

Taking the experiment to a single photon regime will allow investigation of the indistinguishability of the experimental single photons. The coincidence counts should drop to zero for cases where the photons are absolutely identical and overlapped perfectly in time (also known as the Hong–Ou–Mandel dip) [102]. Two separate blue coupling lasers should address each one of the photonic channels, which allows independent control of the storage time t_{st}. It will be also interesting to observe how the induced interaction dephasing affects such indistinguishability.

Previous work of photon shaping (shown in figure 7.2) [57], using additional microwave (MW) field to couple the Rydberg state $|nS_{1/2}\rangle$ to a dark state $|nP\rangle$ for the coupling laser, can also benefit in a single photon regime.

Appropriate spatial and temporal modes are preferable for optimal performance of the single photons used in quantum communication or quantum cryptography. Similarly, in cavity QED quantum communication, single photons in the waveform of temporally symmetric pulses are used to minimize cavity-coupling losses. Furthermore, photons in rising exponential pulses (the photon mode should match spatially and temporally the time-reversed spontaneously emitted photon mode) are more efficient for quantum-state transfer between light and matter. Additionally, photons modes could be modified, for three level systems or for interacting molecules, depending on what the system dynamics requires. And finally, single Gaussian spatial modes are preferable for quantum information processes applications [103].

Controlling the spatial and temporal modes of a single photon has been observed in cavity experiments by a direct phase or an amplitude modulation [104–106]. Figure 7.2 shows photon retrieval shaping from Rydberg state $|80S_{1/2}\rangle$ for four different microwave Rabi frequencies $\Omega_{MW}/2\pi$ (0 MHz (a), 2.6 MHz (b), 8 MHz (c) and 16 MHz (d)) coupling Rydberg state $|80S_{1/2}\rangle$ to $|79P_{1/2}\rangle$ state. The photon retrieval model is based on a spontaneous emission from the intermediate state $|e\rangle$ to the ground state $|g\rangle$.

Using MW field allows to modify the spatial and temporal modes with almost no losses and it will be interesting to examine further in the single photon regime.

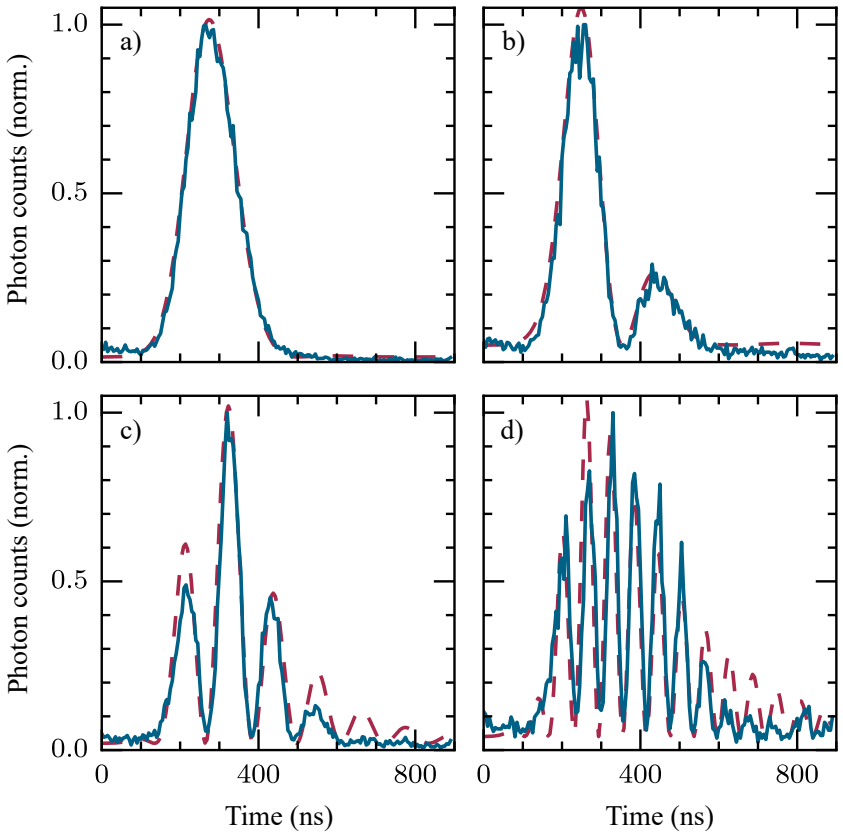

Figure 7.2.: Intensity modulation of optical photons at microwave frequency given by $\Omega_{MW}/2\pi$ for a) 0 MHz, b) 2.6 MHz, c) 8 MHz and d) 16 MHz. The dashed red line represents a photon retrieval model [57].

A. Modelling the superradiance behavior

The described system model is based on the work of Rob Bettles [107].

An ensemble of atoms is driven by a weak field E_l. Each atom is an oscillating electric dipole with particular frequency and decay rate Γ_0. The response $\mathbf{d}_j$ of the oscillating dipole j is a combination of both the driving laser field E_l as well as the scattered fields from every other dipole in the ensemble.

$$\dot{\mathbf{d}}_j = \left(\mathrm{i}\Delta - \frac{\Gamma_0}{2}\right)\mathbf{d}_j + \mathrm{i}\frac{|\mathcal{D}_0|^2}{\hbar}\Big(\mathsf{E}_\ell(r_j) + \sum_{\ell\neq j}\mathsf{G}_{j\ell}\mathbf{d}_\ell\Big) \tag{A.0.1}$$

where Δ is the detuning of the laser field from the atomic resonance frequency, Γ_0 is the spontaneous decay rate, $\mathcal{D}_0$ is the dipole matrix element, $\hbar$ is the reduced Planck constant, $\mathbf{r}_j$ is the position of dipole j, and $(\mathsf{G}_{j\ell}\mathbf{d}_\ell)$ is the scattered field at $\mathbf{r}_j$ from dipole $\mathbf{d}_\ell$.

The equation of motion for all the dipoles in the system can be solved numerically by taking a particular number of atoms and placing them into a configuration similar to the experimental one described in chapter 4. Gaussian distributed 400 atoms have been used to simulate the experimental data presented in chapter 4.

As well as looking at the dynamics of the dipoles, we can also look at the steady state. To do that, we can set the time derivative $\dot{\mathbf{d}}_j = 0$, which rearranges equation A.0.1, to a combination of the driving field and all the fields scattered by the other dipoles:

$$\begin{aligned} d_j &= \alpha\mathsf{E}_\ell(r_j) + \alpha\sum_{\ell\neq j}\mathsf{G}_{j\ell}\mathbf{d}_\ell \\ \frac{1}{\alpha}d_j - \sum_{\ell\neq j}\mathsf{G}_{j\ell}d_l &= \mathsf{E}_\ell(r_j), \end{aligned} \tag{A.0.2}$$

where $\alpha = -(\mathcal{D}_0^2/\hbar)/\Big(\Delta + \mathrm{i}(\Gamma_0/2)\Big)$ is the atomic polarisability.

This can be written down in a matrix representation:

$$\left(\frac{1}{\alpha}1 - \sum_{\ell \neq j} \mathsf{G}\right) \vec{\mathbf{d}} \equiv \hat{\mathsf{M}}\vec{\mathbf{d}} = \vec{\mathbf{E}}_{\mathrm{L}}. \tag{A.0.3}$$

The driving field terms $1/\alpha$ and G (which describes all the couplings $\{\mathsf{G}_{j\ell}\}$ between the dipoles) can be combined in a matrix $\hat{M}$ as:

$$\underbrace{\begin{pmatrix} \frac{1}{\alpha} & -\mathsf{G}_{12} & -\mathsf{G}_{13} \\ -\mathsf{G}_{21} & \frac{1}{\alpha} & -\mathsf{G}_{23} \\ -\mathsf{G}_{31} & -\mathsf{G}_{32} & \frac{1}{\alpha} \end{pmatrix}}_{\hat{M}} \underbrace{\begin{pmatrix} d_1 \\ d_2 \\ d_3 \end{pmatrix}}_{\vec{d}} = \underbrace{\begin{pmatrix} \mathsf{E}_\ell(r_1) \\ \mathsf{E}_\ell(r_2) \\ \mathsf{E}_\ell(r_3) \end{pmatrix}}_{\vec{E_L}} \tag{A.0.4}$$

where $\vec{\mathbf{d}}$ and $\vec{\mathbf{E}}_{\mathrm{L}}$ are column vectors of all the dipole and laser field vectors.

Knowing the driving field, each dipole experiences, we can calculate the dipole-dipole interactions based on the position of each atom. This also allows to investigate the dipoles behaviour by looking at the eigenvectors and the eigenvalues of $\hat{M}$.

$$\hat{\mathsf{M}}\vec{m}_q = \left(\frac{1}{\alpha}1 - \sum_{\ell \neq j} \mathsf{G}\right) \vec{m}_q = \left(\frac{1}{\alpha} - g_q\right) \vec{m}_q = \mu_q \vec{m}_q. \tag{A.0.5}$$

where $\mu_q = 1/\alpha - g_q$, in which g_q is the q-th eigenvalue of G.

We can use the eigenvector m_q as a basis and write down $\vec{d}$ and $\vec{E_L}$ as a combination of $\vec{m_q}$ and coefficients a_q and b_q:

$$\begin{aligned} \vec{d} &= \sum_q a_q \vec{m}_q, \\ \vec{E}_L &= \sum_q b_q \vec{m}_q. \end{aligned} \tag{A.0.6}$$

Applying and substituting equation A.0.6 in equation A.0.3 results in:

$$\begin{aligned} \hat{\mathsf{M}} \sum_q a_q \vec{m}_q &= \sum_q a_q (\hat{\mathsf{M}} \vec{m}_q) \\ &= \sum_q a_q \mu_q \vec{m}_q \\ &= \sum_q b_q \vec{m}_q, \end{aligned} \tag{A.0.7}$$

From this we can express the coefficients a_q and b_q using the eigenvalues

μ_q as:

$$\begin{aligned} b_q &= a_q \mu_q, \\ a_q &= \frac{b_q}{\mu_q}. \end{aligned} \tag{A.0.8}$$

For a single atom the dipole moment is proportional to the driving field E_L with a constant of proportionality the polarizability. Using equation (A.0.6) shows that there is an effective polarizability for each q-th eigenmode:

$$\begin{aligned} \vec{d} = \alpha E_L &= \sum_q a_q \vec{m}_q \\ &= \sum_q \frac{b_q}{\mu_q} \vec{m}_q. \end{aligned} \tag{A.0.9}$$

The coefficient b_q as E_0 does not depend on the detunning Δ and therefore is only dependent on the atomic configuration.

Each eigenvector gives an effective polarizability α_q with a complex form. The eigenvalues μ_q are complex and defined as:

$$\begin{aligned} \mu_q = \frac{1}{\alpha} - g_q &= -\frac{\hbar}{\mathcal{D}_0^2}\left(\Delta + \mathrm{i}\frac{\Gamma_0}{2}\right) - g_q = \\ &= -\frac{\hbar}{\mathcal{D}_0^2}\left((\Delta - \Delta_q) + \mathrm{i}\frac{\Gamma_0 + \Gamma_q}{2}\right), \end{aligned} \tag{A.0.10}$$

which has the same form as the inverse atomic polarisability with modified detuning and linewidth. The real part of g_q produces a resonance shift $\Delta_q = (\hbar/\mathcal{D}_0^2) Re(g_q)$ and the imaginary part produces a modification to the decay rate $\Gamma_q = -(\hbar/\mathcal{D}_0^2) Im(g_q)$.

Next, the fiber coupling should be taken into account. The experimental signal is proportional to the coupling of the total electric field into a single mode optical fibre. This coupling can be written as

$$\varepsilon = \int (E(r).l^*(r)) dS \tag{A.0.11}$$

where the total field $E(r) = E_L(r) + \sum_j E_j(r)$ is sum of the driving field and the total scattered field. $l(r)$ is the mode of the single-mode fiber at position r, integrated over an area S perpendicular to the optical axis. This mode is matched to the laser field $l \propto E_L$.

B. Two-channel depahsing model with spin-wave operators

This appendix covers the depahasing model presented in chapter 5 using spin-wave operators.

In the atomic medium the photons are stored as collective Rydberg excitations. The atomic ensemble collective state can be expressed as:

$$|\psi\rangle = \sum_n c_n |\psi_n\rangle \tag{B.0.1}$$

where $|\psi_n\rangle$ is the state containing n collective Rydberg excitations and can be defined using the creation operator $\hat{S}^\dagger$:

$$|\psi\rangle = (\hat{S}^\dagger)^n |G\rangle \tag{B.0.2}$$

where $|G\rangle$ is the collective ground state.

The creation operator $\hat{S}^\dagger$ holds the imprinted signal amplitude E and the combined phase ϕ:

$$\hat{S}^\dagger = \frac{1}{\sqrt{\sum_j E(\vec{r}_j)^2}} \sum_j E(\vec{r}_j) e^{i\phi(\vec{r}_j)} |r_j\rangle\langle g_j| \tag{B.0.3}$$

where $\vec{r_j}$ is the position of atom j.

During the storage time t_{st}, the components of $|\psi_n\rangle$ acquire different phase factors due to interactions between Rydberg atoms. This evolution can be expressed through the operator $\hat{U}(t_{st})$:

$$\hat{U}(t_{st}) = \sum_{j,k>j} e^{-iV_{jk}t_{st}/\hbar} |r_j, r_k\rangle\langle r_j, r_k|. \tag{B.0.4}$$

The collective state acquires an additional phase, leading to a reduction of the probability of photon retrieval in the signal mode from the state

$\hat{U}(t_{st})|\psi_n\rangle$.

For two pairs of photons in the control and signal modes, the overlap between the collective ground state $|G\rangle$ and the state $\hat{U}(t_{st})|\psi_n\rangle$ using the annihilation operator $\hat{S}$, can be expressed as:

$$D^{(2)} = \frac{\langle G|\hat{S}^2\hat{U}(t_{st})\hat{S}^{\dagger 2}|G\rangle}{\langle G|\hat{S}^2\hat{S}^{\dagger 2}|G\rangle}. \tag{B.0.5}$$

In absence of interactions, photons should be retrieved in their original spatial modes. The overlap $D^{(2)}$ can be used to calculate the experimentally measured single-correlation function $g^{(2)}$:

$$g^{(2)} = \frac{2|D^{(2)}|^2|c_2|^2}{(|c_1|^2 + 2|D^{(2)}|^2|c_2|^2)^2}. \tag{B.0.6}$$

In case of two spatially separated mediums, the situation is very similar. The collective state can be expressed as:

$$|\psi^{AB}\rangle = \sum_{n,m\in[0,1]} c_{nm}|\psi^{AB}_{nm}\rangle \tag{B.0.7}$$

where $|\psi^{AB}_{nm}\rangle$ is the state containing n collective Rydberg excitations in channel A and m collective Rydberg excitations in channel B, given by:

$$|\psi^{AB}_{nm}\rangle = |\psi^{A}_{n}\rangle \otimes |\psi^{B}_{m}\rangle \tag{B.0.8}$$

This state can be defined using the creation operators $\hat{S}^\dagger_A$ and $\hat{S}^\dagger_B$:

$$\begin{aligned} |\psi^A_n\rangle &= (\hat{S}^\dagger_A)^n|G^A\rangle, \\ |\psi^B_m\rangle &= (\hat{S}^\dagger_B)^m|G^B\rangle \end{aligned} \tag{B.0.9}$$

where $|G^A\rangle$ and $|G^B\rangle$ are the collective ground state. The creation operators $\hat{S}^\dagger_A$ and $\hat{S}^\dagger_B$ hold the imprinted signal amplitudes E_A and E_B as well as the combined phases ϕ_A and ϕ_B.

During the storage time t_{st}, the components of $|\psi^{AB}_{nm}\rangle$ acquire different phase factors due to interactions between Rydberg atoms stored in the separated channels. This evolution can be expressed through the operator $\hat{U}^{(AB)}(t_{st})$:

$$\hat{U}^{(AB)}(t_{st}) = \sum_{j_A,j_B} e^{-iV_{j_Aj_B}t_{st}/\hbar}|r_{j_A}\rangle\langle r_{j_A}| \otimes |r_{j_B}\rangle\langle r_{j_B}|. \tag{B.0.10}$$

The collective state acquires an additional phase, leading to a reduction in the probability of photon retrieval in the signal mode from the state $\hat{U}^{(AB)}(t_{st})|\psi_{nm}^{(AB)}\rangle$.

For a pair of photons in the control and signal modes in each of the two channels, the overlap between the collective ground state $|\psi_{00}^{(AB)}\rangle$ and the state $\hat{U}(t_{st})|\psi_{nm}^{(AB)}\rangle$ using the annihilation operators $\hat{S}_A$ and $\hat{S}_B$ can be express as:

$$D_{AB}^{(11)} = \frac{\langle\psi_{00}^{(AB)}|\hat{S}_A\hat{S}_B\hat{U}^{(AB)}(t_{st})\hat{S}_A^\dagger\hat{S}_B^\dagger|\psi_{00}^{(AB)}\rangle}{\langle\psi_{00}^{(AB)}|\hat{S}_A\hat{S}_B\hat{S}_A^\dagger\hat{S}_B^\dagger|\psi_{00}^{(AB)}\rangle}. \tag{B.0.11}$$

The overlap $D_{AB}^{(11)}$ allows the calculation of the cross-correlation function $g^{(2)}$ as:

$$g_{AB}^{(2)} = \frac{|D_{AB}^{(11)}|^2|c_{11}|^2}{(|c_{10}|^2 + |D_{AB}^{(11)}|^2|c_{11}|^2)(|c_{01}|^2 + |D_{AB}^{(11)}|^2|c_{11}|^2)}. \tag{B.0.12}$$

C. Photon statistics

The experiments discussed in this thesis are based on detection of single photon events and the second order auto-correlation function $g^{(2)}$ is used as an estimation factor.

In the experiment a Hanbury-Brown Twiss detection setup is used to detect the number of identical photons and their distribution within a pulse of light. It consists of two sensitive avalanche photo diodes (SPADs) which allow the detection of single photon events with relatively small single to noise ratio. These two detectors limits the possible physical photon events in the system to 2 (no more than 2 photons can be detected simultaneously). This defines the second order auto-correlation function $g^{(2)}$ as:

$$\begin{aligned} g^{(2)}(0) &= \frac{\langle n(n-1)\rangle}{\langle n^2\rangle} = \\ &= \frac{0(-1)P(0) + 1(0)P(1) + 2(1)P(2)}{(0P(0) + 1P(1) + 2P(2))^2} = \\ &= \frac{2P(2)}{(P(1) + 2P(2))^2}. \end{aligned} \tag{C.0.1}$$

The possible photon events configurations inside the Hanbury-Brown Twiss interferometer are shown in table C.1. If there is 1 photon it can go to detector A or B. And in case of 2 photon event, both photons can go to A or B, or to A and B.

The photon event counting efficiency of each of the two detectors (SPAD A and SPAD B) is defined as:

$$\begin{aligned} \varepsilon_A &= \frac{n_A}{n_A + n_B}, \\ \varepsilon_B &= \frac{n_B}{n_A + n_B} \end{aligned} \tag{C.0.2}$$

where n_A and n_B are the number of counts on SPAD A and SPAD B respectively.

The probability table C.1 connects the physical events in the experiment

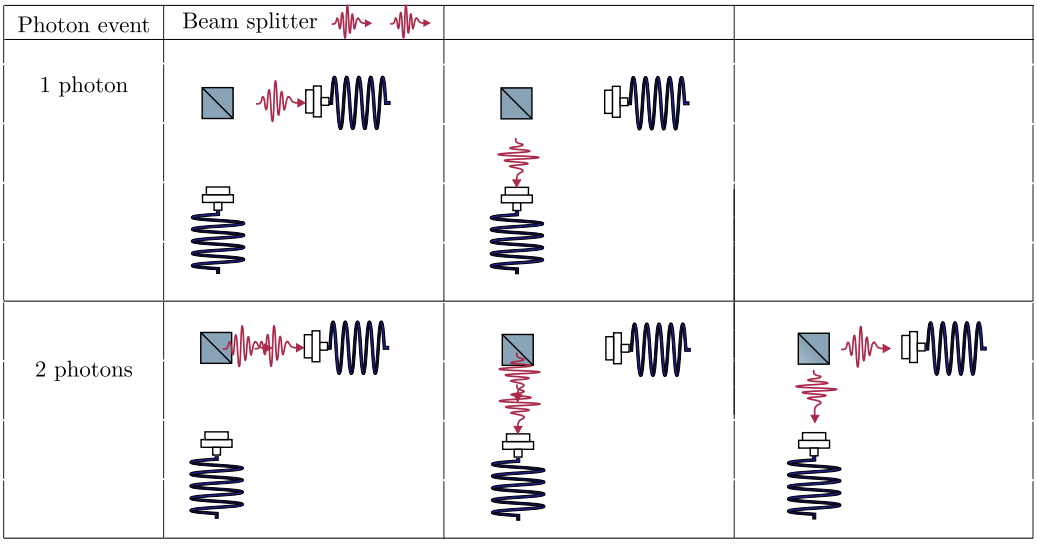

Figure C.1.: Photon events possible configurations inside the Hanbury-Brown Twiss interferometer.

(the number of photons arriving on the detection system, between 0 and 2) with the detected events (clicks on the detectors, between 0 and 2).

From the probability table, we can express the physical events as a function of the measured photons:

$$\begin{aligned} P(2) &= \frac{1}{2\varepsilon_A\varepsilon_B}P(AB), \\ P(1) &= \Big(\varepsilon_B P(A) + \epsilon_A P(B) - (2 - \frac{3}{2}(\varepsilon_A + \varepsilon_B)P(AB)\Big)/2\varepsilon_A\varepsilon_B. \end{aligned} \tag{C.0.3}$$

Substituting equation C.0.3 in equation C.0.1, the second order auto-correlation function $g^{(2)}$ can be defined only by the detected photon events as:

$$g^{(2)}(0) = \frac{\varepsilon_A\varepsilon_B 4P(AB)}{\Big(P(A)\varepsilon_B + P(B)\varepsilon_A + 3P(AB)/2\Big)^2}. \tag{C.0.4}$$

The detection efficiency in the $g^{(2)}$ expression appears only through the relative efficiency of the two detectors.

Each of the two detectors has 38 ns death time and for further deeper analysis it should also be taken into account.

The two channel second order auto-correlation function $g^{(2)}$ is calculated

	SPADs			
Events	$P(0)$	$P(A)$	$P(B)$	$P(AB)$
0	1	0	0	0
	$(1-P(A))$	$P(A)$	0	0
1	$(1-P(B))$	0	$P(B)$	0
	1	0	0	0
	$(1-P(A))^2$	$P(A)(2-P(B))$	0	0
2	$(1-P(B))^2$	0	$P(B)(2-P(A))$	0
	$(1-P(A))(1-P(B))$	$P(A)(1-P(B))$	$P(B)(1-P(A))$	$P(A)P(B)$

Table C.1.: Probability table that connects the possible physical events in the experiment (the number of photons arriving on the detection system) with the detected events (click on a detector).

Finally, I am incredibly lucky to have such an amazing family. My husband Iliya who has always supported me in the choices I have made, and have allowed me to pursue all my dreams. Thanks for always being there whenever I needed you. I must also thank my parents, who have always believed in me and love me unconditionally. My cousin, Cveta, whose frequent calls always cheer me up. Last, but definit

using the same method for two possible physical photon events in each channel and two identical Hanbury-Brown Twiss detection setups. The possible physical photon events $P(i,j)$ (for i,j between 0 and 2) are defined by the detected photon events in the experiment (SPAD A, SPAD B, SPAD C and SPAD D) and substituted in the cross-correlation $g^{(2)}$ formula:

$$g^{(2)}(0) = \frac{\langle n_i n_j \rangle}{\langle n_i \rangle \langle n_j \rangle} = \\ = \frac{P(1,1) + 2(P(1,2) + P(2,1)) + 4P(2,2)}{\Big(P(1,0) + P(1,1) + P(1,2) + 2(P(2,0) + P(2,1) + P(2,2))\Big)} \cdot \\ \frac{1}{\Big(P(0,1) + P(1,1) + P(2,1) + 2(P(0,2) + P(1,2) + P(2,2))\Big)}. \tag{C.0.5}$$

The second order cross-correlation function $g^{(2)}$, defined only by the

detected photon events, is given as:

$$g^{(2)}(0) = \frac{(\varepsilon_B\varepsilon_D P(A,C) + \varepsilon_B\varepsilon_C P(A,D) + \varepsilon_A\varepsilon_D P(B,C) + \varepsilon_A\varepsilon_C P(B,D)}{(\varepsilon_B P(A) + \varepsilon_A P(B) + 3P(AB)/2)(\varepsilon_D P(C) + \varepsilon_C P(D) + 3P(CD)/2)} + \frac{3(\varepsilon_D P(AB,C) + \varepsilon_C P(AB,D) + \varepsilon_B P(A,CD) + \varepsilon_A P(B,CD))/2}{\varepsilon_B P(A) + \varepsilon_A P(B) + 3P(AB)/2)(\varepsilon_D P(C) + \varepsilon_C P(D) + 3P(CD)/2)} + \frac{9P(AB,CD)/4}{\varepsilon_B P(A) + \varepsilon_A P(B) + 3P(AB)/2)(\varepsilon_D P(C) + \varepsilon_C P(D) + 3P(CD)/2)} \tag{C.0.6}$$

where ε_A, ε_B, ε_C and ε_D are the corresponding photon event counting efficiencies of each of the two sets of detectors ((SPAD A and SPAD B) and (SPAD C and SPAD D)).

Finally, I am incredibly lucky to have such an amazing family. My husband Iliya who has always supported me in the choices I have made, and have allowed me to pursue all my dreams. Thanks for always being there whenever I needed you. I must also thank my parents, who have always believed in me and love me unconditionally. My cousin, Cveta, whose frequent calls always cheer me up. Last, but definit

Bibliography

[1] A. Ekert, N. Gisin, B. Huttner, H. Inamori, and H. Weinfurter, "The Physics of Quantum Information", Springer (2000).

[2] J. L. O'Brien, "Optical Quantum Computing", Science **318**, 1567 (2007).

[3] R. Alléaume, F. Treussart, G. Messin, Y. Dumeige, J. F. Roch, A. Beveratos, R. Brouri-Tualle, J. P. Poizat, and P. Grangier, "Experimental open-air quantum key distribution with a single-photon source", New Jour. of Phys. **6** (2004).

[4] T. Gaebel, I. Popa, A. Gruber, M. Domhan, F. Jelezko, and J. Wrachtrup, "Stable single-photon source in the near infrared", New Jour. of Phys. **6** (2004).

[5] E. Wu, J. R. Rabeau, G. Roger, F. Treussart, H. Zeng, P. Grangier, S. Prawer, and J. F. Roch, "Room temperature triggered single-photon source in the near infrared", New Jour. of Phys. **9** (2007).

[6] S. Kako, C. Santori, K. Hoshino, S. Gotzinger, Y. Yamamoto, and Y. Arakawa, "A gallium nitride single-photon source operating at 200 K", Nat. Mater. **5**, 887 (2006).

[7] S. Strauf, N. G. Stoltz, M. T. Rakher, L. A. Coldren, P. M. Petroff, and D. Bouwmeester, "High-frequency single-photon source with polarization control", Nat. Photon. **1**, 704 (2007).

[8] N. Somaschi, V. Giesz, L. D. Santis, J. C. Loredo, M. P. Almeida, G. Hornecker, S. L. Portalupi, T. Grange, C. Antón, J. Demory, C. Gómez, I. Sagnes, N. D. Lanzillotti-Kimura, A. Lemaitre, A. Auffeves, A. G. White, L. Lanco, and P. Senellart, "Near-optimal single-photon sources in the solid state", Nat. Photon. **10**, 340 (2016).

[9] M. Hennrich, T. Legero, A. Kuhn, and G. Rempe, "Photon statistics of a non-stationary periodically driven single-photon source", New Jour. of Phys. **6** (2004).

[10] C. Maurer, C. Becher, C. Russo, J. Eschner, and R. Blatt, "A single-photon source based on a single Ca+ ion", New Jour. of Phys. **6** (2004).

[11] M. Steiner, A. Hartschuh, R. Korlacki, and A. J. Meixner, "Highly efficient, tunable single photon source based on single molecules", Appl. Phys. Lett. **90**, 183122 (2007).

[12] S. Chen, Y. Chen, T. Strassel, Z. Yuan, B. Zhao, J. Schmiedmayer, and J. Pan, "Deterministic and storable single-photon source based on a quantum memory", Phys. Rev. Lett. **97**, 173004 (2006).

[13] A. Soujaeff, T. Nishioka, T. Hasegawa, S. Takeuchi, T. Tsurumaru, K. Sasaki, and M. Matsui, "Quantum key distribution at 1550 nm using a pulse heralded single photon source", Opt. Expr. **15**, 726 (2007).

[14] E. A. Goldschmidt, M. D. Eisaman, J. Fan, S. V. Polyakov, and A. Migdall, "Spectrally bright and broad fiber-based heralded single-photon source", Phys. Rev. A **78**, 013844 (2008).

[15] D. J. Whiting, N. Šibalić, J. Keaveney, C. S. Adams, and I. G. Hughes, "Single-photon interference due to motion in an atomic collective excitation", Phys. Rev. Lett. **118**, 253601 (2017).

[16] K. M. Birnbaum, A. Boca, R. Miller, A. D. Boozer, T. E. Northup, and H. J. Kimble, "Photon blockade in an optical cavity with one trapped atom", Nature **436**, 87 (2005).

[17] A. Reiserer and G. Rempe, "Cavity-based quantum networks with single atoms and optical photons", Rev. Mod. Phys. **87**, 1379 (2015).

[18] B. Hacker, S. Welte, G. Rempe, and S. Ritter, "A photon–photon quantum gate based on a single atom in an optical resonator", Nature **536**, 193 (2016).

[19] C. W. Chou, S. V. Polyakov, A. Kuzmich, and H. J. Kimble, "Single-photon generation from stored excitation in an atomic ensemble", Phys. Rev. Lett. **92**, 213601 (2004).

[20] D. N. Matsukevich, T. Chaneliere, S. D. Jenkins, S. Y. Lan, T. A. B. Kennedy, and A. Kuzmich, "Deterministic single photons via conditional quantum evolution", Phys. Rev. Lett. **97**, 013601 (2006).

[21] C. H. van der Wal, M. D. Eisaman, A. Andre, R. L. Walsworth, D. F. Philips, A. S. Zibrov, and M. D. Lukin, "Atomic memory for correlated photon states", Science **301**, 196 (2003).

[22] A. Kuzmich, W. P. Bowen, A. D. Boozer, A. Boca, C. W. Chou, L. M. Duan, and H. J. Kimble, "Generation of nonclassical photon pairs for scalable quantum communication with atomic ensembles", Nature **423**, 731 (2003).

[23] R. W. Boyd, "Nonlinear Optics", Academic Press (2008).

[24] H. Mabuchi and A. C. Doherty, "Cavity quantum electrodynamics: coherence in context", Science **298**, 1372 (2002).

[25] T. Peyronel, O. Firstenberg, Q.-Y. Liang, S. Hofferberth, A. V. Gorshkov, T. Pohl, M. D. Lukin, and V. Vuletić, "Quantum nonlinear optics with single photons enabled by strongly interacting atoms", Nature **488**, 57 (2012).

[26] C. Tresp, C. Zimmer, I. Mirgorodskiy, H. Gorniaczyk, A. Paris-Mandoki, and S. Hofferberth, "Single photon absorber based on strongly interacting Rydberg atoms", Phys. Rev. Lett. **117**, 223001 (2016).

[27] J. D. Pritchard, D. Maxwell, A. Gauguet, K. J. Weatherill, M. P. A. Jones, and C. S. Adams, "Cooperative atom-light interaction in a blockaded Rydberg ensemble", Phys. Rev. Lett. **105**, 193603 (2010).

[28] O. Firstenberg, C. S. Adams, and S. Hofferberth, "Nonlinear quantum optics mediated by Rydberg interactions", J. Phys. B: At. Mol. Opt. Phys. **49**, 152003 (2016).

[29] C. Murray and T. Pohl, "Quantum and nonlinear optics in strongly interacting atomic ensembles", Advances in Atomic, Molecular, and Optical Physics **65**, edited by E. Arimondo, C. C. Lin, and S. F. Yelin, 321 (2016).

[30] C. S. Hofmann, G. Günter, H. Schempp, M. R. de Saint-Vincent, M. Gärttner, J. Evers, S. Whitlock, and M. Weidemüller, "Sub-Poissonian statistics of Rydberg-interacting Dark state polaritons", Phys. Rev. Lett. **110**, 203601 (2013).

[31] H. Busche, P. Huillery, S. W. Ball, T. V. Ilieva, M. P. A. Jones, and C. S. Adams, "Contactless non-linear optics mediated by long-range Rydberg interactions", Nat. Phys. **13**, 655 (2017).

[32] D. A. Steck, "Rubidium 87 D Line Data", (2009).

[33] J. Gea-Banacloche, Y. Li, S. Jin, and M. Xiao, "Electromagnetically induced transparency in ladder-type inhomogeneously broadened media: Theory and experiment", Phys. Rev. A **51**, 576 (1995).

[34] G. Lindblad, "On the generators of quantum dynamical semigroups", Commun. Math. Phys. **48**, 119 (1976).

[35] J. D. Pritchard, "Cooperative optical non-linearity in a blockaded Rydberg ensemble", Doctoral thesis, Durham University (2011).

[36] S. H. Autler and C. H. Townes, "Stark effect in rapidly varying fields", Phys. Rev. **100**, 703 (1955).

[37] M. Fleischhauer, A. Imamoglu, and J. P. Marangos, "Electromagnetically induced transparency: optics in coherent media", Rev. Mod. Phys. **77**, 633 (2005).

[38] M. Fleischhauer and M. D. Lukin, "Dark-state polaritons in Electromagnetically induced transparency", Phys. Rev. Lett. **84**, 5094 (2000).

[39] C. Liu, Z. Dutton, C. H. Behroozi, and L. V. Hau, "Observation of coherent optical information storage in an atomic medium using halted light pulses", Nature **409**, 490 (2001).

[40] D. F. Phillips, A. Fleischhauer, A. Mair, R. L. Walsworth, and M. D. Lukin, "Storage of Light in Atomic Vapor", Phys. Rev. Lett. **86**, 783 (2001).

[41] J. R. Rydberg, "XXXIV. On the structure of the line-spectra of the chemical elements", Philos. Mag. **29**, 331–337 (1890).

[42] W. Li, I. Mourachko, M. W. Noel, and T. F. Gallagher, "Millimeter-wave spectroscopy of cold Rb Rydberg atoms in a magneto-optical trap: quantum defects of the *ns* , *np* , and *nd* series", Phys. Rev. A **67**, 052502 (2003).

[43] J. Han, Y. Jamil, D. V. L. Norum, P. J. Tanner, and T. F. Gallagher, "Rb nf quantum defects from millimeter-wave spectroscopy of cold ^{85}Rb Rydberg atoms", Phys. Rev. A **74**, 054502 (2006).

[44] K. Afrousheh, P. Bohlouli-Zanjani, J. A. Petrus, and J. D. D. Martin, "Determination of the ^{85}Rb ng-series quantum defect by electric-field-induced resonant energy transfer between cold Rydberg atoms", Phys. Rev. A **74**, 062712 (2006).

[45] D. Paredes-Barato and C. S. Adams, "All-optical Quantum information processing using Rydberg gates", Phys. Rev. Lett. **112**, 040501 (2014).

[46] L. Isenhower, E. Urban, X. L. Zhang, A. T. Gill, T. Henage, T. A. Johnson, T. G. Walker, and M. Saffman, "Demonstration of a neutral atom controlled-NOT Quantum gate", Phys. Rev. Lett. **104**, 010503 (2010).

[47] T. Wilk, A. Gaëtan, C. Evellin, J. Wolters, Y. Miroshnychenko, P. Grangier, and A. Browaeys, "Entanglement of two individual neutral atoms using Rydberg blockade", Phys. Rev. Lett. **104**, 010502 (2010).

[48] F. Gallagher, "Rydberg atom", Cambridge University Press (1994).

[49] K. A. Safinya, J. F. Delpech, F. Gounand, W. Sandner, and T. F. Gallagher, "Resonant Rydberg atom - Rydberg atom collisions", Phys. Rev. Lett. **47**, 405 (1981).

[50] W. R. Anderson, J. R. Veale, and T. F. Gallagher, "Resonant dipole - dipole energy transfer in a nearly frozen Rydberg gas", Phys. Rev. Lett. **80**, 249 (1998).

[51] D. Barredo, H. Labuhn, S. Ravets, T. Lahaye, A. Browaeys, and C. S. Adams, "Coherent excitation transfer in a spin chain of three Rydberg atoms", Phys. Rev. Lett. **114**, 113002 (2015).

[52] H. Gorniaczyk, C. Tresp, J. Schmidt, H. Fedder, and S. Hofferberth, "Single-photon transistor mediated by interstate Rydberg interactions", Phys. Rev. Lett. **113**, 053601 (2014).

[53] D. Tiarks, S. Baur, K. Schneider, S. Dürr, and G. Rempe, "Single-photon transistor Using a Förster resonance", Phys. Rev. Lett. **113**, 053602 (2014).

[54] M. D. Lukin, M. Fleischhauer, R. Côté, L. M. Duan, D. Jaksch, J. I. Cirac, and P. Zoller, "Dipole blockade and quantum information processing in mesoscopic atomic ensembles", Phys. Rev. Lett. **87**, 037901 (2001).

[55] D. Jaksch, J. I. Cirac, P. Zoller, S. L. Rolston, R. Côté, and M. D. Lukin, "Fast quantum gates for neutral atoms", Phys. Rev. Lett. **85**, 2208 (2000).

[56] H. Busche, "Contactless quantum non-linear optics with cold Rydberg atoms", Doctoral thesis, Durham University (2017).

[57] S. W. Ball, "A coherent microwave interface for manipulation of single optical photons", Doctoral thesis, Durham University (2017).

[58] K. Dieckmann, R. J. C. Spreeuw, M. Weidemüller, and J. T. M. Walraven, "Two-dimensional magneto-optical trap as a source of slow atoms", Phys. Rev. A **58**, 3891 (1998).

[59] D. Comparat and P. Pillet, "Dipole blockade in a cold Rydberg atomic sample", J. Opt. Soc. Am. B **27**, A208 (2010).

[60] E. L. Raab, M. Prentiss, A. Cable, S. Chu, and D. E. Pritchard, "Trapping of neutral Sodium atoms with radiation pressure", Phys. Rev. Lett. **59**, 2631 (1987).

[61] J. H. Shirley, "Modulation transfer processes in optical heterodyne saturation spectroscopy", Opt. Lett. **7**, 537 (1982).

[62] D. J. McCarron, S. A. King, and S. L. Cornish, "Modulation transfer spectroscopy in atomic rubidium", Meas. Sci. Technol. **19**, 105601 (2008).

[63] S. C. Bell, D. M. Heywood, J. D. White, J. D. Close, and R. E. Scholten, "Laser frequency offset locking using electromagnetically induced transparency", Appl. Phys. Lett. **90**, 171120 (2007).

[64] R. P. Abel, A. K. Mohapatra, M. G. Bason, J. D. Pritchard, K. J. Weatherill, U. Raitzsch, and C. S. Adams, "Laser frequency stabilization to excited state transitions using electromagnetically induced transparency in a cascade system", Appl. Phys. Lett. **94**, 071107 (2009).

[65] G. C. Bjorklund, "Frequency-modulation spectroscopy: a new method for measuring weak absorptions and dispersions", Opt. Lett. **5**, 15 (1980).

[66] R. W. P. Drever, J. L. Hall, F. V. Kowalski, J. Hough, G. M. Ford, A. J. Munley, and H. Ward, "Laser phase and frequency stabilization using an optical resonators", Appl. Phys. B **31**, 97 (1983).

[67] D. T. Maxwell, "Light storage and control of photon-photon interactions in a cold Rydberg gas", Doctoral thesis, Durham University (2017).

[68] W. Ketterle, K. B. Davis, M. A. Joffe, A. Martin, and D. E. Pritchard, "High densities of cold atoms in a dark spontaneous-force optical trap", Phys. Rev. Lett. **70**, 2253 (1993).

[69] R. Bourgain, J. Pellegrino, A. Fuhrmanek, Y. R. P. Sortais, and A. Browaeys, "Evaporative cooling of a small number of atoms in

a single-beam microscopic dipole trap", Phys. Rev. A **88**, 023428 (2013).

[70] C. S. Adams, H. J. Lee, N. Davidson, M. Kasevich, and S. Chu, "Evaporative cooling in a crossed dipole trap", Phys. Rev. Lett. **74**, 3577 (1995).

[71] G. Günter, M. Robert-de-Saint-Vincent, H. Schempp, C. S. Hofmann, S. Whitlock, and M. Weidemüller, "Interaction Enhanced Imaging of Individual Rydberg Atoms in Dense Gases", Phys. Rev. Lett. **108**, 013002 (2012).

[72] R. Hanbury-Brown and R. Q. Twiss, "Correlation between Photons in two Coherent Beams of Light", Nature **177**, 27 (1956).

[73] T. P. Wiles, "Dynamics of bright solitary matter-waves", Doctoral thesis, Durham University (2013).

[74] R. Rohlsberger, K. Schlage, B. Sahoo, S. Couet, and R. Rüffer, "Collective Lamb shift in single-photon superradiance", Science **328**, 1248 (2010).

[75] Y. Yoshikawa, Y. Torii, and T. Kuga, "Superradiant light scattering from thermal atomic vapors", Phys. Rev. Lett. **94**, 083602 (2005).

[76] A. Goban, C. L. Hung, J. D. Hood, S. P. Yu, J. A. Muniz, O. Painter, and H. J. Kimble, "Superradiance for atoms trapped along a photonic crystal waveguide", Phys. Rev. Lett. **115**, 063601 (2015).

[77] W. Guerin, M. O. Araújo, and R. Kaiser, "Subradiance in a large cloud of cold atoms", Phys. Rev. Lett. **116**, 083601 (2016).

[78] J. Keaveney, A. Sargsyan, U. Krohn, I. G. Hughes, D. Sarkisyan, and C. S. Adams, "Cooperative Lamb Shift in an atomic vapor layer of nanometer thickness", Phys. Rev. Lett. **108**, 173601 (2012).

[79] R. G. DeVoe and R. G. Brewer, "Observation of superradiant and subradiant spontaneous emission of two trapped ions", Phys. Rev. Lett. **76**, 2049 (1996).

[80] M. Scheibner, T. Schmidt, L. Worschech, A. Forchel, G. Bacher, T. Passow, and D. Hommel, "Superradiance of quantum dots", Nat. Phys. **3**, 106 (2007).

[81] Z. Meir, O. Schwartz, E. Shahmoon, D. Oron, and R. Ozeri, "Cooperative Lamb shift in a mesoscopic atomic array", Phys. Rev. Lett. **113**, 193002 (2014).

[82] R. H. Dicke, "Coherence in spontaneous radiation processes", Phys. Rev. **93**, 99 (1954).

[83] N. Skribanowitz, I. P. Herman, J. C. MacGillivray, and M. S. Feld, "Observation of Dicke superradiance in optically pumped HF gas", Phys. Rev. Lett. **30**, 309 (1973).

[84] M. Gross, C. Fabre, P. Pillet, and S. Haroche, "Observation of near-infrared Dicke superradiance on cascading transitions in atomic Sodium", Phys. Rev. Lett. **36**, 1035 (1976).

[85] J. M. Raimond, P. Goy, M. Gross, C. Fabre, and S. Haroche, "Collective absorption of blackbody radiation by Rydberg atoms in a cavity: an experiment on Bose statistics and Brownian motion", Phys. Rev. Lett. **49**, 117 (1982).

[86] S. J. Roof, K. J. Kemp, M. D. Havey, and I. M. Sokolov, "Observation of single-photon superradiance and the cooperative Lamb shift in an extended sample of cold atoms", Phys. Rev. Lett. **117**, 073003 (2016).

[87] M. O. Araújo, I. Krešić, R. Kaiser, and W. Guerin, "Superradiance in a large and dilute cloud of cold atoms in the linear-optics regime", Phys. Rev. Lett. **117**, 073002 (2016).

[88] M. O. Scully, "Collective Lamb shift in single photon Dicke superradiance", Phys. Rev. Lett. **102**, 143601 (2009).

[89] N. E. Rehler and J. H. Eberly, "Superradiance", Phys. Rev. A **3**, 1735 (1971).

[90] S. Haroche, "High-resolution laser spectroscopy", Springer **13**, 253 (1976).

[91] R. J. Bettles, T. Ilieva, H. Busche, P. Huillery, S. W. Ball, N. L. R. Spong, and C. S. Adams, "Collective mode interferences in light matter interactions", arXiv:1808.08415 (2019).

[92] T. Bienaimé, N. Piovella, and R. Kaiser, "Controlled Dicke subradiance from a large cloud of two-level systems", Phys. Rev. Lett. **108**, 123602 (2012).

[93] J. L. O'Brien, "Optical Quantum Computing", Science **318**, 1567–1570 (2007).

[94] R. Loudon, "The Quantum Theory of Light", Oxford University, New York (1983).

[95] E. Urban, T. A. Johnson, T. Henage, L. Isenhower, D. D. Yavuz, T. G. Walker, and M. Saffman, "Observation of Rydberg blockade between two atoms", Nat. Phys. **5**, 110–114 (2009).

[96] A. Gaëtan, Y. Miroshnychenko, T. Wilk, A. Chotia, M. Viteau, D. Comparat, P. Pillet, A. Browaeys, and P. Grangier, "Observation of collective excitation of two individual atoms in the Rydberg blockade regime", Nat. Phys. **5**, 115 (2009).

[97] A. V. Gorshkov, A. André, M. D. Lukin, and A. S. Sørensen, "Photon storage in Λ-type optically dense atomic media. I. Cavity model", Phys. Rev. A **76**, 033804 (2007).

[98] F. Bariani, Y. O. Dudin, T. A. B. Kennedy, and A. Kuzmich, "Dephasing of multiparticle Rydberg excitations for fast entanglement generation", Phys. Rev. Lett. **108**, 030501 (2012).

[99] S. Baur, D. Tiarks, G. Rempe, and S. Dürr, "Single-photon switch based on Rydberg blockade", Phys. Rev. Lett. **112**, 073901 (2014).

[100] D. Tiarks, S. Schmidt, G. Rempe, and S. Dürr, "Optical π phase shift created with a single-photon pulse", Sci. Adv. **2**, 1600036 (2016).

[101] R. Grimm, M. Weidemüller, and Y. B. Ovchinnikov, "Optical dipole traps for neutral atoms", Academic Press, 95 (1999).

[102] C. K. Hong, Z. Y. Ou, and L. Mandel, "Measurement of subpicosecond time intervals between two photons by interference", Phys. Rev. Lett. **59**, 2044 (1987).

[103] P. P. Rohde, T. C. Ralph, and M. A. Nielsen, "Optimal photons for quantum-information processing", Phys. Rev. Lett. A **72**, 052332 (2005).

[104] P. B. R. Nisbet-Jones, J. Dilley, D. Ljunggren, and A. Kuhn, "Highly efficient source for indistinguishable single photons of controlled shape", New J. Phys. **13**, 103036 (2011).

[105] M. Himsworth, P. Nisbet, J. Dilley, G. Langfahl-Klabes, and A. Kuhn, "EIT-based quantum memory for single photons from cavity-QED", Appl. Phys. B **103**, 579 (2011).

[106] P. Nisbet-Jones, "Shaping single photons", Doctoral thesis, Oxford University (2012).

[107] R. J. Bettles, "Cooperative Interactions in Lattices of Atomic Dipoles", Doctoral thesis, Durham University (2016).